

Neutron Activation Analysis of Inhomogeneous Large Samples

An Explorative Study

Cover illustration: Dorine and Nora analysing wedge of cake shaped sand sample using RED NAILS

The research described in this thesis was conducted within the Department of Radiochemistry of the Interfaculty Reactor Institute, Delft University of Technology, Mekelweg 15, 2629 JB Delft, The Netherlands

Het in dit proefschrift beschreven onderzoek is uitgevoerd binnen de afdeling Radiochemie van het Interfacultair Reactor Instituut, Technische Universiteit Delft, Mekelweg 15, 2629 JB Delft.

Neutron Activation Analysis of Inhomogeneous Large Samples

An Explorative Study

Proefschrift

ter verkrijging van de graad van doctor
aan de Technische Universiteit Delft,
op gezag van de Rector Magnificus prof. dr. ir. J.T. Fokkema,
voorzitter van het College voor Promoties,
in het openbaar te verdedigen

op maandag 11 oktober 2004 om 13:00 uur

door

Hendrik Willem BAAS

doctorandus in de natuurkunde
geboren te Staphorst

Dit proefschrift is goedgekeurd door de promotoren:

Prof. dr. ir. J.J.M. de Goeij

Prof. dr. ir. A.H.M. Verkooijen

Samenstelling Promotiecommissie

Rector Magnificus,	voorzitter
Prof. dr. ir. J.J.M. de Goeij,	Technische Universiteit Delft, promotor
Prof. dr. ir. A.H.M. Verkooijen,	Technische Universiteit Delft, promotor
Dr. A.V. Bronnikov,	Nucletron, Veenendaal
Prof. dr. ir. H. van Dam,	Technische Universiteit Delft
Prof. dr. ir. C.W.E. van Eijk,	Technische Universiteit Delft
Prof. dr. W. Görner	German Academy of Sciences, Berlin, Germany
Prof. dr. ir. L.J. van Vliet,	Technische Universiteit Delft

Dr. M. Blaauw heeft als begeleider in belangrijke mate aan de totstandkoming van het proefschrift bijgedragen.

Published and distributed by: DUP Science

DUP Science is an imprint of
Delft University Press
P.O. Box 98
2600 MG Delft
The Netherlands
Telephone: +31 15 27 85 678
Telefax: +31 15 27 85 706
E-mail: DUP@Library.TUdelft.NL

ISBN 90-407-2528-4

Keywords: neutron activation analysis, gamma-ray spectrometry, large samples, inhomogeneity

Copyright © 2004 by Hendrik Willem BAAS.

All rights reserved. No part of the material protected by this copyright notice may be reproduced or utilized in any form or by any means, electronic or mechanical, including photocopying, recording or by any information storage and retrieval system, without written permission from the publisher:
Delft University Press.

Printed in the Netherlands

*Aanschouw ik uw hemel, het werk van uw vingers,
de maan en de sterren, die Gij bereid hebt:
Wat is de mens, dat Gij zijner gedenkt,
en het mensenkind, dat Gij naar hem omziet?
Toch hebt Gij hem bijna goddelijk gemaakt,
En hem met heerlijkheid en luister gekroond*

Psalm 8: 4-6, Vertaling NBG 1951

Voor Anneclair, Dorine en Nora

Table of contents

<u>LIST OF SYMBOLS</u>	XI
<u>LIST OF ABBREVIATIONS</u>	XIV
<u>CHAPTER 1 RECONSTRUCTION OF ELEMENT DISTRIBUTIONS IN NEUTRON ACTIVATED INHOMOGENEOUS LARGE SAMPLES, INTRODUCTION</u>	<u>1</u>
1.1 Neutron Activation Analysis	1
1.2 LS-NAA	5
1.3 Scope of the dissertation work	8
1.4 Contents of the thesis: Neutron Activation Analysis of Inhomogeneous Large Samples	9
1.5 References	9
<u>CHAPTER 2 SAMPLING, HOMOGENEITY AND REPRESENTATIVITY</u>	<u>11</u>
2.1 Introduction	11
2.2 Definitions	11
2.3 Sampling in practice	14
2.4 Discussion	17
2.5 Conclusions	18
2.6 References	18
<u>CHAPTER 3 RECONSTRUCTION OF ELEMENT DISTRIBUTIONS IN NEUTRON ACTIVATED INHOMOGENEOUS LARGE SAMPLES</u>	<u>21</u>
3.1 Introduction	21
3.2 Theory	22
3.3 Experimental facilities	24
3.4 Experimental calibration procedures	30
3.5 Experimental sample analysis procedures	31
3.6 Data analysis and processing	32
3.7 References	36
<u>CHAPTER 4 3D-MODELLING OF THE GE DETECTOR FULL-ENERGY PEAK EFFICIENCY FOR MEASUREMENTS OF THE SPATIAL RADIOACTIVITY DISTRIBUTIONS</u>	<u>37</u>
4.1 Introduction	37

4.2 Theory	39
4.3 Experimental set-up and methods	45
4.4 Results	48
4.5 Discussion and conclusions	59
4.6 References	62
<u>CHAPTER 5 OPTIMISATION OF THE LS-INAA MEASUREMENT FACILITY FOR SCANNED MEASUREMENTS</u>	63
5.1 Introduction	63
5.2 Theory	66
5.3 Methods	70
5.4 Results	72
5.5 Discussion and conclusions	79
5.6 References	83
<u>CHAPTER 6 DETECTION OF INHOMOGENEITIES VIA COLLIMATED SCANNING</u>	85
6.1 Introduction	85
6.2 Theory	86
6.3 Methods	88
6.4 Experimental	90
6.5 Results	91
6.6 Discussion and conclusions	95
6.7 References	98
<u>CHAPTER 7 GAMMA-RAY ATTENUATION ASSESSMENT</u>	99
7.1 Introduction	99
7.2 Theory	99
7.3 Methods and experimental	101
7.4 Results and discussion	103
7.5 Conclusions	103
7.6 References	105
<u>CHAPTER 8 RECONSTRUCTION ALGORITHMS FOR ANALYSIS OF ELEMENT DISTRIBUTIONS IN NEUTRON-ACTIVATED INHOMOGENEOUS LARGE SAMPLES</u>	107
8.1 Introduction	107
8.2 Theory and methods	108
8.3 Modelling studies and phantom experiment	115

Table of contents

8.4 Results	116
8.5 Discussion and conclusions	117
8.6 References	121
CHAPTER 9 REDNAILS: APPLICATION WITH PRIOR KNOWLEDGE TO SAMPLES OF PRACTICAL INTEREST	123
9.1 Introduction	123
9.2 Theory	124
9.3 Methods and results	126
9.4 Discussion and conclusions	137
9.5 References	137
CHAPTER 10 GENERAL DISCUSSION	139
10.1 Introduction	139
10.2 Detection of inhomogeneities	139
10.3 Reconstruction of element distributions	140
10.4 Definition of the design problem	140
10.5 Open issues	141
10.6 References	146
SUMMARY REDNAILS	149
SAMENVATTING REDNAILS	153
DANKWOORD	157
CURRICULUM VITAE	159
LIST OF PUBLICATIONS	160

List of symbols

Symbols for Neutron Activation Analysis

A	Activity	[Bq]
E_γ	Energy of photon	[J]
$A(E_\gamma)$	Area of the detected photo-peak due to gamma-rays with energy E_γ	
A_{ijl}	Area of the detected photo-peak at gamma energy l due to gamma-rays originating from voxel i , in measurement j	
D	neutron diffusion coefficient	[cm]
$I(E_\gamma)$	Photon beam intensity: rate of photons with energy E_γ in a beam	[s ⁻¹]
K : K_{ijnl}	Matrix of expected peak areas for voxel i , measurement j , element n and peak energy l , assuming that voxel i consists of 1 g of element n exclusively.	[g ⁻¹]
L	neutron diffusion length	[cm]
M	atomic mass	[g mol ⁻¹]
N_{Av}	Avogadro's number	[6.022x10 ²³ mol ⁻¹]
\vec{r}	Source position, subscripts: O: position of calibration source. Model: modelled efficiency. Meas: measured efficiency.	
r_{ij}	Source position, voxel i in measurement j	
$t_{\text{subscript}}$	time for process indicated by subscript	[s]
U	Diagonal matrix containing the uncertainties in the A_{jl}	
w	amount of mass of the specific element	[g]
$\gamma(E_\gamma)$	probability of an unstable nucleus emitting a gamma ray of energy E_γ in the decay process.	
θ	isotopic abundance	

λ	Probability of disintegration per unit time	[s ⁻¹]
μ	Attenuation coefficient	[m ⁻¹]
	For intermediate materials, μ is the total attenuation coefficient and subscripts indicate the number of the intermediate material.	
	For the detector, the partial attenuation coefficients corresponding to the photo-electric effect, the Compton effect and pair creation are denoted with the subscripts ph , c and p respectively. The subscript tot is reserved for the total attenuation coefficient and d for the full-energy absorption coefficient.	
$\sigma(E_n)$	Neutron energy dependent neutron absorption cross section	[m ²]
σ_{th}	neutron activation cross section for thermalised neutrons	[m ²]
$\Phi(E_n)$	neutron flux of neutrons with energy E_n	[m ⁻² s ⁻¹ J ⁻¹]
Φ_{th}	neutron flux of thermalised neutrons	[m ⁻² s ⁻¹]

Sampling

G_{batch}	Inhomogeneity of the batch	
M_{sample}	Sample mass	[g]
N_{batch}	number of samples in the batch	
q	Probability that a grain is selected in the sample	
R	Representativity of a sample	
$V(a_{sample})$	Variance of the sample concentration	

Detection efficiency

A_{det}	Detector crystal surface area	[m ²]
$C_{photo}, C_{Compton}, C_{pair},$	Correction factor for the fact that not all photons are detected in the full-energy peak of the detector after a photo effect, Compton interaction or pair creation respectively.	
c	Collimator thickness	[m]
D	Detector diameter	[m]
d	Collimator opening	[m]
$L_{crystal}$	Length of the detector crystal	[m]

List of Symbols

N_{det}	Number equally sized sub-areas on the crystal front end.
$P, \Delta x$	Path of the gamma ray through the detector crystal.
$P_{\text{subscript}}$	Probability for a series of interactions of the photon with the detector crystal described by <i>subscript</i> : <i>Bs+esc</i> : backscattering and escape of the backscattered photon. <i>Fw+det</i> : forward scattering and absorption of the forward scattered photon in the detector crystal.
r	Radius of position of incidence of the gamma with the detector.
R	Detector radius [m]
$(U_{\text{in}}, V_{\text{in}}, W_{\text{in}})$	(or φ, ϑ) Angles of incidence of the gamma ray with the detector.
W_j	Inner product of perpendicular vector of sub area j with the vector that connects the sub area with the point source.
$(X_{\text{in}}, Y_{\text{in}}, Z_{\text{in}})$	position of incidence of the gamma with the detector.
$\varepsilon(E_\gamma)$	Gamma ray detection efficiency, the probability of detecting a photon of energy E_γ in the full-energy peak at very low count rates. Subscripts <i>tot</i> , <i>sample</i> , <i>coll</i> and <i>det</i> indicate the total, sample, collimator and internal detector detection efficiency respectively.

Statistical symbols

C_k	number of counts in channel k
$P(a b)$	Probability of a occurring given condition b
Z_{ik}	z-score of channel k in measurement i
σ	standard deviation
χ_r^2	reduced chi-square value
F^2	Statistical parameter, related to χ_r^2 , used as quality rating of a fitted function in Chapter 4

List of abbreviations

AAS	Atomic Absorption Spectrometry
BGO	Bismuth Germanate, $\text{Bi}_4\text{Ge}_3\text{O}_{12}$
BISNIS	Big Sample Neutron Irradiation System
CAI	Coded Aperture Imaging
CGNN	Conjugate Gradient method with Non-Negative constraint
CM	Centre of mass, position of the sample centre
EGS4	Electron and Gamma Shower 4, Monte Carlo simulation software
FWHM	Full Width at Half Maximum
Ge(Li)	Germanium – Lithium doped
HPGe	High Purity Germanium
IC	Ion Chromatography
ICP-AES	Inductively Coupled Plasma Atomic Emission Spectrometry
ICP-MS	Inductively Coupled Plasma Mass Spectrometry
I-div	I-divergence
(I)NAA	(Instrumental) Neutron Activation Analysis
IRI	Interfaculty Reactor Institute
LS-(I)NAA	Large Sample (Instrumental) Neutron Activation Analysis
MC	Monte Carlo
MLEM	Maximum Likelihood method with Expectation Maximisation
MSE	Mean Square Error
NIGET	Neutron Induced Gamma-ray Emission Tomography
PAA	Photon Activation Analysis
PIXE	Proton Induced X-ray Emission
REDNAILS	Reconstruction of Element Distribution in Neutron Activated Inhomogeneous Large Samples
RNAA	Radiochemical Neutron Activation Analysis
SSMS	Spark Source Mass Spectrometry
XRF	X-ray Fluorescence

Chapter 1

Reconstruction of Element Distributions in Neutron Activated Inhomogeneous Large Samples, Introduction

The aim of the work described in this thesis is the development of a reconstruction method for the determination of spatial element distributions using Large-Sample Neutron Activation Analysis.

For a proper introduction to this field of research, first the principles of Neutron Activation Analysis are described. Secondly, Large-Sample Neutron Activation Analysis is summarized. This is followed by the scope of the thesis and an overview of its contents.

1.1 Neutron Activation Analysis

1.1.1 principles

Neutron Activation Analysis (NAA) is a technique to determine amounts of elements in a sample. It is based on the following principle:

An atomic nucleus exposed to a unity neutron flux of neutrons of energy E_n has an isotope-specific probability per unit time of absorbing a neutron ($\sigma(E_n)$). The reaction product may be unstable, i.e. radioactive, and the process is therefore called “activation”. In that case, it then decays with a probability of λ per second to a stable or another unstable nucleus by emission of isotope specific radiation. This

radiation usually involves charged particles (β^- or β^+) and there is also a probability γ of emitting gamma rays of a certain, discrete energies.

The activity A [Bq] of a directly produced radionuclide, with decay-constant λ [s^{-1}] in an infinitely small sample containing a mass w [g] of a specific element with target-isotope abundance θ , neutron-energy E_n [J] dependent activation cross-section $\sigma(E_n)$ [m^2] immediately after irradiation-time t_{ir} [s] in neutron-energy dependent neutron-flux $\Phi(E_n)$ [$m^{-2}s^{-1}J^{-1}$] is:

$$A(t_{ir}) = \int_{E_n=0}^{\infty} \Phi(E_n)\sigma(E_n)dE_n \frac{N_{Av}\theta w}{M} (1 - e^{-\lambda t_{ir}}) \quad (1)$$

with $N(t)$ the number of atoms of the specific radionuclide, N_{Av} Avogadro's number [$6.022 \times 10^{23} \text{ mol}^{-1}$] and M the atomic mass [g/mol].

The number of atoms decaying during measurement time t_m [s] after waiting time t_d [s] is:

$$N(t_m, t_d, t_{ir}) = e^{-\lambda t_d} A(t_{ir}) \int_0^{t_m} e^{-\lambda t} dt = e^{-\lambda t_d} A(t_{ir}) \frac{1 - e^{-\lambda t_m}}{\lambda} \quad (2)$$

If gamma-rays with energy E_γ [J] are emitted with a probability $\gamma(E_\gamma)$ per decay event and are detected in the full-energy peak with an energy-dependent efficiency $\varepsilon(E_\gamma)$, then Equation 1 and 2 combined give the number of gamma-rays detected in the full-energy peak by:

$$A(E_\gamma) = \int_{E_n=0}^{\infty} \Phi(E_n)\sigma(E_n)dE_n \frac{N_{Av}\theta w}{M} (1 - e^{-\lambda t_{ir}}) e^{-\lambda t_d} \frac{1 - e^{-\lambda t_m}}{\lambda} \gamma(E_\gamma) \varepsilon(E_\gamma), \quad (3)$$

with $A(E_\gamma)$ the area of the detected full energy peak. Equation 3 shows that the number of gamma-rays detected in a photo-peak is proportional to the amount of that specific element. This is under the assumptions that only the gamma-rays of the specified element* contribute to this full-energy peak and the peak area is corrected for dead time of the detector.

* In fact the gamma rays originate from the radionuclide produced by neutron irradiation of the element. In this thesis, both terms radionuclide and element are used, where the amount of the element is the parameter of interest and the radionuclide is the source of the gamma rays.

In standard NAA, Equation 3 is often used, even though in practice, samples are not that small: even at sample masses of about 100 mg and dimensions of a few mm, the peak area will be influenced by neutron self shielding (the inner atoms are shielded from the neutron source by the outer atoms), neutron-flux gradients over the sample and self-absorption of gamma rays (photons may be absorbed within the sample). Equation 3 needs to be corrected for these effects as well as for dead-time of the detector.

Finally, if the sample is inhomogeneous, then w , Φ and ε have to be considered as a function of position in the sample. This effect of inhomogeneity is studied in this thesis for large samples (with volumes ranging from 1 litre to 15 litres, or 1 to 15 dm³).

1.1.2 Origin and optimisation of the technique

Activation of elements by bombardment with neutrons was discovered by Fermi in 1934 [1] and soon thereafter (1936) applied by De Hevesy as an analysis technique [2], nowadays known as Neutron Activation Analysis. From the beginning this technique was considered very powerful due to its matrix insensitivity and element-specific response.

At first Ra-Be mixtures were used as neutron source, but with the development of the nuclear reactor, a powerful neutron source has become available [3], yielding substantially larger neutron fluxes and hence allowing for the determination of lower concentrations or the analysis of smaller samples.

For detection, first the Geiger-Müller counter was used for counting both β - and γ -rays, without energy resolution, so elements were identified based on half-lives and chemical separations performed after the irradiation. This is called Radiochemical NAA (RNAA).

The development of NaI scintillation detectors introduced the possibility of measuring a gamma-ray spectrum with an energy resolution of some 4 % at 1 MeV, which was improved when Ge(Li) semiconductor material was used for detection [4] with a resolution of some 0.1 % at 1 MeV at present. The introduction of the gamma-ray detectors with energy resolution allowed for analyses without chemical separation, i.e. Instrumental NAA (INAA).

In the following decades, NAA gained importance as an analysis technique. Though in the last two decades the share in trace-element analyses is declining

due to competing non-nuclear analysis techniques, for some special cases activation analysis still offers unique capabilities. The high penetration power of both neutrons and gammas is exploited in Large-Sample Neutron Activation Analysis (LS-NAA), that was developed at the Interfaculty Reactor Institute [5]. Further development of this technique is the subject of this thesis.

Nowadays, NAA of normal-size samples (up to a few grams) is a mature technique that can be used in routine applications. It is known as (1) highly accurate, (2) matrix independent (3) multi-element (4) with low detection limits for some elements; *i.e.* varying between 0.0006 and 10 mg/kg for 40 elements [6]. In Table 1 (from [7]), a qualitative comparison of some analysis techniques applied in petroleum analysis is given, which shows that INAA approximates the ideal analysis technique in many respects.

Still, some challenges remain. One of them affects all currently available analysis techniques: the problem of representativeness of the sample when dealing with inhomogeneous bulk material.

One way to overcome this problem is to analyse large samples. Most techniques do not allow for large samples (kg level) because the activating signal or the response (or both) cannot penetrate samples of that size, or the technique is destructive and cannot handle such large amounts.

NAA, though, has highly penetrating neutrons as incoming signal and highly penetrating gamma-rays as signal to be detected. This makes NAA (in principle) a

Criteria	Ideal	AAS	ICPAES	ICPMS	NAA	SSMS	XRF	IC
Sensitivity	++	+	++	++	++	++	+	+
Dynamic Range	++	-	++	++	++	-	++	++
Precision	++	++	+	+	++	--	+	+
Interferences	+++	+	++	++	+	--	+	+
Sample Preparation	++	+	+	+	++	+	+	-
Price	low	x	5x	10x	2x	5x	10x	x
Applications	++	++	++	-	+	-	++	-
Elements	+++	++	++	++	++	+++	+	-
Multielements	+	-	+	+	+	+	+	+
Turnaround	+++	++	++	++	+/-	-	++	++
Nondestructive	+	-	-	-	+	-	+	-

Table 1 From R.A. Nadkarni [7] p 48, table 16: How close do available methods approach the “ideal method” for petroleum analysis? The price assumes that the equipment (like a nuclear reactor for NAA) is readily available.

suitable technique for the analysis of such large samples.

The only competing technique is Photon Activation Analysis (PAA) [8], due to high penetration depth of the activating energetic photons (20-150 MeV). In PAA, the number of detectable elements is more limited than in INAA, because the achievable activation rates tend to be substantially smaller than in NAA. PAA has not been as widely used as NAA mainly due to the limited availability of suitable photon sources [9].

LS-INAA requires special facilities for activation as well as for detection. At the Interfaculty Reactor Institute, both have been developed.

1.2 LS-NAA

1.2.1 Facilities

Large Samples up to 13 dm³ can be handled with current facilities. Samples are activated in the BISNIS facility of the Interfaculty Reactor Institute. A cross-section diagram of that facility is shown in Figure 1.

The sample is placed in an irradiation container that can contain samples up to 100 cm length and 13 cm diameter. The sample can be rotated during irradiation. The sample is surrounded by neutron flux monitors positioned in a fixed grid, as drawn in Figure 1. The empty space in the container is filled with graphite to have a well defined medium for the neutron transport calculations.

The measurement facility is shown in Figure 2. The detector is surrounded by a 10-cm lead shielding. The sample-to-detector distance is 20 cm, which is large as compared to typical NAA counting geometries, to prevent true coincidence summing effects, and also to reduce inaccuracy due to inhomogeneity. Inaccuracy due to inhomogeneity can be further suppressed by rotating the sample during irradiation and measurement.

1.2.2 Methods

In LS-NAA it is assumed that inhomogeneity of the sample does not influence the analysis significantly. Now, Equation 3 can still be used with the addition of corrections for neutron self-shielding and for the position-dependent

gamma-ray detection efficiency due to self-attenuation of the sample and distance to the detector. Since at the irradiation position the ratio of thermal over non-thermal neutrons is 250, the neutrons can be considered to be thermalised (a Maxwellian distribution with a maximum at room temperature of 0.025 eV) and the integral over the neutron energy can be approached by a constant for the neutron flux Φ_{th} and activation cross section σ_{th} , because in the thermal column:

$$A(E_\gamma) = \int_{\substack{\text{Sample} \\ \text{Volume}}} \varepsilon(E_\gamma, \vec{r}) \Phi_{th}(\vec{r}) w(\vec{r}) d\vec{r} \sigma_{th} \frac{N_{Av} g}{M} (1 - e^{-\lambda t_{ir}}) e^{-\lambda t_d} \frac{1 - e^{-\lambda t_m}}{\lambda} \gamma(E_\gamma) \quad (4)$$

The gamma radiation emitted by the sample is measured before irradiation to determine the initially present radioactivity. Next a ^{152}Eu point source is placed behind a pinhole collimator for a transmission measurement to determine the attenuation coefficients for gamma-rays in the sample.

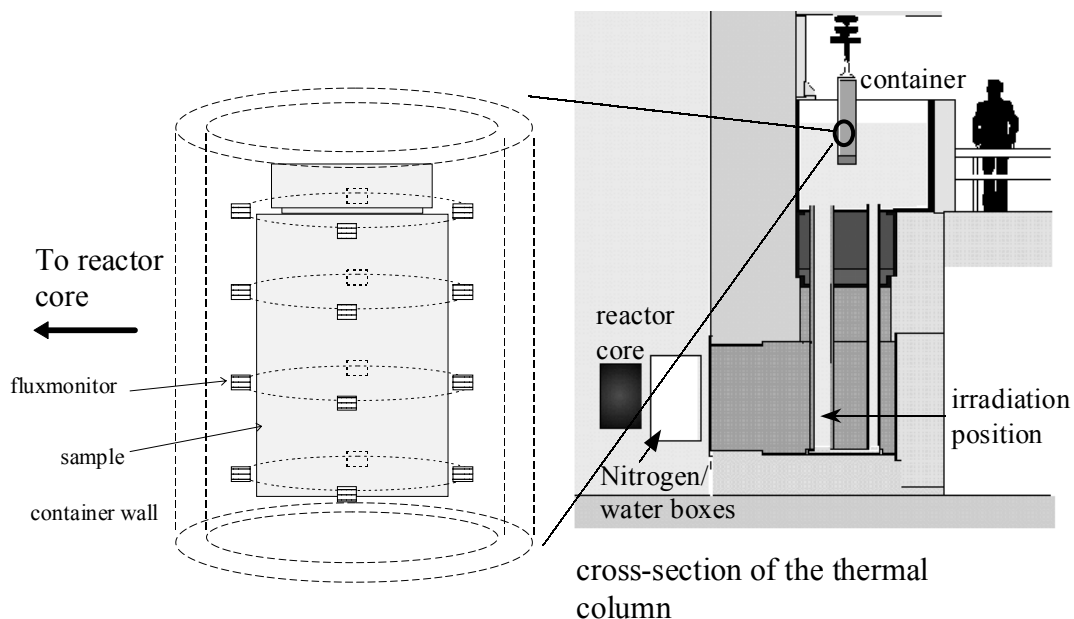


Figure 1 Cross section of the BISNIS irradiation facility for large samples at the Interfaculty Reactor Institute. Before irradiation, the nitrogen/water boxes are filled with nitrogen to enlarge the neutron flux in the facility. The neutrons in the irradiation tube are completely thermalised after the 1.4m carbon layer. The container at the irradiation position is surrounded by 3 mm of water, the bypass system serves for the water displacement. For explanation of all terms see [5,10]. The left part of the figure shows a sample inside the container, surrounded by Zn neutron flux monitors.

The sample is placed in the irradiation container and is surrounded by flux monitors, to determine the flux at several positions outside the sample. From the flux distribution outside the sample the flux distribution inside the sample can be derived, as shown by Overwater [5].

After a waiting time, the sample is measured, rotating in front of the detector. For the main gamma-ray energies of ^{152}Eu , the Large Sample correction factor is determined by a Monte Carlo simulation of a sample activity distribution proportional to the neutron flux distribution. For other gamma-ray energies, the correction factor is interpolated using a cubic spline. After this correction, the analysis proceeds as in normal INAA, as if the sample were infinitely small.

1.2.3 Limitations on detection limits

With LS-NAA the maximum sample size has been increased by a factor of at least 10^4 : from less than 1 g to about 10 kg. On the other hand, the average neutron flux in the BISNIS facility is about a factor of 10^4 lower than in the facilities normally used for INAA. This means that for an equal concentration of an element

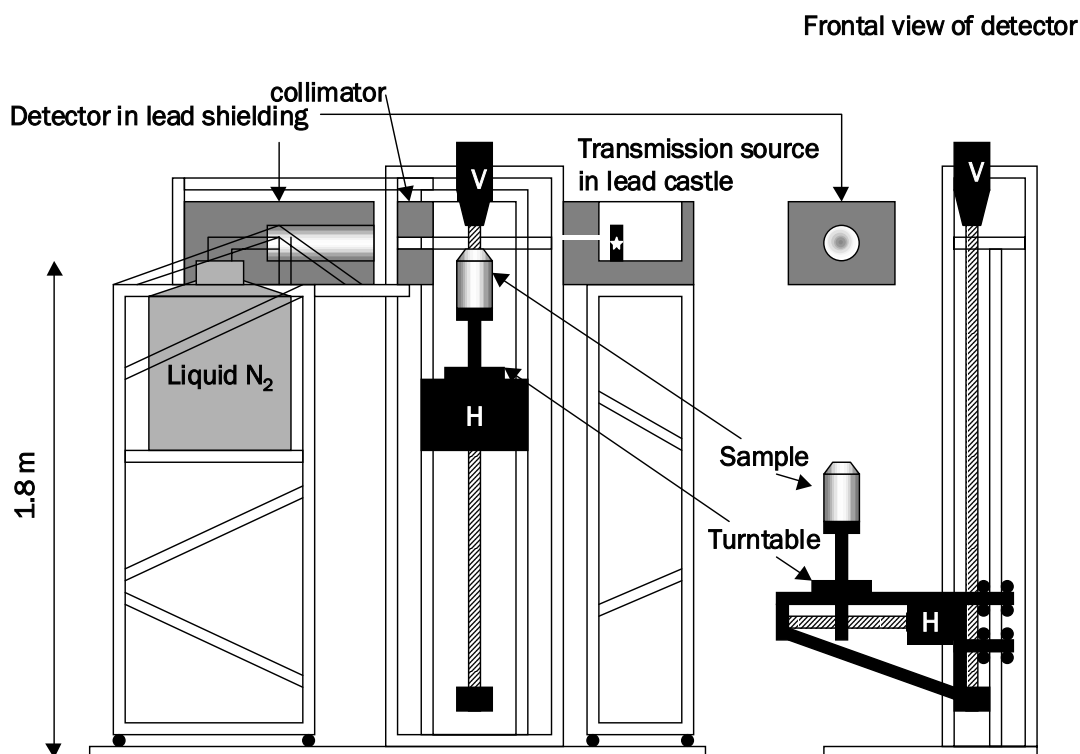


Figure 2 Sample measurement system consisting of a detector in a stand, a sample rotator and translator and a transmission source stand.

in a LS-NAA sample and in an INAA sample the peak area will be the same given an equal detection efficiency and other analysis parameters. However, this detection efficiency will be lower for LS-NAA due to the larger sample detector distance and especially for low-energy gamma-rays due to the self-shielding. This means that, everything else remaining the same, the detection limits are somewhat higher for LS-NAA than for INAA. Furthermore, elements determined with INAA exclusively through very short-lived radionuclides can not be determined with LS-NAA, since the LS-NAA irradiation container can only be opened by hand and needs some hours decay time before its radioactivity is at a reasonable level to be handled by man.

1.2.4 Limitations on accuracy

Though LS-NAA has been introduced to analyse inhomogeneous samples, still some extreme cases of inhomogeneity may occur that deteriorate the accuracy of the results of the measurement, because they affect the measurement without being observed and hence without being corrected for. Overwater studied some types and geometries of extreme inhomogeneities and their error propagation [10]. His study shows that in general inhomogeneities affecting the gamma-ray attenuation have larger effects than inhomogeneities affecting the neutron attenuation. The largest inaccuracies are found for inhomogeneous distributions of the elements to be determined themselves. They may cause the analysis results to be off by a factor of 2. Moreover, in cases of extreme inhomogeneities, it is questionable whether a correct average over the entire sample provides sufficient information.

1.3 Scope of the dissertation work

The limitations of LS-NAA mentioned above made clear that extremely inhomogeneous large samples required new analysis methods. These methods should not only provide a more accurate average result for the element concentration, but also information about the nature and degree of inhomogeneity of the sample. Therefore, this thesis work was started to develop methods for detection and correction for inhomogeneities and Reconstruction of Element Distributions in Neutron Activated Inhomogeneous Large Samples: (REDNAILS).

With these methods more accurate LS-NAA results can be obtained. Also, the element distribution itself can be used for further interpretation. This will be discussed in the general discussion of this thesis.

1.4 Contents of the thesis: Neutron Activation Analysis of Inhomogeneous Large Samples

The method developed is divided in mutually dependent steps corresponding to thesis chapters.

In Chapter 2, the meaning of the terms inhomogeneity and sample representativity is discussed. This chapter is introductory to the thesis work and gives a basis to the further use of these terms.

Chapter 3 gives the framework and constraints of the thesis work (the design of a method for neutron activation analysis of inhomogeneous large samples) and describes the steps in the design of the method that are not part of this thesis work. It points to Chapters 4 through 9 for those parts that constitute the thesis work.

Chapter 4 describes the method developed for determination of the source position and energy dependent gamma-ray detection-efficiency. This method is applied in Chapter 5 for optimisation of the measurement set-up.

The measurement facility is used in the method described in Chapter 6 for a quick determination of the inhomogeneity of the sample.

Chapter 7 discusses a method for determination of the position and gamma-energy dependent gamma-ray attenuation coefficient.

In Chapter 8 algorithms for reconstruction of the element distribution from the measurements are discussed and tested with a few simple samples. This is followed by a test with samples of practical interest in Chapter 9.

The thesis work and its resulting methods as a whole are discussed in Chapter 10.

1.5 References

1. E. Fermi, Radioactivity Induced by Neutron Bombardment, *Nature* 1934, 757
2. G. Hevesy, H. Levi, *Kgl. Danske Videnskab. Selskab Math-fys.* 14 (1936) 3-34

3. G.E. Boyd, *Anal. Chem.* 21 (1949) 335-347
4. N.A. Bailey, R.J. Grainger, J.W. Mayer, *Rev. Sci. Instrum.* 32 (1961) 865
5. R.M.W. Overwater, *The physics of Big Sample Instrumental Neutron Activation Analysis*, thesis, Delft 1994
6. P. Bode, *Instrumental and organizational aspects of a neutron activation analysis laboratory*, thesis, Delft 1996
7. R.A. Nadkarni 'Modern Instrumental Methods of Elemental Analysis of Petroleum products and Lubricants', *ASTM 1109* (1991), 48
8. D. Schulze, W. Heller, H. Ullrich, H. Krupsch, C. Segebade, *J. Radioanal. Nucl. Chem.* 168 (1993) 385-392
9. W.D. Ehman, D.E. Vance, *Radiochemistry and Nuclear Analytical Methods of Analysis*, John Wiley & Sons Inc., New York, 1991
10. R.M.W. Overwater, P. Bode, *Computer simulations of the effects of inhomogeneities on the accuracy of large sample INAA*, *Appl. Radiat. Isot.* 49 (1998) 967-976
11. P.M. Gy, *Sampling of Particulate Materials, Theory and Practice*, Elsevier Scientific Publishing Company, Amsterdam, 1979
12. M. Stoepler (Ed.), *Sampling and Sample Preparation*, Springer Verlag, Berlin, 1997
13. M. Blaauw, *The Holistic Analysis of Gamma-ray Spectra in Instrumental Neutron Activation Analysis*, thesis, Delft 1993
14. N.M. Spyrou, J.M. Sharaf, S. Sarkar, *J. Radioanal. Nucl. Chem.* 167 (1993) 453-465

Chapter 2

Sampling, homogeneity and representativity

2.1 Introduction

In general, when a sample is taken from a larger amount of material, the probability of it having exactly the same composition as the larger amount is negligible. So, if a sample is to represent exactly the total population it was taken from in order to be representative, representative samples in that strict sense do not exist. In practice though, representativity is not defined that strict. Often, a sample is considered to be representative without any check at all. All this means that the degree of inhomogeneity and the degree of representativity are the quantities of interest, and that we need quantitative definitions for them.

In the theoretical discussion in this chapter we assume that the analysis is free from any analytical error. A sample is defined as a randomly selected set of subsamples from a batch with a random distribution of inhomogeneities in the batch.

2.2 Definitions

2.2.1 Homogeneity of the batch

A literature study reveals different definitions of homogeneity. An early qualification of homogeneity was given by Kratochvil and Taylor [1]: “The degree to which a property or substance is randomly distributed throughout a material.” According to Kratochvil and Taylor, homogeneity depends on the size of the units

under consideration. Thus, in their opinion, a mixture may be inhomogeneous at the molecular or atomic level, but homogeneous at the particulate level.

Another, more quantifiable, definition of homogeneity has been proposed by Buslik [2]: “the negative log of the sample weight (g) required to obtain a standard deviation of 1%”(most likely in a series of subsamples). This is related to the homogeneity index available in pharmaceutical practice: “the ratio of the standard deviation of a number of tablets measured in practice during the mixing operation, to the required standard deviation” [3].

The latter definitions are more objective. However, application requires the relation between the relative standard deviation and sample size, which is often unknown. An attempt to solve this problem mathematically was undertaken by Gy [4]. A sample is analysed on property a . Dividing the batch in grains and representing the sample drawing process as repeated Bernoulli experiments for every grain, he derived the relation between the sample-to-sample variance of property a in the batch $V(a_{sample})$ and the inhomogeneity of the batch G_{batch} , inversely proportional to the previously defined homogeneity,

$$G_{batch} \equiv M_{sample} V(a_{sample}) \quad (1)$$

where M_{sample} is the sample mass and $V(a_{sample})$ is defined as:

$$V(a_{sample}) = \frac{1-q}{qM_{batch}^2} \sum_{k=1}^{N_{batch}} m_k^2 (a_k - a_{batch})^2 \quad (2)$$

where M_{batch} is the mass of the batch, N_{batch} is the number of batches, q is the probability that a grain with the specific property a is selected in the sample, and k is the sample number.

The applicability of Gys definitions to sampling in practice is somewhat complicated. His mathematical way of sampling is not really applied in analytical chemistry and, from the definitions, it is clear that Gy is considering measurement uncertainties to be negligible.

2.2.2 Representative sampling

The term “representative sample” is often used to denote a single sample from a population or batch that can be expected to exhibit the average properties of the batch. This definition would only appear to apply in two cases: i) samples a

priori defined to be representative for a specific purpose or ii) the sampling of truly homogeneous materials [1].

In this study no *a priori* representative samples are considered. Representativity is directly related to homogeneity. Secondly, truly homogeneous materials are not common in normal sample analysis. Therefore, the representativity of the sample is often defined as the agreement between sample and batch properties in view of the reported uncertainties of the sample properties.

Some factors influencing the degree of representativity of a sample are: the sample size, the inhomogeneity of the batch (or sample if that influences the results), the method of sampling and the required precision or reported uncertainties. In this discussion, we only consider the first two factors.

Current trace-element analysis techniques, e.g. AAS, INAA, ICP-MS, determine concentrations in small aliquots, typically ranging from 1 mg to 10 grams. Obtaining a representative aliquot from a bulk sample typically collected or offered for analysis may become problematic when the material is difficult to homogenise. Sampling uncertainties are almost always the greatest source of analytical error in environmental trace-element measurements and are often significant in other microanalyses [5].

The representativity of a sample is related to its inhomogeneity, representativity may be established by measuring the inhomogeneity. This is not possible with current techniques, which only determine the overall sample concentration. Therefore, homogeneity and representativity are often established by analysing a series of randomly collected samples, yielding the mean and variance of certain properties.

We define representativity of a sample as the reciprocal of the between-samples variance V :

$$R \equiv 1/V \quad (3)$$

If the between-sample variance is zero, the representativity of each sample is infinite, and vice versa. Here, we assume again that there is no analytical error.

2.2.3 Discussion

Buslik's definition appears to be flawed: A noisier measurement method would result in a lower homogeneity number. Also the 1 % in there is arbitrary.

Gy's definition $G \equiv MV$ makes sense, if the between-sample variance in concentration is taken to denote the true variance, meaning that the observed variance must have been corrected for the variance contribution from the measurement method. Note that estimation of V will require analysis of a number of samples.

So in this study $G \equiv MV$ and $R \equiv 1/V$ are proposed as the definitions for homogeneity of the batch and representativity of the sample respectively.

The best estimate for a property of the material the samples were taken from is the average M over the samples. The 1 s.d. confidence interval c (as in $M \pm c$) for the material property would then be the standard error of the mean, given by

$$c = \sqrt{V/N} = 1/\sqrt{RN} \quad (4)$$

with N denoting the number of samples.

2.3 Sampling in practice

2.3.1 Example 1: Sampling a large area.

In the field, someone fills a bucket with mud by walking around in the terrain to be sampled and taking bits of material every here and there. The bucket as a whole might be homogenised, and a 1 g subsample taken for analysis by AAS, ICP-MS or INAA. Even if the analysis technique would be a negligible source of uncertainty in the measured concentration, the final result would be of limited significance with respect to the terrain sampled, because there would be no estimate of between-sample variance and therefore no estimate of sample representativity. So the bucket must be divided in say 10 portions without homogenisation, and each portion homogenised and analysed. Roughly this procedure is prescribed in the Dutch norm for environmental sampling of e.g. future construction sites [5].

The analysis result of the whole bucket, through homogenisation and the taking of a single small subsample assuming inhomogeneities on only a cm scale, is comparable to the “Overwater” LS-INAA analysis result. LS-INAA has the advantage that homogenisation and subsampling are no longer needed [7,8,9]. On the other hand it should be noted that in LS-INAA, not all parts of the sample are irradiated with the same neutron flux, and not all parts are counted with the same detection efficiency [10]. Rotational and most of the radial differences in neutron flux and gamma-ray detection-efficiency can be smoothed by rotation of the sample during measurement, but a vertical difference in sensitivity remains. Both neutron flux and gamma-ray detection-efficiency have their maximum at the vertical centre of the sample and both can be approximated with a $\cos(\alpha(x-x_0))$ function [4]. So if LS-INAA is considered as an averaging or smoothing technique, the result is biased towards the vertical centre of the sample. This is illustrated in Figure 3 and Figure 4, where this product of flux and efficiency is described by a filter and compared to the true average described by a box filter.

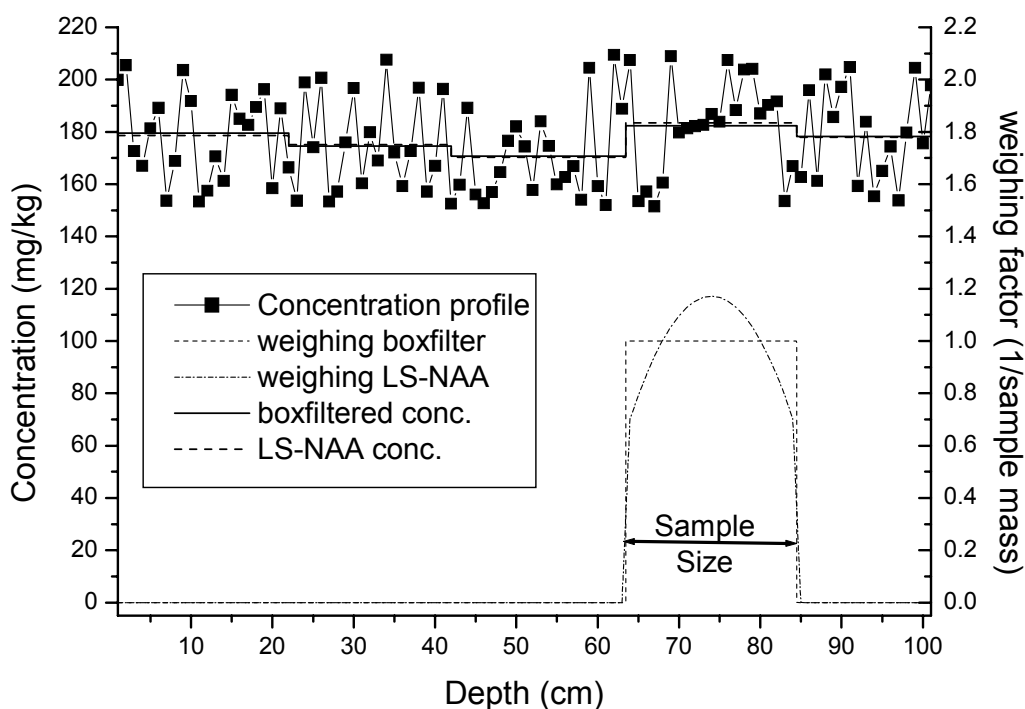


Figure 3 Simulated results for averaging of a randomly distributed concentration profile with a box-filter and with a filter with the same profile as LS-INAA. Both filters render almost the same profile.

In Figure 3, the box filter and LS-INAA shape filter are compared for a spatially randomly distributed property. It indicates that for such a random distribution both filters give almost the same result. In fact, only for these cases LS-INAA gives correctly smoothed results.

Figure 4 shows the comparison between the two filters for a spiked distribution. In this example, this results in a difference of 10%.

The previously mentioned procedure of division in 10 portions before homogenisation is comparable to REDNAILS. If the element distributions in the bucket can be considered to be randomly inhomogeneous, the Equations in Section 2.2 can be applied to obtain estimates for the homogeneity of the material and the representativity of the sample. Activation analysis techniques have the useful property that the contribution of the counting statistics to the final concentrations can be determined, so that between-sample variation can be corrected for that. Other sources of error are difficult to correct for.

Ordinary LS-INAA is applicable only if it can be assumed that the amount of material in the bucket is sufficient to achieve the required sample representativity,

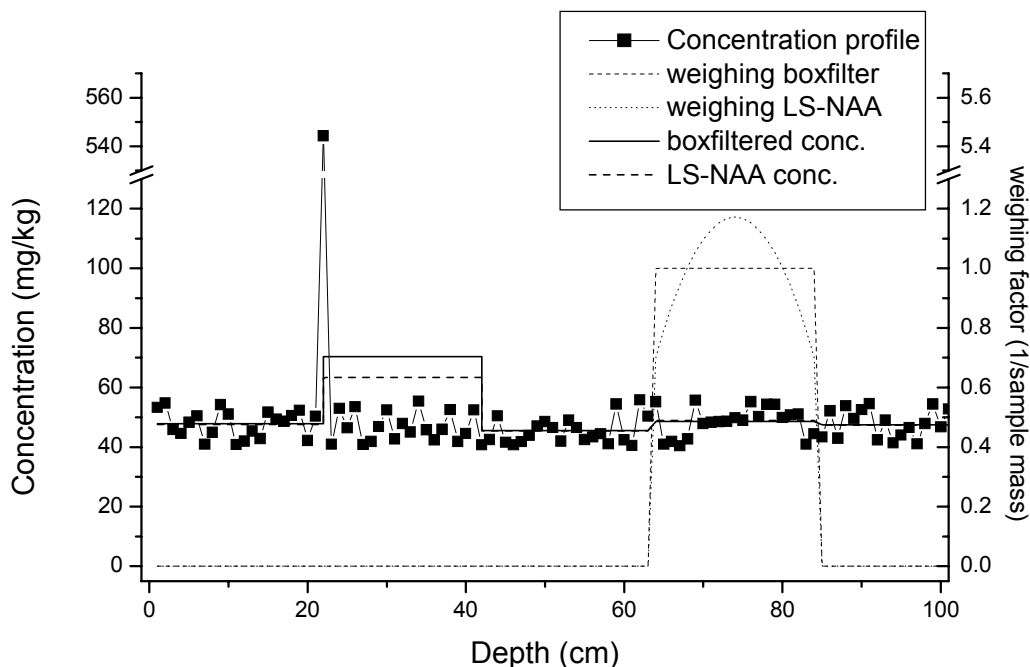


Figure 4 Simulated results for averaging of a randomly distributed concentration profile having one spiked extremely high concentration, with a box-filter and with a filter with the same profile as LS-INAA. Both filters render almost the same profile.

for example because of previous experience with the material.

2.3.2 Example 2: drill core

A ditch bottom sample is taken by freezing and taking an unperturbed drill core. Or a drill core is taken from a rock. Due to the layered structure, the sample is not randomly inhomogeneous, and the previous discussion of representativity and inhomogeneity probably does not apply. In that case, with REDNAILS, the spatial element distributions can be determined and reported as a kind of tomographic result. To improve the quality of the solution, all the pre-existing knowledge about the sample and its origin in the analysis procedure can be used.

2.4 Discussion

Like other analysis techniques, LS-INAA also requires some rough knowledge about the sample content. High concentrations of neutron or gamma absorbing elements like respectively boron or lead should be avoided.

Extreme cases of matrix inhomogeneity would often not come as a surprise to the analyst using LS-INAA. There will be some information about the possible inhomogeneity of the material that made the analyst decide to use LS-INAA, e.g. previous inhomogeneous samples of the same origin and also optical examination may reveal a certain structure of the sample. For many types of material, the level of homogeneity and the probability of extreme inhomogeneities can be estimated, based on previous analyses. E.g. soil, waste and biological materials are known for their inhomogeneity [11]. REDNAILS will be mainly applied to geological samples. These samples may be the result of vertical cylindrical bore hole logging through material that has been deposited over a wider area in successive periods of time. This means that these samples are expected to have a typical layered structure.

Inhomogeneity of matrix elements and density can be deduced from the neutron-flux measurements or gamma-transmission measurements which are applied to determine respectively the neutron and gamma-ray self-attenuation. However, such measurements do not give insight in trace-element inhomogeneities of the current sample.

2.5 Conclusions

In this chapter, the problem of representative sampling in the analysis of inhomogeneous bulk has been indicated. Though different definitions for inhomogeneity of the sample can be derived from literature, it can be described in a quantifiable way using the definition of Gy (Equation 1), where the inhomogeneity of a sample for a certain property is related to the variance of that property over a set of subsamples, assumed that the analytical error is negligible and that the rules of a normal distribution of the determinant may be applied.

As discussed in [7,8,9] and Section 2.3.1, for real samples, LS-INAA is especially suited for non-destructive determination of average concentrations in samples that are inhomogeneous on a cm scale. Disadvantages are (i) that extreme inhomogeneities may deteriorate the accuracy of the results, (ii) that no standard deviation is known, and hence the inhomogeneity is still unknown. (iii) Finally, in some cases the average of a property is not the parameter of interest, e.g. in gold mining or waste treatment one may be interested in the hot spots.

As discussed in Section 2.3.2 and 2.4, in certain practical cases, existing knowledge about the sample may help to decide to perform an analysis of the spatial distribution of a property. Especially where a certain structure in the bulk is foreseen, a spatial analysis is preferred. REDNAILS can be applied to this end.

Now, if the element distribution in the large sample is determined for instance by analysis of the sample in subsamples or voxel by voxel, the sample-to-sample variance and the sample representativity can be estimated. This is what REDNAILS has to offer as an additional advantage over LS-INAA.

2.6 References

1. B. Kratochvil, J.K. Taylor, Sampling for chemical analysis, *Anal. Chem.* 53 (1981) 924-936
2. D. Buslik, A proposed universal homogeneity and mixing index, *Powder Tech.* 7 (1973) 111-116
3. J.A. Hersey, Assessment of homogeneity of powder mixtures, *J. Pharm. Pharmacol.* 19 (1967) 168S-176S
4. P.M. Gy, *Sampling of particulate materials, theory and practice*, 1st edition, Elsevier, Amsterdam 1979

5. B. Kratochvil, Sampling for microanalysis: Theories and strategies, *Fres. J. Anal. Chem.* 337 (1990) 808-811
6. NEN 5740. Soil investigation strategy for exploratory survey – investigation of the environmental quality of soil and soil lots, Nederlands Normalisatie Instituut, Delft 1999
7. M. Blaauw, O. Lakmaker, P. van Aller, *Anal. Chem.* 69 (1997) 2247-2250
8. P. Bode, O. Lakmaker, P. van Aller, M. Blaauw, *Fresenius J. Anal. Chem.* 360 (1998) 10-17
9. R.M.W. Overwater, P. Bode, J.J.M. De Goeij, J.E. Hoogenboom, *Anal. Chem.* 68 (1996) 341-348
10. R.M.W. Overwater, P. Bode, Computer simulations of the effects of inhomogeneities on the accuracy of Large Sample INAA, *Appl. Radiat. Isot.* 49 (1998) 967-976
11. P. Bode, R.M.W. Overwater, J.J.M. De Goeij, *J. Rad. Nucl. Chem.* 216 (1997) 5-11
12. M. Stoepler (Ed.), *Sampling and Sample Preparation*, Springer Verlag, Berlin 1997

Chapter 3

Reconstruction of Element Distributions in Neutron Activated Inhomogeneous Large Samples

3.1 Introduction

In this chapter a general introduction is given to REDNAILS. First the underlying theory is presented. Next, the experimental facilities and the procedures for calibration and measurement are described. Finally, the methods for data processing are introduced. The parts supported by experiments are further described and discussed in following chapters.

As described in Chapter 1, the work in this thesis is about the design of a method to analyse large samples, using neutron activation analysis, that are too inhomogeneous to be analysed correctly using Overwater's methods. Instead of integral measurements of the sample, the sample has to be scanned in some way to determine the spatial distribution of the induced radioactivity.

The reconstruction of the element distributions from the spectra obtained in a sample scan can be compared, to some extent, to energy resolved tomography like Neutron Induced Gamma Emission Tomography (NIGET) [1], scanned measurements of radioactive waste barrels [2] and scans of nuclear reactor fuel rods or pallets [3,4]. However, the constraints are now that the reconstruction method should be applied to (i) spectra measured with a germanium detector, (ii) spectra of samples with low radioactivity (iii) situations with significant gamma self attenuation. Moreover, (iv) not the spatial distribution of the radioactivity is of primary interest, but the spatial distribution of elements giving rise to this

radioactivity, and due to the neutron self attenuation, there is no fixed ratio between element concentrations and corresponding induced radioactivity.

Compared to normal tomography, there are a few unfavourable experimental facts: (i) the gamma-ray energy cannot be optimised since it cannot be freely chosen, (ii) the measurement set-up cannot be optimised for one gamma-ray energy and (iii) the radioactivity of the sample is much lower, in the order of about 100 kBq/kg. Due to these effects, the results of the scanned measurements will be blurred and noisy. Hence, emission tomography based on a Radon Transform or filtered back-projection will not render proper results.

On the other hand, the gamma-ray spectra in LS-NAA spectra have some advantageous features: all parameters in Equation 4 of Chapter 1 except the element distributions are known, and the ratio of peaks stemming from radionuclide(s) produced from the same element can be employed as well. This advantage is used at best in the so-called 'holistic approach'[5]. Therefore this approach is the basis for the method described here.

3.2 Theory

3.2.1 NAA basis

The basic equation for NAA describing activation, decay, gamma-ray emission and detection for a sample consisting of one element, with negligible neutron and gamma-ray self attenuation is:

$$A(E_\gamma) = \int_{E_n=0}^{\infty} \Phi(E_n) \sigma(E_n) dE_n \frac{N_{Av} \theta w}{M} (1 - e^{-\lambda t_{ir}}) e^{-\lambda t_d} \frac{1 - e^{-\lambda t_m}}{\lambda} \gamma(E_\gamma) \varepsilon(E_\gamma), \quad (1)$$

where $A(E_\gamma)$ is the peak area at energy E_γ [J], $\Phi(E_n)dE_n$ is the flux for neutrons with energies between E_n and $E_n + dE_n$ incident on the sample [$s^{-1}m^{-2}J^{-1}$], $\sigma(E_n)$ is the neutron capture cross section [m^2], N_{av} is Avogadro's number ($6.022 \times 10^{23} \text{ mol}^{-1}$), θ is the isotopic abundance, w is the mass of the element in the sample [g], M is the atomic mass of the element [g/mol], λ is the decay constant of the radioactive atoms produced [s^{-1}], t_{ir} is the irradiation time [s], t_d is the time in between irradiation and measurement [s], t_m is the measurement time

[s], $\gamma(E_\gamma)$ is the probability of a photon of energy E_γ being emitted in the decay, and $\varepsilon(E_\gamma)$ is the probability of detection of the photon.

This equation can be used straightforwardly to predict full energy peak areas for each element. The fitting of these predicted peak areas to the measured areas directly renders the element concentrations, typically by finding the optimum solution to an overdetermined system of linear equations in the least-squares sense. This procedure is called the “holistic approach”[5] because the interpretation is performed in one step (with no intermediate results), thereby taking optimal advantage of the existing knowledge about the analysis technique and element properties.

Neutron and gamma-ray self attenuation cannot be neglected in LS-NAA. Therefore, the NAA-equation 1 changes to [6]:

$$A(E_\gamma) = \int_{\text{Sample Volume}} \int_{E_n=0}^{\infty} \Phi(E_n, \vec{r}) \sigma(E_n) dE_n \frac{N_{Av} \theta w(\vec{r})}{M} (1 - e^{-\lambda t_{ir}}) e^{-\lambda t_d} \frac{1 - e^{-\lambda t_m}}{\lambda} \gamma(E_\gamma) \varepsilon(E_\gamma, \vec{r}) d\vec{r} \quad (2)$$

In Equation 2, the density distribution of the element w , the neutron flux Φ and the detection efficiency $\varepsilon(E_\gamma)$ are integrated over the sample volume. For normal LS-NAA as developed by Overwater, it was assumed that the sample was homogeneous ($w(r) = w$) or that inhomogeneities could be averaged out, so that:

$$A(E_\gamma) = \int_{\text{Sample Volume}} \int_{E_n=0}^{\infty} \Phi(E_n, \vec{r}) \sigma(E_n) dE_n \frac{N_{Av} \theta w}{M} (1 - e^{-\lambda t_{ir}}) e^{-\lambda t_d} \frac{1 - e^{-\lambda t_m}}{\lambda} \gamma(E_\gamma) \varepsilon(E_\gamma, \vec{r}) d\vec{r} \quad (3).$$

Effects of inhomogeneity occurring in reality were averaged out or minimised by rotating the sample during irradiation and measurement. Hence if the integration was possible (*i.e.* the attenuation parameters were known), the holistic approach could be applied.

3.2.2 Sample scanning of extremely inhomogeneous samples

Large samples may sometimes contain extreme inhomogeneities such as layers or nuggets. It has been shown [7,8] that in such cases the assumption of macroscopic homogeneity and use of Equation 3 leads to results that may be off by a factor of 2 or more. To overcome this source of error and also to determine

(sometimes requested) distributions of elements non-destructively, sample scanning is introduced in LS-NAA, where the sample is thought to consist of volume elements that individually are considered homogeneous.

The sample is considered to be consisting of N voxels, to be scanned in L measurements, where each measurement is taken from a different position relative to the sample. Equation 2 evolves to an array of equations, giving for the contribution to area A from voxel i in scan-measurement j :

$$A_{ij}(E_\gamma) = \int_{\text{Vol.}=0}^{\text{voxel } E_n} \int \Phi(E_n, \vec{r}_i) \sigma(E_n) dE_n \frac{N_{Av} \vartheta w(\vec{r}_i)}{M} (1 - e^{-\lambda t_{ir}}) e^{-\lambda t_{d,j}} \frac{1 - e^{-\lambda t_{m,j}}}{\lambda} \gamma(E_\gamma) \varepsilon_j(E_\gamma, \vec{r}_i) d\vec{r}_i, \quad (4)$$

It is assumed that the element concentrations are constant within each voxel, that the neutrons are thermalised and hence that their capture behaviour can be described by a thermal neutron flux Φ_{th} and a thermal neutron cross-section σ_{th} . Equation 4 now simplifies to:

$$A_{ij}(E_\gamma) = \int_{\text{Vol.}}^{\text{voxel}} \Phi_{th}(\vec{r}_i) \sigma_{th} \frac{N_{Av} \vartheta w_i}{M} (1 - e^{-\lambda t_{ir}}) e^{-\lambda t_{d,j}} \frac{1 - e^{-\lambda t_{m,j}}}{\lambda} \gamma(E_\gamma) \varepsilon_j(E_\gamma, \vec{r}_i) d\vec{r}_i, \quad (5)$$

The reconstruction of the element distribution in the sample can be found by solving the vector w_i for all elements, all voxels i and all measurements j from Equation 5, when all other parameters are known.

3.3 Experimental facilities

3.3.1 Design of REDNAILS analysis method

The methods for REDNAILS are based on LS-NAA. Roughly the same procedure is followed. In order to correct for possibly inhomogeneously distributed natural radioactivity, background gamma-ray spectra, $A_j(E_\gamma)$, are acquired for each sample scan position. These spectra are to be subtracted from the spectra acquired in the same positions after sample irradiation, to obtain the spectrum corresponding to net induced radioactivity.

Secondly the gamma-ray attenuation is determined. The method is described in more detail in Paragraph 3.5.2. Then, the sample, surrounded by flux monitors, is irradiated in the BISNIS facility described in Section 3.3.2. The flux monitors are measured with a calibrated gamma-ray detector. Finally, the scanned measurements of the activated sample are performed with the Large Sample Scanned Measurement Facility again.

Figure 1 presents an overview of all steps to be performed for REDNAILS.

3.3.2 Irradiation facility

The samples are activated in the Big Sample Neutron Irradiation System (BISNIS) [6,9], schematically presented in the cross-section in Figure 2. The facility has been designed in such a way that the induced radioactivity of a sample –of

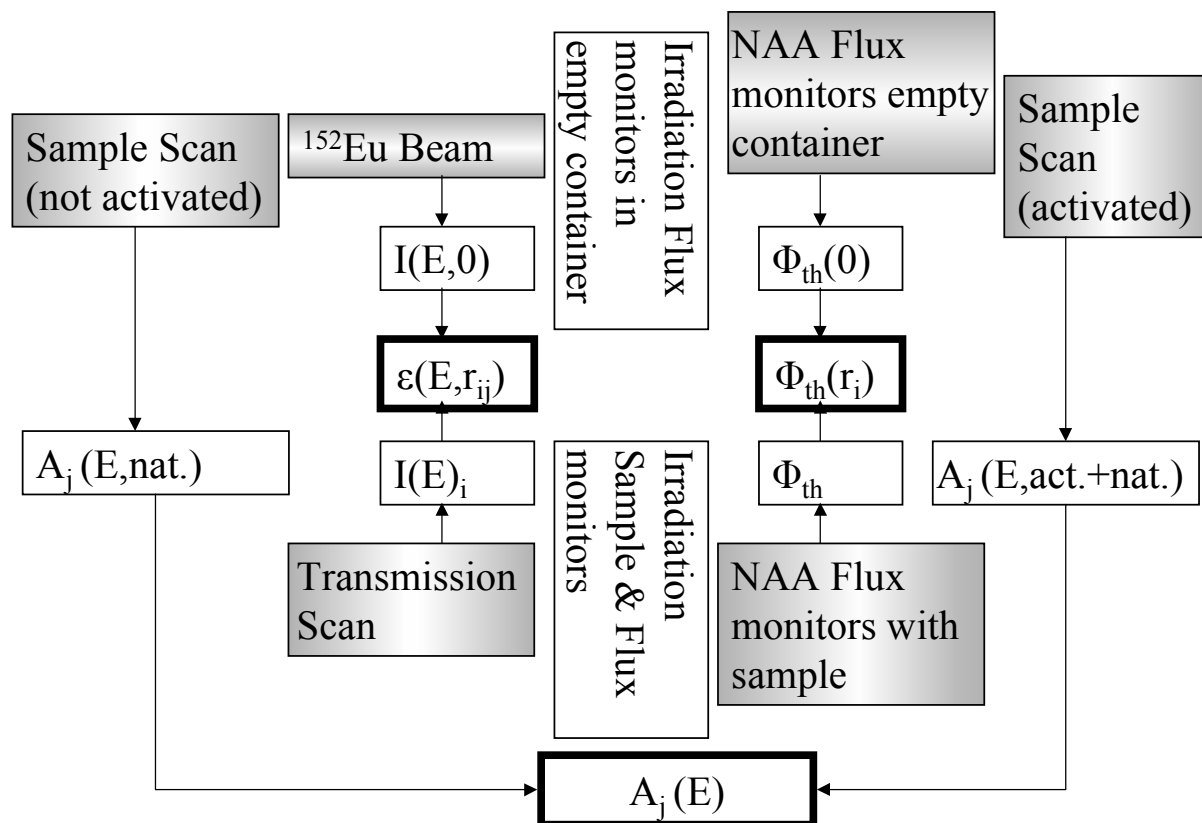


Figure 1. RED NAILS analysis scheme. Sample measurements are indicated by a vertical background fill pattern, calibration measurements indicated by a horizontal pattern, irradiation by vertical text flow, resulting in sample specific parameters for solving Equation 5 in the bold frames.

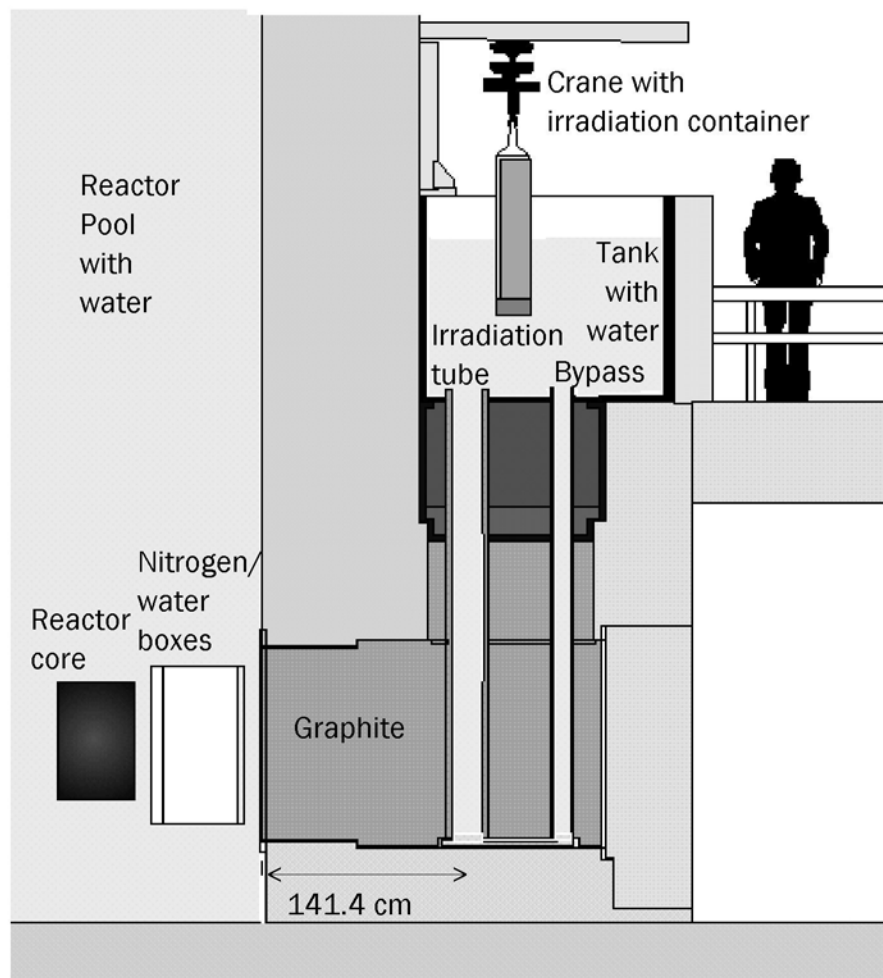


Figure 2 Schematic vertical cross section of the thermal column of the IRI reactor, showing the thermal column's irradiation facility for large samples

which the mass is in the order of 10^4 times that of a 'normal size' INAA sample- is of the same order of magnitude as for such an INAA sample with the same element composition. Also, this facility delivers completely thermalised neutrons at the sample site, minimising thermalisation effects within the sample. To this end, it was installed in the reactor's thermal column, which is fully filled with nuclear-grade graphite blocks, and yields the desired neutron flux and neutron thermalisation.

The facility consists of a tank with two vertical aluminium tubes penetrating into the graphite blocks. It is filled with water to shield the outside from both gamma and neutron radiation. The tank is also used for storage of the activated samples. The two tubes are interconnected at the bottom. The narrower tube

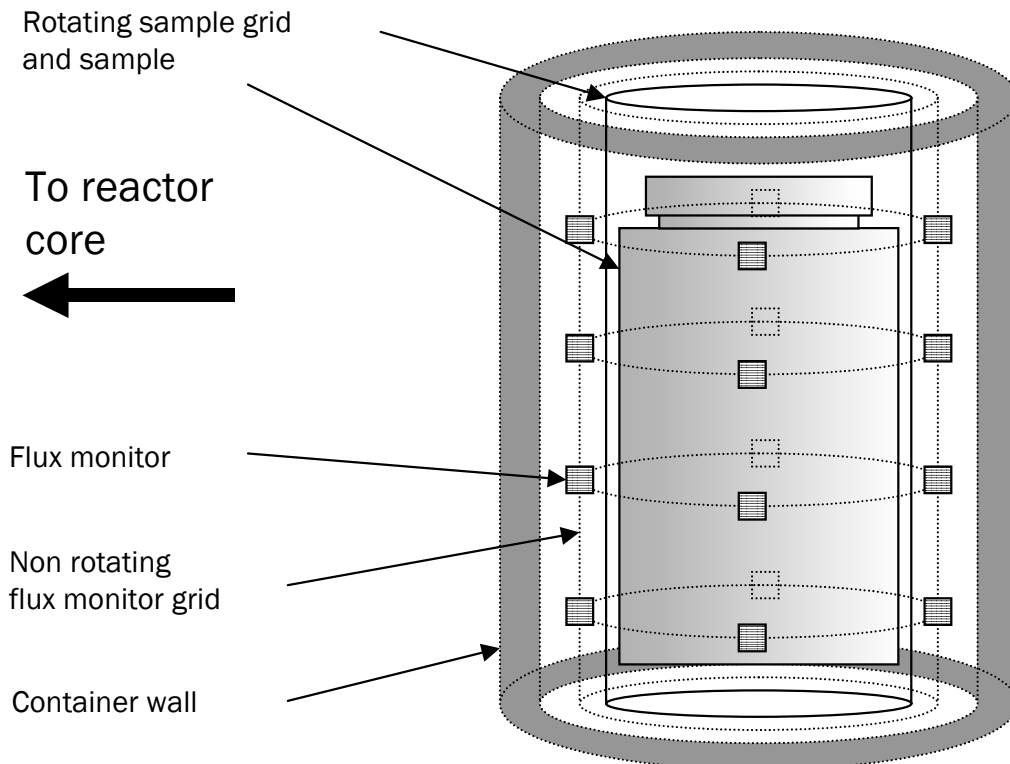


Figure 3 Schematic drawing of a sample (bottle) surrounded by four layers of four flux monitors each, in the irradiation container

serves as a bypass for displaced water when the tightly fitting container is lowered or lifted in the irradiation tube.

In this facility samples up to 1 m length and 15 cm diameter, can be irradiated. The samples are packed, surrounded by neutron flux monitors, in a polyethylene container. The flux monitors stay in a non-rotating grid inside the container. The sample can be rotated around its vertical axis, using a small motor in the screw-on lid of the container. A schematic drawing of the sample in the container is shown in Figure 3.

3.3.3 Scanned Measurement Facility

One facility is used for all scanning measurements of the large samples. It is a slightly modified version of the detector arrangement that is also used for integral LS-NAA [10], as described in Chapter 1. Figure 4 gives an overview of the scanner, while scanning a 1 m long sample. A schematic drawing of the cross section is presented in Figure 5.



Figure 4 The measurement set-up during a scan of a 1 m high sample. indicated are (1) the detector in a lead shielding, (2) the collimator, (3) the sample holder, (4) the sample and (5) the lead castle that contains the transmission source. A schematic drawing of detector, collimator, stepper motor movement options and sample is given in the next figure.

The arrangement consists of four scaffolds. The first is placed arbitrarily, in Figure 4 behind the other arrangements, and contains the pulse generator, preamplifier and computer. The second scaffold bears the detector surrounded by a lead shielding, the lead collimator and the liquid-nitrogen vessel. The third scaffold consists of a sample holder driven by stepper motors under computer control and the fourth scaffold bears a transmission source that can be positioned in front of a pinhole in its lead castle to create a narrow beam.

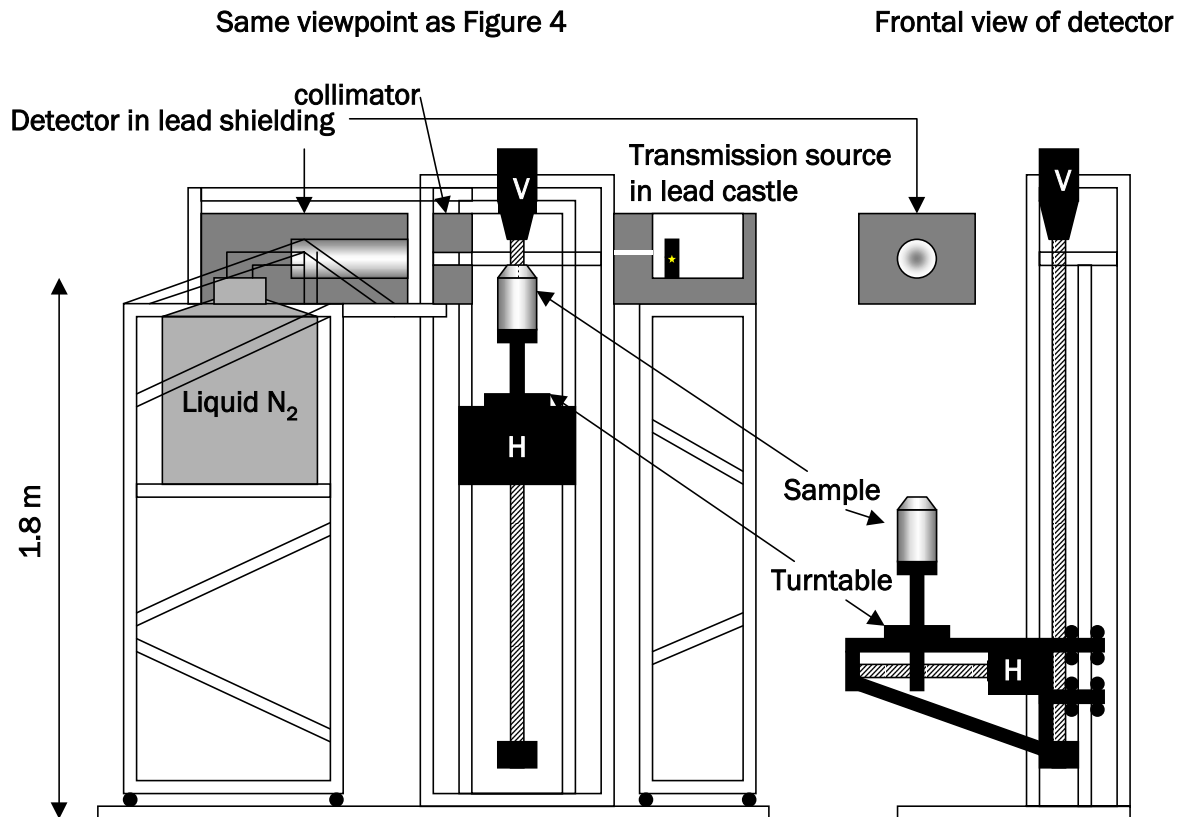


Figure 5 Schematic drawing of the measurement set up. Dark grey are lead elements, black are moving parts, H is the horizontal stepper motor, V is the vertical stepper motor. The right-hand side is tilted 90° in respect to the left-hand side.

The detector is a HPGe cylindrical detector of 97% relative efficiency (relative to the efficiency of a 3"x3" NaI(Tl) scintillation detector), 1.82 keV FWHM resolution at 1333 keV and a peak-to-Compton ratio of 97:1.

For integral LS-NAA the distance from the detector end cap to the vertical central axis of the sample is 20 cm. For scanning samples with a large diameter while using the collimator this distance can be enlarged with 5 cm increments by lateral movement of the scaffold that holds the detector and collimator.

For optimisation of the arrangement for scanned measurements, Monte Carlo simulations of the facility have been performed. This is described in Chapter 5.

3.4 Experimental calibration procedures

By using existing, calibrated facilities for irradiations, few new calibrations had to be performed. Specifically, the capture cross sections to be used for activation calculations were all taken from the k_0 -database[11].

3.4.1 Irradiation

The development and calibration of the methods for determination of the neutron-flux distribution within the sample was part of the development of the normal LS-NAA. By measuring the neutron flux with monitors just outside the sample (see Figure 3) and with reference values in a situation with a calibration sample with well known composition, the neutron flux depression due to the presence of the sample can be determined. From these measurements, the unknown neutron diffusion length L [cm] and neutron diffusion coefficient D [cm] of the sample can be determined. From the flux at a reference point outside the sample, the L and D , the neutron flux distribution inside the sample can be determined, as described in detail elsewhere [6,9].

A reference flux is determined after each change in the reactor core configuration. To this end, the irradiation container with 80 flux monitors is filled with water samples in order to determine the flux at reference positions based on a completely known geometry with materials for which the required neutron parameters are known. The reference fluxes are determined for each flux monitor height in the sample container and can be interpreted as the thermal neutron flux coming into the thermal column at that height on the reactor side.

3.4.2 Scanned measurements

The gamma-ray detection efficiency of the measurement facility without collimator has been calibrated for integral LS-NAA using a set of certified gamma-ray sources. The detection efficiency of these point sources has been determined at 20-cm distance from the detector end cap on the detector's symmetry axis.

For the scanning measurements, a more detailed insight in the detector efficiency and its dependency on source-detector geometry was required. Calibration measurements for a number of different geometries would be too laborious. Therefore an efficiency transfer technique has been applied. A series of

Monte Carlo simulations has been performed to determine the detector efficiency as a function of gamma-ray energy and the dimensions of the path of the gamma ray through the detector. These experiments and their results are described in Chapter 4.

3.5 Experimental sample analysis procedures

3.5.1 Measurement of the natural radioactivity

As indicated in Figure 1, the sample is measured in scanning mode before activation to allow for correction for background radiation from the surrounding materials and from natural radioactivity in the sample. The measurement facility described in Section 3.3.3 is used with the collimator in front of the detector and the transmission source behind the lead shielding.

The sample is mathematically divided in volume elements called voxels. The optimum size and shape of these voxels is determined in Chapter 5. In measurement j the sample is counted with the voxel $i = j$ in front of the detector and collimator opening.

The fitted peak areas resulting from the procedure described in Section 3.6.2 are subtracted from the peak areas obtained from the scanning measurements of the sample after activation, after conversion in case of different acquisition times.

3.5.2 Transmission measurements

Before activation, the sample is scanned once more, now with the transmission source in front of the pinhole, to determine the gamma-ray energy and sample-position dependent transmission of gamma-rays through the sample. This sample property is used to determine the gamma ray and position dependent detection efficiency, $\varepsilon(E_\gamma, r)$ in Equation 5 and Figure 1. Methods and results are described in Chapter 7.

3.5.3 Irradiation

As indicated in Figure 3, during the irradiation the sample is surrounded by flux monitors positioned in a fixed grid in the container.

Before the container is positioned at the bottom of the irradiation tube (see Figure 2), the nitrogen/water boxes are filled with nitrogen gas to increase the neutron flux in the thermal column. Normally, these boxes are filled with water to minimise unnecessary activation of the thermal column.

The irradiation is started by lowering the sample into the irradiation position using the crane. The irradiation is finished by raising the sample to a position in the water tank on top of the thermal column.

After a waiting time for decay of short-lived ($T_{1/2} < 1$ h) radionuclides, the sample and the flux monitors are removed from the container.

For determination of the neutron-flux distribution in the sample, the radioactivity of the flux monitors is measured with one of the calibrated gamma-ray detectors for normal-size samples present in the counting room of the INAA laboratory at the IRI.

3.5.4 Scanned measurements of the activated sample

After a total waiting time of a few hours up to a few days ($t_{d,j}$ in Equation 5), the sample is scanned, using the same procedure as for the natural-activity measurements, to acquire the spectra needed to determine the gamma-ray peak areas after activation $A_j(E_\gamma)$ for all gamma-ray energies E_γ and measurements j .

After a longer decay time (up to a few weeks), the sample can be scanned again, optionally with more counting time per spectrum, to determine more accurately the concentration distribution of elements with long-lived activation products.

3.6 Data analysis and processing

3.6.1 Determination of the sample inhomogeneity

The set of spectra constituting one scan is statistically evaluated to determine whether fluctuations over the scan of the count rates of gamma-rays of

a given energy are only due to Poisson counting statistics or also due to inhomogeneities in the sample.

This method and the results for some of the test experiments are described in Chapter 6.

Based on this knowledge the data can be further analysed. If no inhomogeneities are observed, the sample can be analysed integrally using the weighted sum of all acquired spectra in one scan. If inhomogeneities have only a layered structure in the direction of the cylinder axis of the sample, the sample can be analysed layer by layer, and for the most extreme cases the analysis can be performed for each voxel separately. These various methods are described in Chapter 8.

3.6.2 Spectrum fitting

In order to obtain the peak areas A_{jk} from the raw gamma ray spectra fine-tuned peak fitting procedures are required.

As a basis for the REDNAILS method, the same spectrum fitting procedures [12] are used as in holistic analysis [5]. Firstly, for a peak search, the channel contents are filtered using a second order (mid-window) derivative Routti-Prussin filter, where the window width, energy and peak shape calibrations are derived from a calibration measurement. Next, peak areas are determined by fitting this peak shape and a continuum function to the channel contents with standard non-linear least squares methods. Then, before the final calculations are performed, the fitted spectra are visually inspected and peaks with a $\chi^2 \geq 4$ can be fitted interactively ('manually', by indication of a base-line for the peaks) if relevant.

This procedure is modified for REDNAILS in order to meet its special requirements and to yield extra information for the spectra related to one sample. The first requirement is that areas of peaks found in any measurement spectrum at a given energy, should be determined in the spectra of the other measurements as well.

This is required to stabilise the outcome of the reconstruction. Also the reported peak energy should be the same for all spectra, in order to ensure that a certain peak is consistently attributed to the same radionuclide.

As an extra source of information, the sum of all spectra from one scan can be used to search for peaks that have not been found in the individual spectra,

since the signal-to-noise ratio will be better in the sum spectrum for gamma emitters that are present throughout the large sample. The annihilation peak at 511 keV must be discarded since it will contain useless information due to a large number of pair creation events in the sample, the collimator and other surrounding materials.

In the resulting fitting procedure, first all peak positions (and their related energies) are determined by least squares fitting in all the spectra separately obtained in one sample scan as well as in the sum spectrum. The results are merged into a single list of peak positions. Peaks with positions that are not clearly separated are assigned to the weighted average of these positions. This combined list of peak positions is then used to determine the peak areas in the individual spectra, with the peak positions kept constant in the fitting procedure. It is known from literature that this method stabilises the outcome of the fit. [13,14].

3.6.3 Efficiency factors

After correction for background and natural activity, the peak areas must be related to concentrations of the elements in the voxels. According to the methods of the holistic analysis, Equation 5 is used to calculate the set of expected peak areas K_{ijnl} for each voxel i , spectrum j , element n and peak energy l , assuming that voxel i consists of 100% of element n . In order to do this, the spatial neutron flux distribution $\Phi_{th}(\mathbf{r}_i)$ and the spatial detection efficiency $\varepsilon_j(E_\gamma, \mathbf{r}_i)$ must be known.

The spatial neutron flux distribution, $\Phi_{th}(\mathbf{r}_i)$, is derived from the radioactivity of the flux monitors. As depicted in Figure 3, the sample is surrounded by flux monitors during irradiation. The flux monitors consist of a weighed amount of zinc of about 70 mg. After irradiation, the ^{65}Zn activity is measured with a calibrated gamma ray detector for normal-size samples present in the counting room of the INAA laboratory at the IRI. The standard activation formula, Equation 1, can now be used to determine the flux at the position of the flux monitor. Overwater has determined a method to calculate the spatial flux distribution within the sample based on the changes in the neutron flux at the position of the flux monitors relative to the fluxes observed in the calibration irradiation measurement [9].

The spatial detection efficiency, $\varepsilon_j(E_\gamma, \mathbf{r}_i)$, is determined using the results of the sample-transmission measurements and the spatial detection-efficiency of the

detector in the measurement geometry given, applying the methods described in Chapter 4.

The matrix of the total efficiency factors, K_{ijnl} , is determined for all voxels, measurements and relevant elements, and validated as described in Chapter 9, using Equation 5 and Figure 1.

3.6.4 Reconstruction algorithms

In the holistic approach of INAA and LS-NAA, the vector of observed peak areas \mathbf{A} is related to the vector of element concentrations \mathbf{w} by

$$\mathbf{A} = \mathbf{K}\mathbf{w}, \quad (6)$$

the vector of (average) element concentrations \mathbf{w} can be solved from the observed peak areas A_{ji} using Equation 6, given the matrix of expected peak areas (assuming an element concentration of 100%) \mathbf{K} and the vector of observed peak areas A_{ji} by the linear least squares solution:

$$\mathbf{w} = (\mathbf{K}^t\mathbf{U}\mathbf{K})^{-1}\mathbf{K}^t\mathbf{U}\mathbf{A}, \quad (7)$$

where \mathbf{U} is a diagonal matrix containing the uncertainties in the A_{ji} [5].

For the reconstruction of element distributions in scanned large samples, this method will not suffice: differences between spectra are relatively small compared to Poisson fluctuations. The linear least squares solution will lead to noise enhancement and unstable solutions with alternating, large, positive and negative concentrations.

Two other reconstruction algorithms are implemented and tested in Chapter 8 and 9: the Maximum Likelihood with Expectation Maximisation (MLEM) and the Conjugate Gradient method with a Non-Negativity constraint (CGNN). Chapter 8 focuses on simple model samples. These algorithms are tested with mock samples in Chapter 9.

Finally, in Chapter 10, the REDNAILS method is tested with real samples and validated with normal INAA of subsamples.

3.7 References

1. N.M. Spyrou, J.M. Sharaf, S. Sarkar, Elemental analysis of biological matrices using tomographic techniques, *J. Rad. Nucl. Chem.* 167 (1993) 453-465
2. R.J. Estep, T.H. Prettyman, G.A. Sheppard, Tomographic gamma scanning to assay heterogeneous radioactive waste, *Nucl. Sci. Eng.*, 118 (1994) 145-152
3. R.H.J. Tanke, J.E. Jaspers, P.A.M. Gaalman, D. Killian, Applications of tomography in nuclear-research, *Kernteknik*, 56, 5 (1991) 283-289
4. L. Borms, J. Oeyen, The design of a multipurpose tomography installation, *Nucl. Instr. Meth. A* 422 (1999) 489-492
5. M. Blaauw, The holistic analysis of gamma-ray spectra in instrumental neutron activation analysis, *Nucl. Instr. Meth. A* 353 (1994) 269-271
6. R.M.W. Overwater, The physics of Big Sample Instrumental Neutron Activation Analysis, thesis, Delft 1994
7. H.W. Baas, M. Blaauw, P. Bode, J.J.M. De Goeij, Collimated scanning towards 3D-INAA of inhomogeneous large samples, *Fres. J. Anal. Chem.* 363 (1999) 753-759
8. R.M.W. Overwater, P. Bode, Computer simulations of the effects of inhomogeneities on the accuracy of large sample INAA, *Appl. Radiat. Isot.* 49 (1998) 967-976
9. R.M.W. Overwater, P. Bode, J.J.M. De Goeij, J.E. Hoogenboom, Feasibility of elemental analysis of kilogram-size samples by instrumental neutron activation analysis, *Anal. Chem.* 68 (1996) 341-348
10. P. Bode, R.M.W. Overwater, J.J.M. de Goeij, Large-sample neutron activation analysis: Present status and prospects, *J. Radioanal. Nucl. Chem.* 216 (1997) 5-11
11. M. Blaauw, The k_0 -calibration of the IRI system for INAA of samples in the kg range, *J. Radioanal. Nucl. Chem.* 220 (1997) 233-235
12. M. Blaauw, Statistical properties of a peak-search algorithm for γ -ray spectrometry as related to Currie's detection limits, *Nucl. Instr. Meth. A* 336 (1993) 273-277
13. L.H. Christensen, K. Heydron, *J. Radioanal. Nucl. Chem.* 113 (1987) 19.
14. M. Blaauw, Multiplet deconvolution as a source of unstable results in gamma-ray spectrometry for INAA, *Nucl. Instr. Meth. A* 333 (1993) 548-552

Chapter 4

3D-modelling of the Ge detector full-energy peak efficiency for measurements of the spatial radioactivity distributions

4.1 Introduction

As mentioned in the previous chapter, for the reconstruction of element distributions in large neutron-activated inhomogeneous samples, the spatial distribution of gamma-ray emitters within the sample has to be determined. The use of a collimated Ge-detector for scanning of the sample in the measurement of the gamma-ray spectrum was introduced in Chapter 3. The optimisation of the measurement set-up will be described in Chapter 5. For the reconstruction of element distributions based on these spectra, the spatial detection efficiency must be determined.

Usually, in a system for measurement of the radioactivity distribution in samples –e.g. emission tomography in nuclear medicine- the gamma-ray energy and the total radioactivity have been optimised in respect to attenuation in the sample and collimated detection.

For determination of spatial activity distributions in LS-NAA, an optimisation of the experimental arrangement as mentioned above is not applicable, because the sample composition is not a parameter that can be optimised. This means that for NAA, radionuclide activities depend on the sample composition as well as on irradiation and decay time, and are not known in advance. Besides, the gamma-ray energies to be measured depend on sample composition and range largely

from 100 keV to 3 MeV, which is difficult to collimate. Therefore, a collimator for these measurements will be transparent to a certain extent for high-energy gamma-rays from all directions. Finally, the sample activity is relatively low, which asks for collimation with a large opening. Hence the detection efficiency of the detector has to be determined for all gamma-rays within this energy range and coming from all directions.

For such a system a method was needed for determining the three-dimensional gamma-ray detection efficiency. The method has been developed for the detector used in the Large-Sample Scanning system and has been applied to a second detector to get more insight in the general applicability of the method.

In scanning measurements in Large-Sample Neutron Activation Analysis, the energy dependence of the spatial detection efficiency cannot be described by a single curve for a point source [1], possibly corrected for solid angle [2,3], since the collimator introduces a dependency of the effective solid angle on the gamma-ray energy. Hosseini-Ashrafi and Spyrou [4] studied the effect of collimator penetration for gamma-ray energies above a few hundred keV. They determined an effective solid angle, assuming the detection efficiency to be independent of both point of entry on the crystal surface and angle of incidence. However, this assumption is only a rough approach and may give rise to errors, for instance for gamma-rays entering the detector near an edge of the crystal.

More recently the method of Moens [2] has been improved by calculating the full-energy peak efficiency by Monte-Carlo simulations [5]. This approach to calculate the effects in the crystal was also applied by Overwater [6], but is relatively time consuming, usually 2-20 s per gamma-ray energy and per voxel, using a 266 MHz Pentium® PC, for a precision of 1%.

In order to find a mathematical description of the detection efficiency, Gehrcke [7] measured and described analytically point kernels for the detection efficiency, that can be integrated numerically over a large sample. His detector and collimator system was cylindrically symmetrical. Although computations based on this approximation are much faster than Monte-Carlo calculations, it cannot be applied to asymmetrical, slit-shaped collimators. Moreover, it requires calibration measurements for each new collimator opening setting.

The method described in this chapter goes a step further. The method is based on considering the full-energy peak detection efficiency as a function of the

position and direction of incidence of the gamma-ray relative to the front end of the detector. Our assumption is that, once we know this full-energy peak efficiency function, we are able to calculate the full-energy peak efficiency for any position in space after calculation of the attenuation of the gamma rays in intermediate media and the geometrical efficiency.

First, in Monte Carlo simulations, pencil beams of photons are generated that hit the bare detector crystal at a given position and under a given angle. Next, the path and interactions of these photons inside the crystal are followed. The detection of gamma rays in the full-energy peak is analysed separately for each type of interaction within the crystal, which renders a first-order approximation of the detection efficiency as a function of gamma-ray energy, direction and point of incidence. Next, the detection efficiency for a point source is determined by integration of these detection efficiencies for single narrow beams over the entire crystal front surface, taking into account the attenuation of all materials in between source and surface of the active core of the detector crystal. Finally, the detection efficiency can be integrated over the source volume resulting in the detection efficiency for a large sample, or any part of it.

Since the detector is cylindrically shielded by at least 10 cm of lead and gamma rays that may impinge on the detector side originate from the sample somewhere behind the collimator and at a larger distance from the detector, it is assumed that the detection efficiency of these gamma rays may be neglected.

4.2 Theory

A photon, emitted from a radionuclide positioned inside a sample, has a certain probability of reaching the detector unperturbed and depositing its energy completely within the detector crystal, hence of contributing to the full-energy peak in the spectrum registered. This probability depends on: (i) the probability of having a direction within the solid angle, with a trajectory of the photon crossing the detector, (ii) the probability of the photon not being scattered or absorbed in the intermediate media (the materials between source and active crystal surface) and (iii) the probabilities of the different interaction types in the detector crystal.

The detection efficiency calculation is based on point kernel integration, in which sample and detection system are separated, as well as detector and

collimator. The path-dependent detection efficiency $\varepsilon_{tot}(E_\gamma, \vec{r}, \vartheta, \varphi)$, integrated over all directions, leads to the point kernel:

$$\begin{aligned} \varepsilon_{tot}(\vec{r}, E_\gamma) &= \frac{1}{4\pi} \int_{\varphi=0}^{\pi} \int_{\vartheta=0}^{2\pi} \cos \vartheta d\vartheta d\varphi \varepsilon_{tot}(E_\gamma, \vec{r}, \varphi, \vartheta) \\ &= \frac{1}{4\pi} \int_{\varphi=0}^{\pi} \int_{\vartheta=0}^{2\pi} \cos \vartheta d\vartheta d\varphi \varepsilon_{sample}(E_\gamma, \vec{r}, \varphi, \vartheta) \varepsilon_{coll}(E_\gamma, \vec{r}, \varphi, \vartheta) \varepsilon_{det}(E_\gamma, \vec{r}, \varphi, \vartheta) \end{aligned} \quad (1)$$

where ε_{tot} is the total energy dependent detection efficiency for a source at position \vec{r} , ε_{sample} indicates the sample detection efficiency, ε_{coll} the contribution of the collimator to the detection efficiency and ε_{det} internal detector detection efficiency, E_γ is the energy of the photon, φ and ϑ describe the direction of the photon and hence determine the angle of incidence on the detector front area. The detection efficiency $\varepsilon_{tot}(E_\gamma, \vec{r}, \vartheta, \varphi)$ is integrated over φ and ϑ for each position to obtain the point kernel, and then integrated over the voxel or sample volume to get the voxel or sample detection efficiency.

If the detection efficiency is represented as the integration of $\varepsilon_{tot}(E_\gamma, \vec{r}, \vartheta, \varphi)$ over a unit sphere:

$$\varepsilon_{tot}(\vec{r}, E_\gamma) = \frac{1}{4\pi} \iint_{4\pi} \varepsilon_{tot}(E_\gamma, \vec{r}, \varphi, \vartheta) d\varphi \cos \vartheta d\vartheta, \quad (2)$$

the probability of the photon trajectory impinging on the detector is calculated from the integral over the solid angle of the detector as seen from the point of view of the point source:

$$\varepsilon_{tot}(\vec{r}, E_\gamma) = \frac{1}{4\pi} \iint_{\substack{\vartheta, \varphi \text{ crossing} \\ \text{detector}}} \varepsilon_{tot}(E_\gamma, \vec{r}, \varphi, \vartheta) d\varphi \cos \vartheta d\vartheta. \quad (3)$$

The probability of the photon reaching the detector crystal unperturbed is implemented in this function, resulting in:

$$\varepsilon_{tot}(\vec{r}, E_\gamma) = \frac{1}{4\pi} \iint_{\substack{\vartheta, \varphi \text{ crossing} \\ \text{detector}}} e^{-\sum_i \mu_i(E_\gamma) d_i(\vec{r}, \varphi, \vartheta)} \varepsilon_{det}(E_\gamma, \vec{r}, \varphi, \vartheta) d\varphi \cos \vartheta d\vartheta, \quad (4)$$

where μ_i is the total attenuation coefficient of intermediate material i and d_i the pathlength in material i .

The calculation of the detection efficiency of the crystal is now described from the point of view of the crystal: for a photon being detected with energy E_γ impinging on the detector from position \vec{r} in the sample and in the direction (φ, ϑ) . Because of the cylindrical symmetry of the crystal, each incident photon can be described as a rotated version of a photon entering the crystal at a point on the bold line in Figure 3.

The contributions to the probability of the photon being eventually detected full-energy peak in the crystal, are described for the three different interaction types in the next paragraphs.

4.2.1 Photoelectric effect

If it is assumed that photoelectric interaction occurs as the first interaction

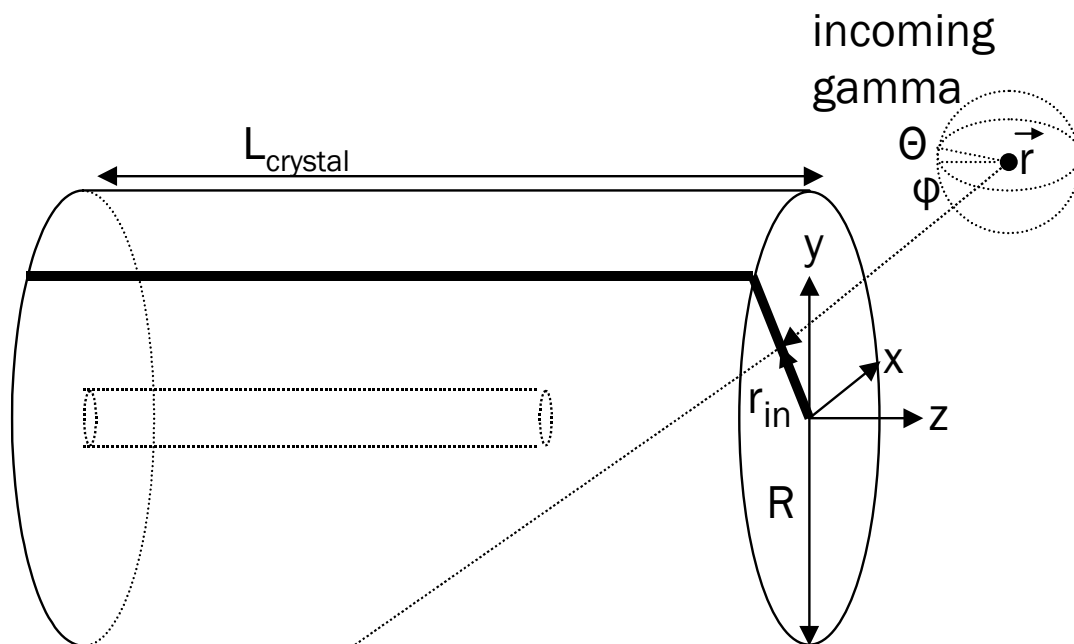


Figure 1 Schematic drawing of the coaxial detector crystal, with an inactive core, used in the simulations and modelling of the detector efficiency. Since the detector has a cylindrical symmetry, all incident gammas can be considered to enter the crystal at a point on the bold line

in the active core of the detector, then the contribution to the detection efficiency of full-energy peak is

$$\varepsilon_{photo}(E_{\gamma}, \Delta x) = \int_0^{\Delta x} d\varepsilon_{photo}(\bar{x})dx = \mu_{photo}(E_{\gamma}) \int_0^{\Delta x} C_{photo}(E_{\gamma}, \bar{x})dx, \quad (5)$$

where Δx [m] is the path length of the photon trajectory through the crystal, μ_{photo} [m^{-1}] is the linear attenuation coefficient due to the photoelectric effect for photons of energy E_{γ} , \bar{x} is path through the crystal and C_{photo} is the correction factor for the probability of a photoelectric interaction: the gamma is absorbed by an atomic electron with the subsequent ejection of the electron from the atom followed by X-rays due to electrons filling subsequent vacancies. resulting in detection of the full energy of the photon. C_{photo} will be close to unity for most gamma energies, because the detector material has much higher stopping power for the X-rays and electrons emitted in the photoelectric process than for the original gamma-ray. Still, some X-rays may escape. Therefore C_{photo} will differ from unity, especially for low E_{γ} which is associated with a large μ_{photo} and as a result for gamma rays interacting with the crystal close to the surface of the crystal front-end.

4.2.2 Compton scattering

One or more Compton interactions may occur, followed by a photoelectric interaction then the contribution to the detection efficiency of full-energy peak is:

$$\varepsilon_{Compton}(E_{\gamma}, \Delta x) = \int_0^{\Delta x} d\varepsilon_{Compton}(\bar{x})dx = \mu_c(E_{\gamma}) \int_0^{\Delta x} C_{Compton}(E_{\gamma}, \bar{x})dx, \quad (6)$$

where $C_{Compton}$ is the correction factor determined by the probability that the Compton-scattered photon will deposit all its energy in the crystal. The geometrical dependency of $C_{Compton}$ is as yet unknown.

An energy-dependent fraction of the gamma-rays, will be scattered in the backwards direction near the point of entry:

$$P_{bs+esc} = \int_0^{\Delta x} \mu_{bs}(E_\gamma) e^{-(\mu_{tot}(E_\gamma) + \mu'_{tot}(E'_\gamma))x} dx = \mu_{bs}(E_\gamma) \frac{1 - e^{-(\mu_{tot}(E_\gamma) + \mu'_{tot}(E'_\gamma))\Delta x}}{\mu_{tot}(E_\gamma) + \mu'_{tot}(E'_\gamma)}, \quad (7)$$

where P_{bs+esc} is the probability that the backward-scattered gamma escapes from the crystal, μ_{bs} [m⁻¹] is the probability for a backward scatter event, μ_{tot} [m⁻¹] is the total attenuation coefficient of the original gamma and μ'_{tot} [m⁻¹] is the total attenuation coefficient of the backward scattered gamma with energy:

$$E'_\gamma = \frac{E_\gamma}{1 + \frac{2E_\gamma}{m_0 c^2}},$$

with m_0 the rest mass of the electron and c the velocity of light in vacuum. This effect reduces the fraction of gammas that can be fully detected. For a detector with a large size relative to the free path length for that gamma energy ($3/\mu = L_{crystal}$), Equation 7 leads to:

$$P_{bs+esc} = \frac{\mu_{bs}(E_\gamma)}{\mu_{tot}(E_\gamma) + \mu'_{tot}(E'_\gamma)}. \quad (8)$$

Hence for those gamma energies, P_{bs+esc} is even independent of the “depth” of the detector. The value of μ_{bs} depends on the energy and the solid angle, as described by the Klein-Nishina formula.

Contributions due to scattering in other directions cannot be described easily in general and will depend on the detector dimensions. In general, the correction factor will depend on the position (x,y,z) of intersection of the gamma trajectory with the detector front end, on the direction (φ,θ) or (u,v,w) of the gamma, on the path through the crystal, and on the dimensions of the crystal.

4.2.3 Pair creation

For $E_\gamma > 1022$ keV, pair creation may occur followed by (i) complete absorption of the energy of the electron and positron, (ii) annihilation of the positron and (iii) complete photoelectric absorption of the two 511 keV gammas then the contribution to the detection efficiency of full-energy peak is:

$$\varepsilon_{pair}(E_\gamma, \Delta x) = \int_0^{\Delta x} d\varepsilon_{pair}(\bar{x}, \Delta x) = \mu_p(E_\gamma) \int_0^{\Delta x} C_{pair}(E_\gamma, \bar{x}) dx, \quad (9)$$

where C_{pair} is the probability that the energy is completely deposited in the crystal. Due to the high penetration power of photons with $E_\gamma > 1022$ keV and the fixed energy of the reaction products with the lowest attenuation, i.e. the 511 keV annihilation gamma's, it is assumed that C_{pair} varies only little with E_γ . This may change for $E_\gamma > 2$ MeV, where Bremsstrahlung photons from the electron and positron are the reaction products with the lowest attenuation.

Because of the similarity in the eventual reaction products (i.e. gammas) of pair creation and of Compton scattering, the correction factor C_{pair} will be another function of the same parameters as $C_{Compton}$.

4.2.4 Combination of the interaction processes

Now, with the linear narrow-beam full-energy peak absorption coefficient defined as

$$\mu_d(E_\gamma, \vec{x}) = \mu_{photo}(E_\gamma)C_{photo}(E_\gamma, \vec{x}) + \mu_{Compton}(E_\gamma)C_{Compton}(E_\gamma, \vec{x}) + \mu_{pair}(E_\gamma)C_{pair}(E_\gamma, \vec{x}), \quad (10)$$

and after integrating μ_d over Δx , the 3-dimensional photo-peak detection efficiency can be written as:

$$\varepsilon_{det}(\vec{r}, E_\gamma) = (1 - e^{-\mu_{tot}(E_\gamma)\Delta x})^0 \frac{\int_0^{\Delta x} \mu_d(E_\gamma, \vec{x})}{\mu_{tot}(E_\gamma)}, \quad (11)$$

and hence:

$$\varepsilon(\vec{r}, E_\gamma) = \frac{1}{4\pi} \iint_{\substack{\vartheta, \varphi \text{ crossing} \\ \text{detector}}} e^{-\sum_i \mu_i(E_\gamma) d_i(\vec{r}, \varphi, \vartheta)} (1 - e^{-\mu_{tot}(E_\gamma)\Delta x})^0 \frac{\int_0^{\Delta x} \mu_d(E_\gamma, \vec{x})}{\mu_{tot}(E_\gamma)} d\varphi \cos\vartheta d\vartheta. \quad (12)$$

Moens [2] gives a comparable equation for calculation of the effective solid angle, assuming $C_{photo} = 1$ and in his equation μ_d depends on gamma energy only.

Results for detection efficiency calculations with Monte-Carlo modelling are reported to deviate up to 12% [8] from measurement, probably due to imperfect charge collection in the real crystal [9], an effect that is difficult to predict and

differs from crystal to crystal. Therefore, the accuracy of the model is improved by calibration of the system under investigation. The efficiency in a reference geometry can be measured and modelled. Now systematic deviations of the detection efficiency of the model $\varepsilon_{\text{model}}$, are eliminated by renormalization to the measured detection efficiency $\varepsilon_{\text{meas}}$ of point sources at position \vec{r}_0 :

$$\varepsilon_{\text{meas}}(\vec{r}) = \frac{\varepsilon_{\text{model}}(\vec{r})}{\varepsilon_{\text{model}}(\vec{r}_0)} \varepsilon_{\text{meas}}(\vec{r}_0). \quad (13)$$

After applying the above calibration, the model is ready to be used for calculations of the detection efficiencies for scanned measurements of large inhomogeneous samples, by summation of the point source efficiencies over the sample volume or any part of it (see the end of next Section).

4.3 Experimental set-up and methods

The gamma-ray detection efficiency is determined for two coaxial Ge detectors, of 17% and 97% relative efficiency. The relative efficiency is defined at 1332 keV for a point source on the axis of the detector at 25cm from the detector end cap face, relative to the efficiency for a hypothetical 3"x3" NaI detector for the same energy and geometry. The 97% HPGe detector, used for scanning measurements, is surrounded by a lead shielding (for a side view, see Figure 4). The 17 % detector is an unshielded Ge(Li) detector. The EGS4 [10] software was used for the Monte Carlo simulations.

Since either the shielded HPGe detector in scanning experiments or the unshielded Ge(Li) detector in experiments with a source directly in front of the detector is applied, only photons that impinge on the detector front end are considered, hence photons impinging on the side wall are disregarded.

First, Monte Carlo simulations were applied to determine the interaction and detection probabilities within the detector crystal - C_{photo} , C_{Compton} and C_{pair} - for gamma-ray energies between 70 keV and 3 MeV.

Input values for these simulations are energy, position and direction of the photons. Each photon reaches the front end of the crystal at a certain position and with a certain direction. Simulations are performed for five positions, varying from the centre towards the outside of the front of the detector

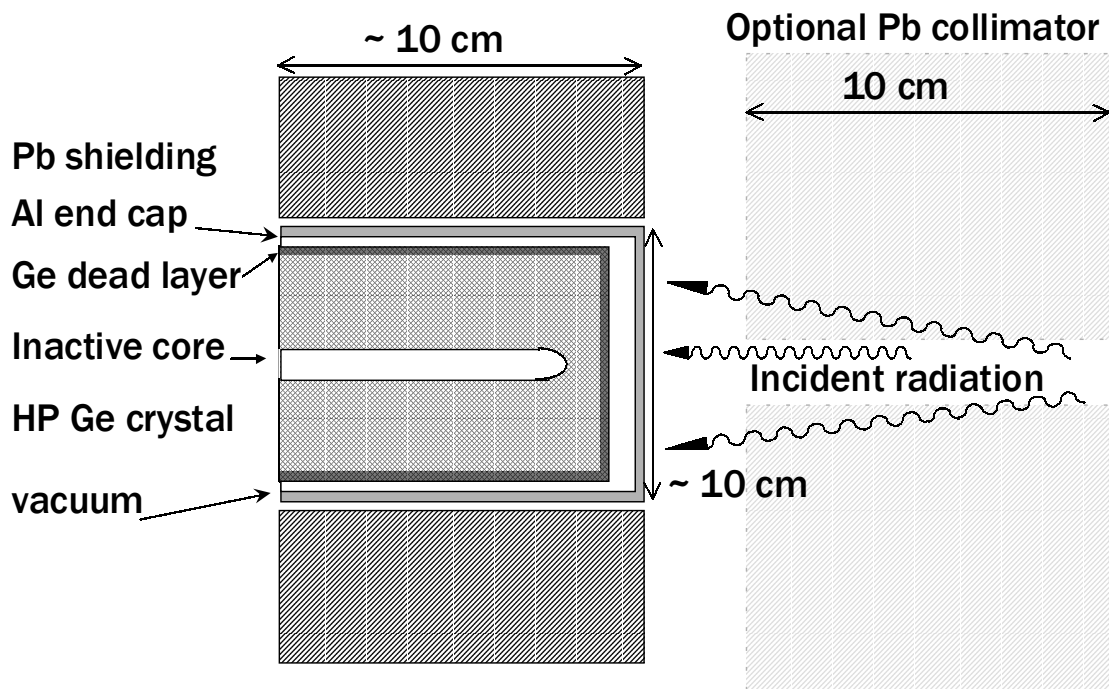


Figure 2 Crosssection of the modelled “97%” detection system. The collimator is applied for sample scanning.

(0,0.2R,0.4R,0.6R,0.8R), with R [m] the radius of the crystal (see Figure 1), and for $5 \times 3 \times 3$ different directions, all towards the detector crystal. The normalised direction vector (u_{in}, v_{in}, w_{in}) with $(0,0,-1)$ perpendicular into the crystal front end and $(1,0,0)$ pointing along the crystal x-axis (See Figure 1) with the five points of incidence. Before normalisation, u_{in} was taken from the set $\{-1, -1/2, 0, 1/2, 1\}$, v_{in} from $\{-1, -1/2, 0\}$ and w_{in} from $\{-1, -2/3, -1/3\}$.

When a photon travels along a path through the detector crystal, the three possibilities of full-energy absorption are distinguished: full photoelectric absorption, Compton scattering followed by photoelectric absorption of the Compton-scattered gamma, and photoelectric absorption of the annihilation gammas after a pair production event, where the first interaction in a photon history classifies the photon history. These three contributions to the full-energy peak area are counted separately during the simulation of a photon passing the end cap with certain energy at a certain place with a certain direction. The Monte Carlo calculations are repeated until an imprecision of 1 % is assuming a normal distribution, *i.e.* until 10^4 photons are fully detected. With the data described, the

correction factors can be fitted as polynomial functions of photon energy, the point of impact, the direction of the incoming photon and parameters that follow from that position and direction for the crystal and crystal dimensions. The fit was carried out using the squared statistical parameter:

$$F_{kl}^2 = \frac{1}{C_{kl,MC}} \left(\frac{C_{kl,MC} - C_{kl,fit}}{\sigma(C_{kl,MC})} \right)^2 \quad (14)$$

where l covers the N_{dir} (=45) directions, the subscript k covers the N_r (=5) radial positions, $C_{kl,MC}$ is the correction factor derived from the Monte Carlo simulation, $C_{kl,fit}$ is the fitted correction factor and $\sigma(C_{kl,MC})$ is the standard deviation of $C_{kl,MC}$:

$$\sigma(C_{kl,MC}) = \sqrt{C_{kl,MC} / J_{kl}},$$

with J_{kl} the number of (either photo-effect, Compton or pair production) interactions in the Monte Carlo session.

Each F was weighted with the solid angle of the fraction of the detector end cap represented by that position:

$$\sum_r F_{r,weighted}^2 = \sum_r \frac{\sum_{k=1}^{N_r} \sum_{l=1}^{N_{dir}} F_{kl}^2 ((r_{k+1} + r_k)^2 - (r_{k-1} + r_k)^2) w_l}{\sum_{k=1}^{N_r} \sum_{l=1}^{N_{dir}} ((r_{k+1} + r_k)^2 - (r_{k-1} + r_k)^2) w_l}, \quad (15)$$

where r is the radial position of the point of impact and w is the perpendicular component of the direction relative to the detector. And for the fit, Equation 15 was minimised.

Because high-energy photons are expected to give the most complex correction factors, the polynomial was first fitted for 3 MeV gammas.

For the determination of the detection efficiency for a point source via the fitted model, the minimised Equation 15 was applied, also taking into account the estimated dead-layer thickness and the thickness of the end cap of the detector. Instead of the integral, a summation was used for $N_{det} = 100$ equally sized positions on the crystal front end:

$$\varepsilon(\vec{r}, E_\gamma) = \frac{A_{\text{det}}}{4\pi N_{\text{det}}} \sum_{j=1}^{N_{\text{det}}} \frac{w_j}{r_j^2} e^{-\sum_i \mu_i(E_\gamma) d_i(\vec{r}, \varphi, \vartheta)} (1 - e^{-\mu_{\text{tot}}(E_\gamma) \Delta x(\vec{r}_j)}) \frac{\mu_d(E_\gamma, \vec{r}_j)}{\mu_{\text{tot}}(E_\gamma)}, \quad (16)$$

where A_{det} is the crystal surface area, \vec{r}_j is the vector connecting the point source and the detector position j , and w_j is the perpendicular fraction of \vec{r}_j on the crystal surface.

The model was verified for the two detectors with non-collimated measurements of calibrated point sources (gamma-ray energies ranging from 122 to 1836 keV) on the detector symmetry axis at 20 cm (for the 97% detector) and 25 cm (for the 17% detector) of the detector end cap, applying Equation 15 and Equation 16. These large distances were employed to avoid coincidence-summing effects.

Finally, the model was verified for scanning measurements, for the 97% detector. The detector was collimated with a 10 cm thick lead collimator with a slit-shaped opening of 2 cm (see Figure 2), covering the sample in height and width. A calibrated ^{152}Eu point source was vertically translated, at 25 cm horizontally from the end cap, with intervals of 2 cm. Also, the detection efficiency was calculated for each position of the source, relative to the collimator and detector. Only the photons with the highest energy emitted by the source, 1408 keV, were considered, because they have the highest penetration power and thus will show the collimator leakage the most.

4.4 Results

For the 97% detector, the results for the fitted correction factors are given in the next paragraphs and the Figures 3-7.

4.4.1 C_{photo}

The empirical function $C_{\text{photo,fit}}(E_\gamma, r_{\text{in}}) = a_1(E_\gamma) + a_2(E_\gamma) \ln((R - r_{\text{in}})/r_0)$, where r_{in} [m] is the radial position where the photon hits the crystal front end and $r_0 = 0.01$ m, is a relatively simple function that fitted best for all simulations and gamma energies, where R is the radius in cm of the active crystal. First, the parameters a_1 and a_2 were fitted to the data points at each energy E_γ . Next, the

dependencies of a_1 and a_2 on photon energy were modelled and the parameters of the models determined by fitting. The results are plotted in Figure 3. It can be seen that $C_{photo,fit}$ depends more on r_{in} with increasing E_γ , because of leakage of high-energy Bremsstrahlung caused by the high energy of the electron ejected by the photoelectric interaction. The quantities a_1 and a_2 were modelled with: the functions $a_1 = 1 - 0.06 * (E_\gamma/1 \text{ MeV})^{1.52}$ and $a_2 = \max(0, 0.0344 * (E_\gamma/1 \text{ MeV}) - 0.01)$. These fitted curves are also plotted in the figure.

Due to singularity at $\ln(0)$, this approximation function cannot be used for calculations of the efficiency at r_{in} being close to R ; but r_{in} was not larger than $0.8R$ in this study. Furthermore, in this study of $C_{photo,fit}$, the angle of incidence did not change the $C_{photo,fit}$ significantly. Hence this fitted function is independent of this angle.

4.4.2 $C_{Compton}$

First the parameter dependencies at 3 MeV were analysed, because for this energy the contribution of Compton interactions was expected to be the most difficult. The $C_{Compton}$ dependencies on (i) path length Δx , (ii) forward direction component $-W_{in}$, (iii) average radius of the path in the crystal (distance of the original photon path to the crystal symmetry axis) r_{av} , (iv) position of incidence r_{in} and (v) the average depth of the path in the crystal (average distance of the

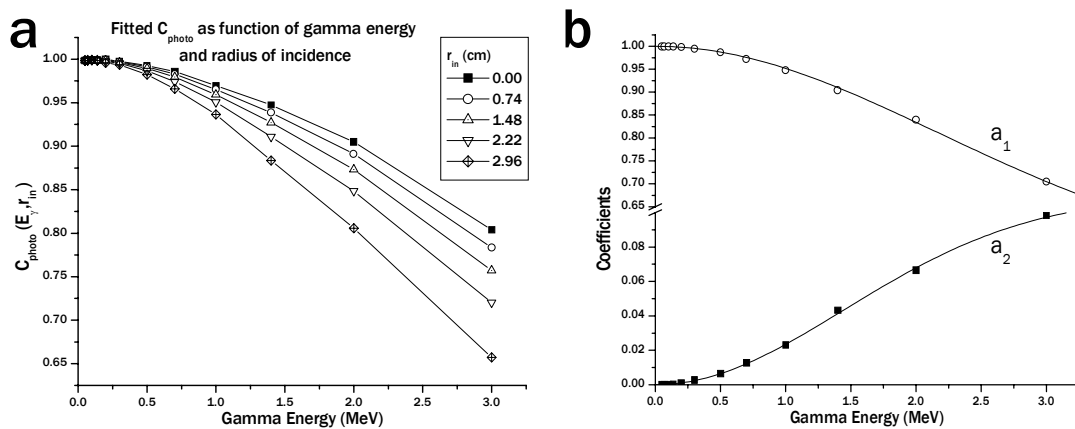


Figure 3 Results for: (a) fitted values for C_{photo} as function of E_γ and r_{in} and (b) parameters in the equation for $C_{photo,fit}$. For higher E_γ , $C_{photo,fit}$ depends only more on r_{in} , demonstrated by the increase of A_2 with increasing E_γ .

original photon path to the crystal front end) $-z_{av}$ are plotted together with (vi) the $C_{Compton}$ fit in Figure 4, where r_{out} is the radius of the position where the original photon path leaves the crystal. In Figure 4a,d,e the marked outliers are due to the narrow inactive core of the crystal: the path is relatively short for forward scattering (Figure 4d), but slightly scattered gamma's have a large probability to be detected (Figure 4a,e).

The following empirical function was fitted on the 225 situations:

$$C_{Compton,fit} = a_0 + a_1 w_{in} + a_2 w_{in}^2 + \ln\left(\frac{R-r_{in}}{R}\right)(a_3 + a_4 w_{in} + \frac{a_5}{R-r_{in}}) + a_6 \Delta x + \frac{a_7}{\Delta x} + a_8 \left(\frac{1}{a_9} + \Delta x\right) e^{-a_9 \Delta x} + a_{10} (x_{in} u_{in} + y_{in} v_{in}) + a_{11} z_{av} + a_{12} z_{av}^2 + a_{13} (1 - e^{-(R-r_{av})A_{14}}) + a_{15} r_{out} \quad (17)$$

The fitted function is a polynomial composition based on educated guesses after theory in 4.2.2, trends observed in Figures 4a-e and trial and error. The quality of fit was for 3 MeV photons: $F_{r,weighted}^2 = 4.7$.

The parameters a_0 through a_{15} in the $C_{Compton}$ function depend on E_γ . These dependencies were modelled by fitting these parameters for each E_γ separately and finally fitting polynomials to the observed E_γ -dependencies of each parameter separately.

4.4.3 C_{pair}

The C_{pair} dependencies on (a) path length, (b) forward direction component $|w_{in}|$, (c) r_{av} , (d) position of incidence r_{in} and (e) $|z_{av}|$ together with (f) its fit results are plotted for 3 MeV in Figure 5. It can be seen that the correction factor for detection after pair creation depends on the parameters also used for $C_{Compton}$, though in a different manner.

The following empirical function was fitted:

$$C_{pair,fit} = a_0 + a_1 W_{in}^2 + a_2 (R^2 - r_{in}^2) + a_3 (R - r_{in})(X_{in} U_{in} + Y_{in} V_{in}) + a_4 \ln\left(\frac{R-r_{in}}{r_0}\right) + a_5 (R - r_{av}) + a_6 (1 - e^{-b_8 (R+r_{av})}) + a_9 Z_{av} + a_{10} Z_{av}^2 + a_{11} \Delta x + a_{12} \Delta x^2 \quad (18)$$

Quality of fit: $F_{r,weighted}^2 = 7.0$

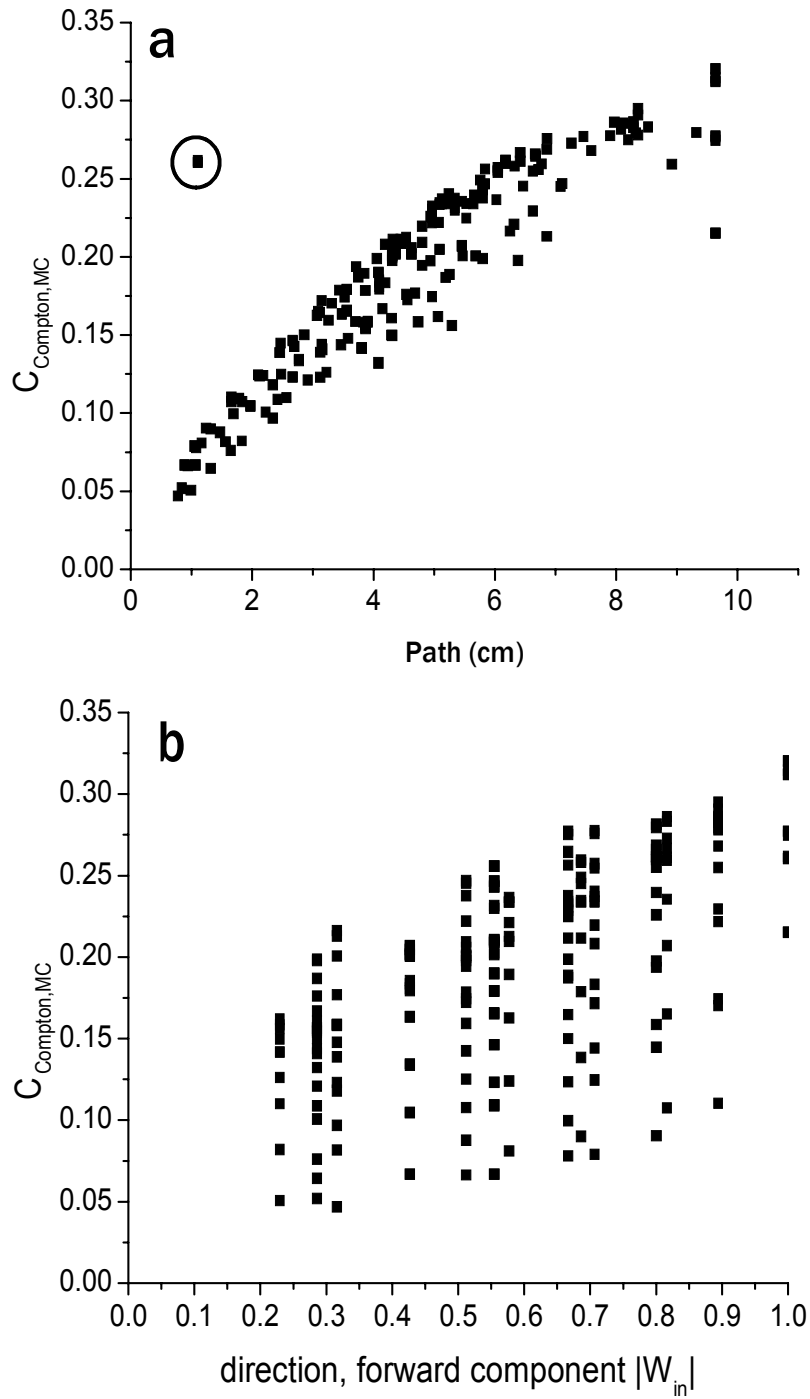


Figure 4a,b. C_{Compton} dependencies and fit for simulation of 3 MeV gammas. In 4a the values found for are plotted as function of path length, in 4b as function of the forward component of the direction vector. In 4a the marked outliers, large C_{Compton} considering the path length, belong to gammas that reach the inactive core, but the secondary gammas probably not.

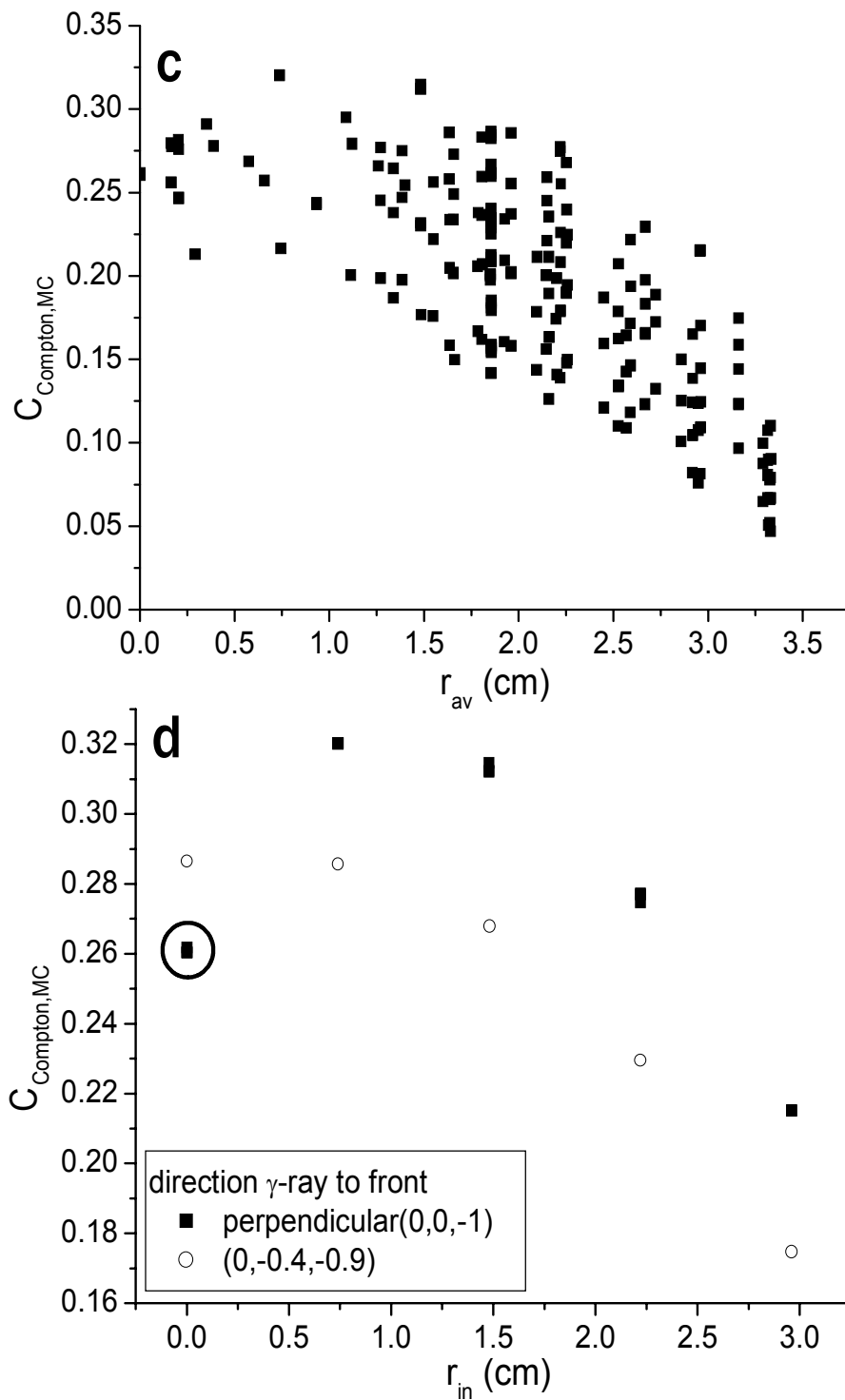


Figure 4c,d. C_{Compton} dependency on r_{av} , r_{in} and angle of incidence. Marked outliers in 4c are the same as in 4a, but exceed now in the other direction, because in 4c the other perpendicular points have the same path length, and only the outliers have this much shorter path length.

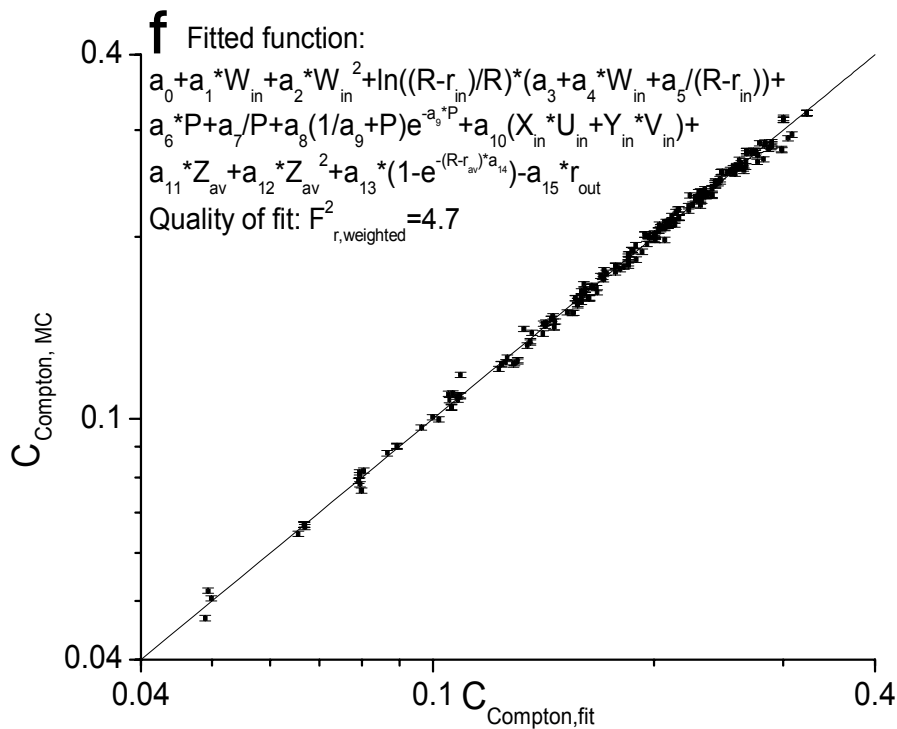
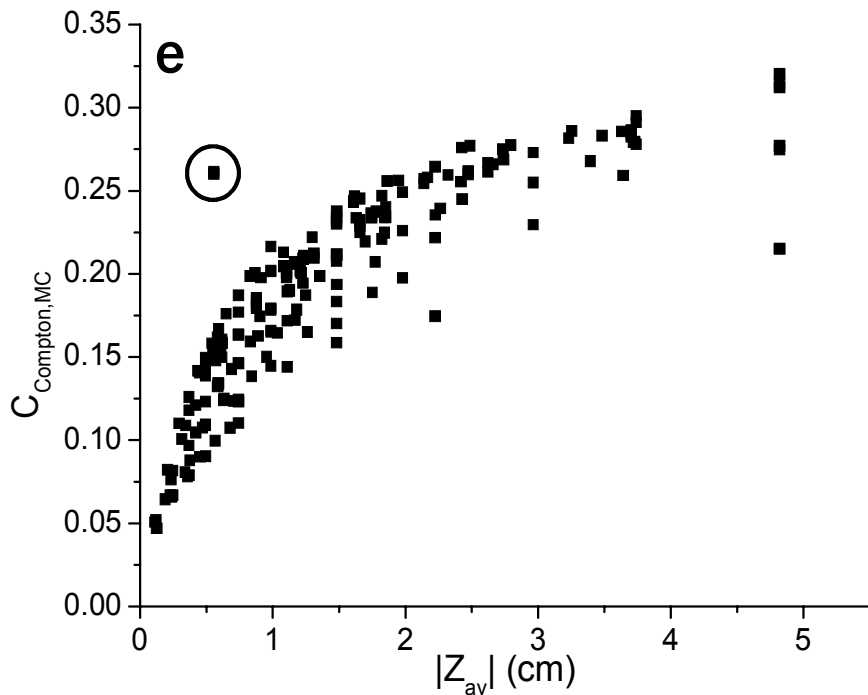


Figure 4e: $C_{Compton}$ dependency on $|Z_{av}|$, which is a combination of the dependency on path length and $|W_{in}|$, so the marked outlier has the same behaviour as in 4a.

Figure 4f: Correspondence between $C_{Compton,MC}$ and $C_{Compton,fit}$, derived from the fit that uses all data from $C_{Compton,MC}$.

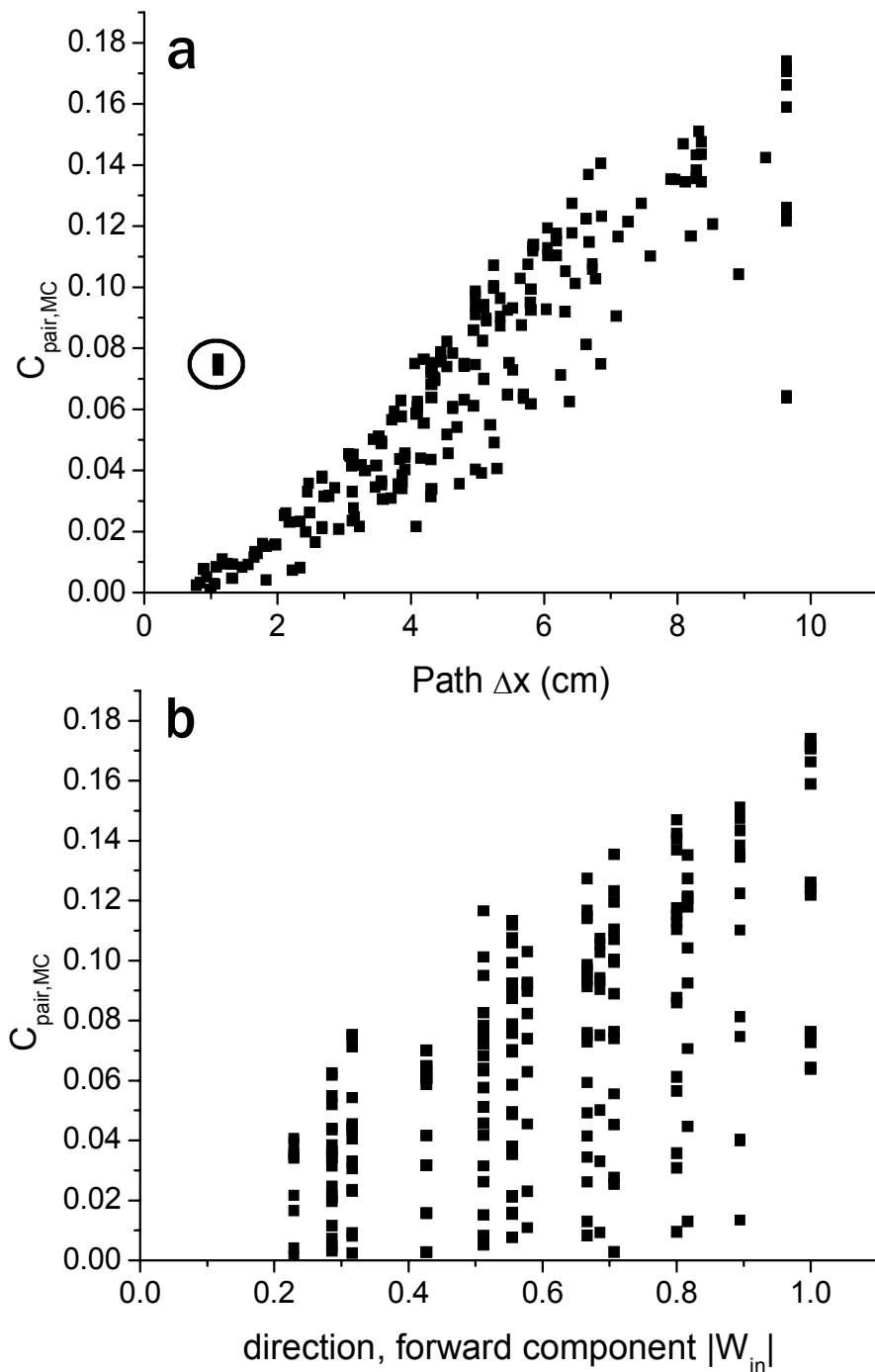


Figure 5a,b. C_{pair} dependencies and fit for simulation of 3 MeV gammas. Trends are roughly the same as in Figure 4, though C_{pair} is smaller than $C_{Compton}$. The marked outliers are again caused by the path of the gamma crossing the inactive core of the crystal. Comparing Figure 4 and Figure 5 to more detail, some differences show up. In Figure 4a and Figure 5a, the dependency on Δx seems for small Δx for C_{pair} more $\propto \Delta x^2$ and for $C_{Compton}$ more $\propto \Delta x$. In Figure 5b a trend $\propto |W_{in}|$ is more clear than in Figure 4b.

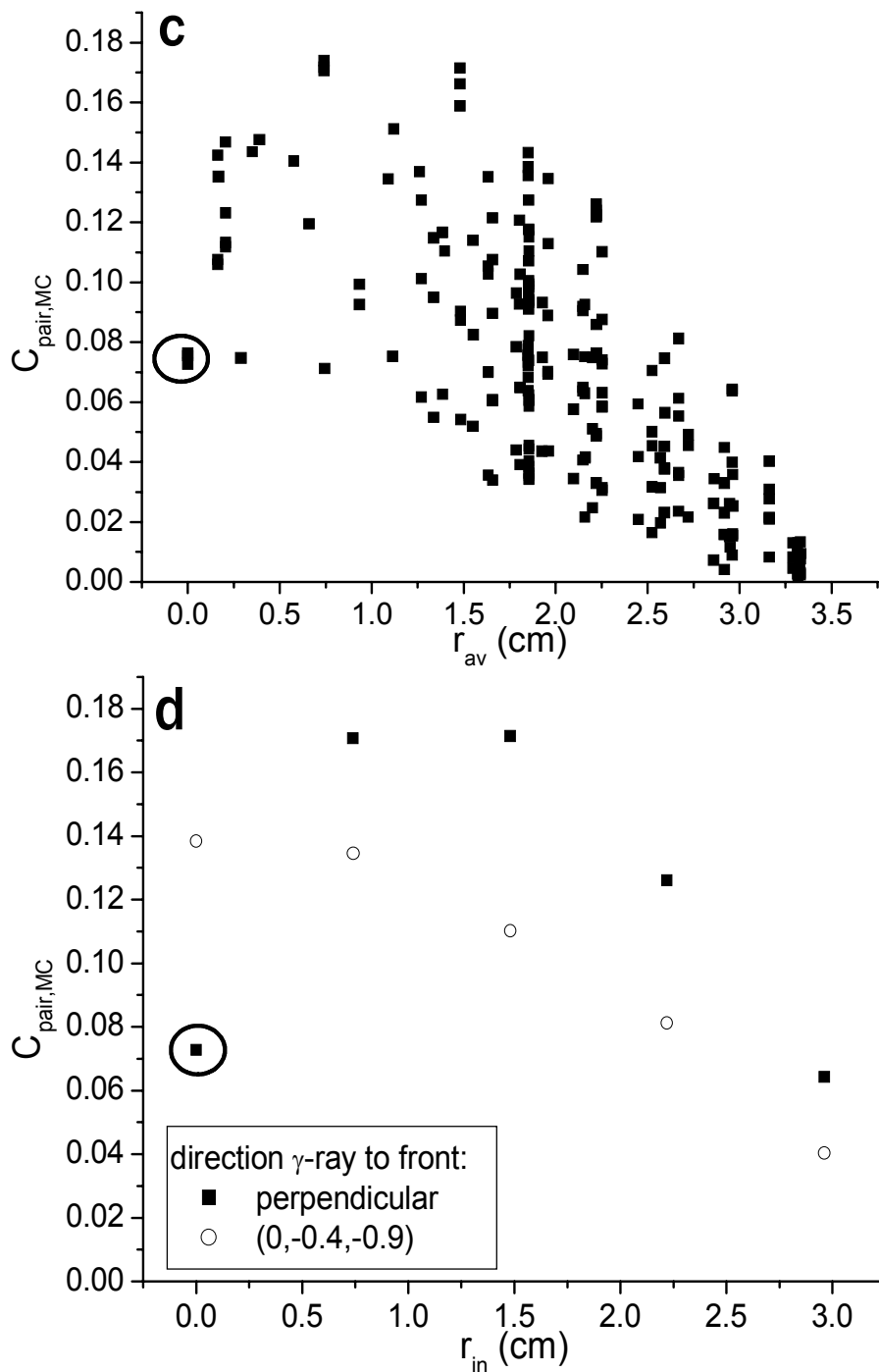


Figure 5c,d. $C_{\text{pair,MC}}$ dependency on r_{av} , r_{in} and angle of incidence. In Figure 4c,d previously mentioned outliers are marked. It can be concluded that dependencies on r_{in} and r_{av} are steeper for C_{pair} than for C_{Compton} . This difference may be caused by the fact that after a pair creation there are two gammas instead of one after a Compton interaction.

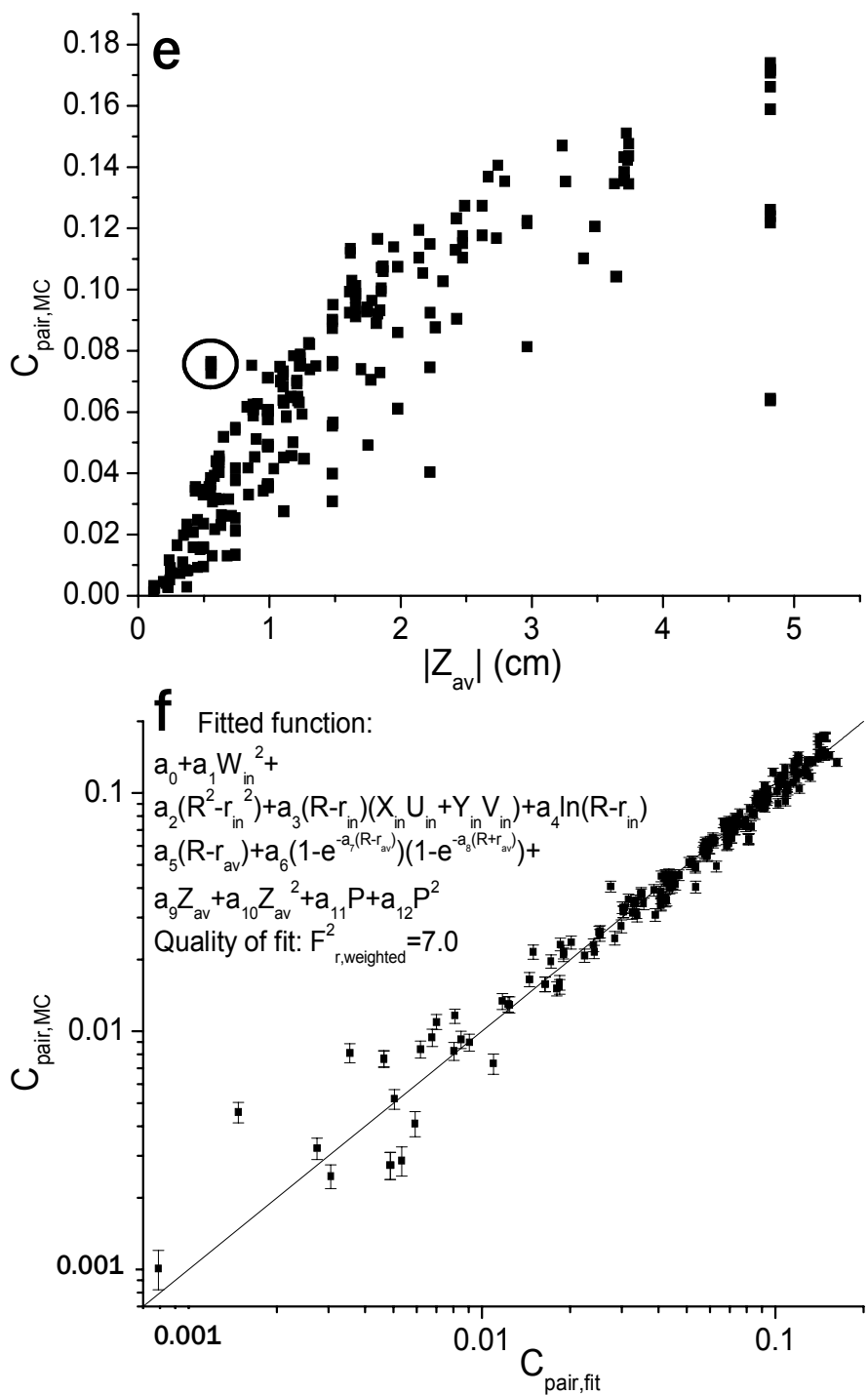


Figure 5e,f. C_{pair} dependency on $|Z_{av}|$. The different values for C_{pair} at $|Z_{av}| \approx 5$ cm are due to different r_{in} .

Figure 5f. Correspondence between $C_{pair,MC}$ and $C_{pair,fit}$, derived from the fit that uses all data from $C_{pair,MC}$. The fit for C_{pair} is worse than for $C_{Compton}$. The polynomial for C_{pair} probably should be more complex than for $C_{Compton}$ to describe better the paths of two gammas after pair creation instead of one after the Compton interaction.

The fitted function is composed in the same way as for $C_{Compton}$, now using knowledge from 4.2.3 and trends in Figures 5a-e.

C_{pair} does not vary significantly between 1.4, 2.0 and 3.0 MeV. So, according to our assumption, at least up to 3.0 MeV, C_{pair} does not depend significantly on E_γ . The quality of the fit, described by $F_{r,weighted}^2 = 7.0$, is worse than for C_{photo} and $C_{Compton}$ and no improvement was found by adding more elements to the function in Equation 18. It should be noticed though, that the contribution of C_{pair} to the detection efficiency is much less in the modelled range of E_γ than C_{photo} and $C_{Compton}$. Therefore, the quality of the modelled efficiency will not be significantly influenced within this range.

4.4.4 All correction factors together

The $F_{r,weighted}^2$ for the three fitted energy-dependent correction functions is plotted in Figure 6. The best fit on normally distributed data would render a $\chi_{r,weighted}^2$ of 1. It can be seen that above 1 MeV the values for $F_{r,weighted}^2$ become significantly larger than unity, which means that for these energies the fit-functions describe the behaviour of full energy detection less accurately.

The figure also demonstrates that for $C_{photo} \approx 1$, $F_{r,weighted}^2$ quickly reduces to 0. This makes clear that $F_{r,weighted}^2 \neq \chi^2$. This is due to at least two reasons: (1) the data are fitted towards guessed polynomial functions and (2) F^2 differs from χ^2 by a factor $C_{kl,MC}$.

4.4.5 Implementation and test of the efficiency calculation

The cross-sections for photon interactions with germanium are calculated from [11]. The cross-section for a Compton interaction is well described by:

$$\left(\frac{\mu}{\rho}\right)_c = \frac{Z}{A} N_{Av} \sigma_{KN}, \quad (19)$$

where for germanium, the density $\rho = 5.32 \text{ g/cm}^3$, the atomic number $Z = 32$ and the average atomic mass of $A = 72.6 \text{ g/mol}$; $N_{Av} = 6.023 \times 10^{23}$ is Avogadro's number and σ_{KN} is the Klein-Nishina function of the Compton total cross section

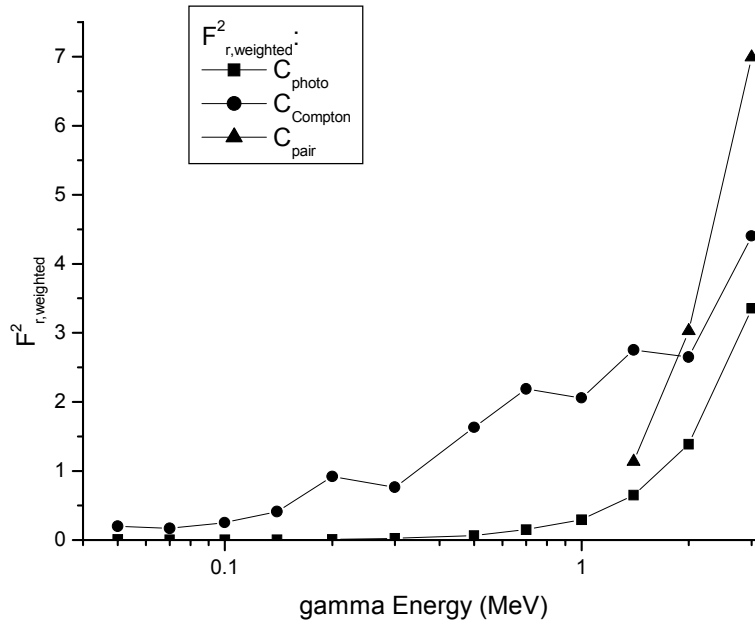


Figure 6 Quality of fitted correction factors, presented as a function of the energy of the original gamma.

[12]. For speeding up the calculations, the photo-effect cross-section is approximated to within 2% in the gamma energy range 0.05-10 MeV by:

$$\left(\frac{\mu}{\rho}\right)_{ph} = 3.77 \cdot 10^{-4} \left(\frac{E_{\gamma}}{1\text{MeV}}\right)^{-1.22} + 3.26 \cdot 10^{-4} \left(\frac{E_{\gamma}}{1\text{MeV}}\right)^{-3.06}, \quad (20)$$

and for $E_{\gamma} > 1.022$ MeV the cross section for pair creation is approximated to within 5% by:

$$\left(\frac{\mu}{\rho}\right)_{pair-nuc} = -0.0194 \cdot \cos(1.49 \cdot \log\left(\frac{E_{\gamma}}{1\text{MeV}}\right) - 0.0830) + 0.0194. \quad (21)$$

For Equation 20 and 21, the coefficients have been fitted to tabulated values [11]. For pair creation, only the nuclear cross section is taken into account, the electron cross section becomes only significant at higher E_{γ} than the range currently of interest.

Figure 7 and 8 show the results for the verification of the model with measured detection efficiencies of a calibrated source. For the 97% HPGe detector, to be used in REDNAILS, the model approximates the measured efficiencies generally to

within 5 percent and occasionally to within 10 percent, which is accurate enough for scanned measurements, where other sources of error are larger. Besides, in REDNAILS this deviation is corrected by calibration using Equation 13. For the other, 17% Ge(Li) detector, the model approximates the measured efficiencies to within 10 percent. The deviations are mainly that the model overestimates the efficiency compared to the measurement, since the model does not correct for effects like incomplete charge collection.

In Figure 9, the calculated and measured detection efficiencies for the 1408 keV gamma-ray line of ^{152}Eu are presented for the collimated detector configuration to be used for scanned measurements. For most points the model represents the measured efficiencies to within the statistical error of the measured peak areas. Outliers are at the collimator edge, i.e. source positions relative to the detector just behind the edge of the collimator. There the calculations underestimate the efficiency, probably due to the fact that the real collimator settings are not as precisely set as in the model: The slit opening is 2 ± 0.2 cm, the collimator thickness is 10 ± 0.15 cm and copper bolts are used to connect the 4 pieces each collimator consists of. This explains why the measured efficiencies suggest that the collimator opening is a little wider than 2 cm.

4.5 Discussion and conclusions

From Figure 7 and 8 it can be concluded that the model developed agrees well enough with the measured efficiencies up to gamma ray energies of 1.8 MeV, for point sources on the detector symmetry axis. For higher energies the multiple scattering may disturb the reconstruction, which may be assumed on the basis of trend of the values for the fitted $F_{r,weighted}^2$ at the higher gamma energies, as shown in Figure 6.

The modelled data in Figure 7 and 8 show some minor irregularities in the gamma-energy dependent efficiency curves, which causes the modelled lines to not be completely smooth. This may be due to the fitting of the gamma-energy dependent polynomials for the a_i coefficients for $C_{Compton}$ and C_{pair} respectively. The use of these polynomials for interpolation in the energy dimension can be obviated

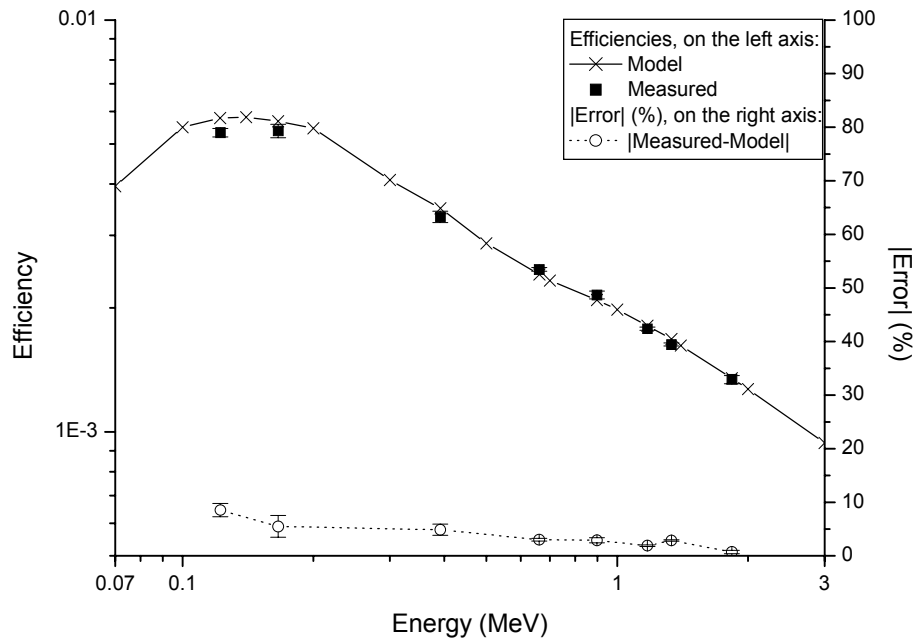


Figure 7 Verification of the model for the 97% HPGe detector with a source at 20 cm on the detector symmetry axis.

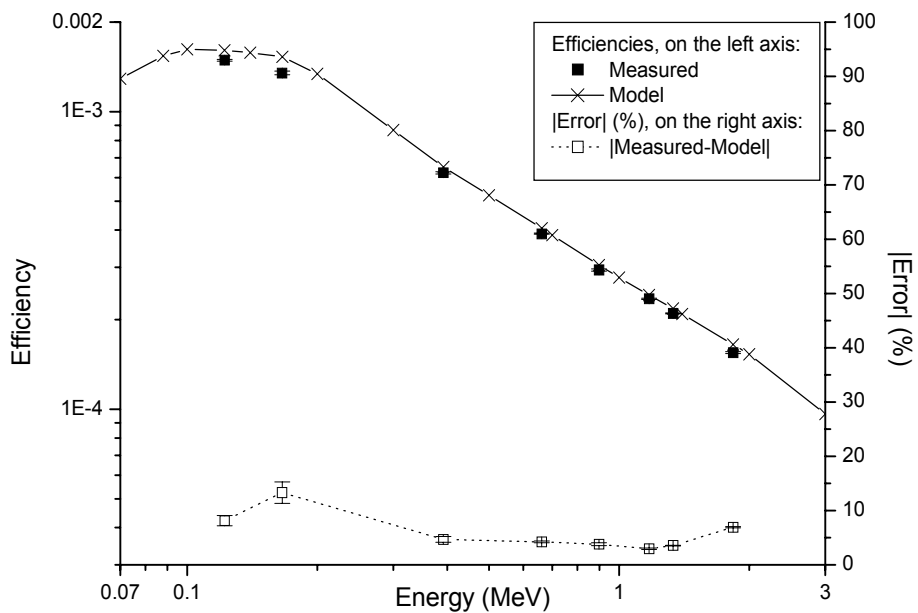


Figure 8. Verification of the model for the 17% Ge(Li) detector with a source at 25 cm on the detector symmetry axis.

by using the fitted coefficients found for the actual gamma energies used in de Monte-Carlo simulation to calculate the photo-peak efficiency for the required geometry for these gamma energies, and then by interpolating the efficiency for the required gamma energy in the required geometry using e.g. Gunnink's efficiency polynomial [1].

Calculation of the detection efficiency with this newly developed method is about 300-1000 times faster than Monte Carlo simulations of that detection efficiency with an imprecision of 1%.

Because the efficiencies calculated by the model generally differ only about 5% from measured efficiencies, this model can be used as a reliable and fast replacement for Monte Carlo simulations, especially for scanned measurements where large fractions of the sample are out of focus of the collimator and hence have a low detection efficiency.

Figure 8 suggests that the modelled efficiency for the 17% Ge(Li) detector contains a systematic error. This error may be based on incorrect assumptions

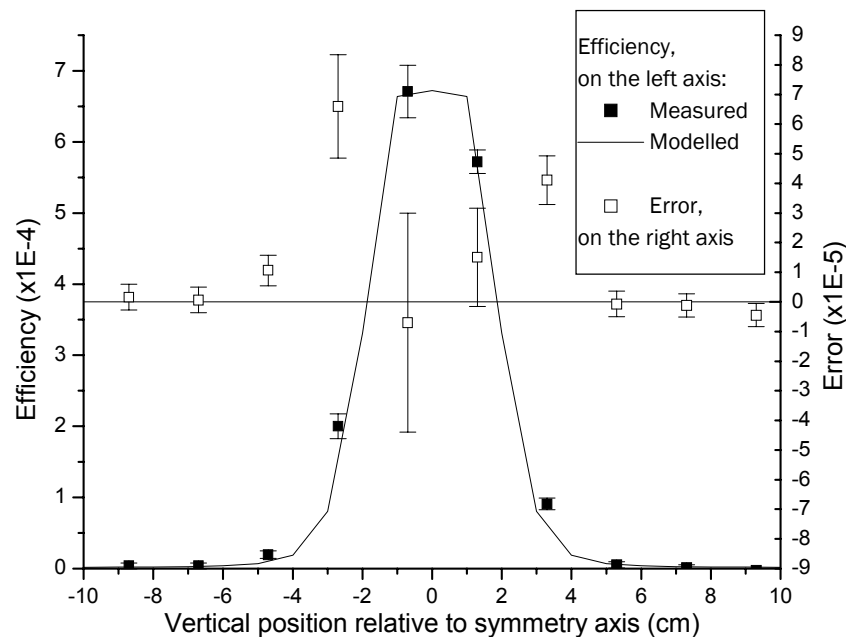


Figure 9 Verification of the model for scanned measurements with the 97% HPGe detector of 1408 keV gamma radiation. Errors presented on the right axis are absolute and give the difference between modelled and measured efficiencies. Error bars are derived from the standard deviations in the peak areas. Errors from the modelled data are not accounted for since it is assumed that they are relatively small (1%).

about the dimensions of the dead layer of the detector. This error is removed by correction of the modelled efficiency for this type of errors with Equation 13. The 97% detector does not show such a systematic deviation of calculated efficiencies from measured efficiencies. This demonstrates that the model can be applied to this detector for efficiency calculations on scanned measurements.

From Figure 9 it can be concluded that the model can be used for efficiency calculations in the set-up for scanned measurements with a collimator.

Finally, the results of the final experiment support the assumption that neglecting the gamma-rays impinging on the side wall of the shielded and collimated detector, as done in the efficiency calculations, still gives a proper result for the detection efficiency.

4.6 References

1. R. Gunnink, A.L. Prindle, J. Radioanal. Nucl. Chem. 160 (1992) 305.
2. L. Moens, J. De Donder, Lin Xi-lei, F. De Corte, A. De Wispelaere, A. Simonits, J. Hoste, Nucl. Instr. Meth. 187 (1981) 451.
3. V.L.C. Procida Veissid, G. Kenchian, M.T.F. Da Cruz, Nucl. Instr Meth A 309 (1991) 222.
4. M.E. Hosseini-Ashrafi, N.M. Spyrou, Appl. Radiat. Isotopes 43 (1992) 1449.
5. M.B. Alamin, N.M. Spyrou, J. Radioanal. Nucl. Chem. 215 (1997) 205.
6. R.M.W. Overwater, P. Bode, J.J.M. De Goeij, Nucl. Instr. And Meth. Phys. Res. A 324 (1993) 209.
7. K. Gehrcke, Kernenergie 33 (1990) 21.
8. I.O.B. Ewa, D. Bodizs, Sz. Czifrus, Zs. Molnar, Appl. Radiat. Isotopes 55 (2001) 103.
9. F. Hernandez, F. El-Daoushy, Nucl. Instr. And Meth. Phys. Res. A. 498 (2003) 340-351
10. W.R. Nelson, H. Hirayama, D.W.O. Rogers, SLAC-265, Stanford Linear Accelerator Center, Stanford, California, 1985.
11. M.J. Berger, J.H. Hubbell, H.D. Lemmel, XCOM: Photon cross-sections on a PC. Version 1.2 of 9 May 1987, International Atomic Energy Agency, Vienna (Austria). Nuclear Data Section.
12. O. Klein, Y. Nishina, Z. Physik 52 (1929) 853.

Chapter 5

Optimisation of the LS-INAA measurement facility for scanned measurements

5.1 Introduction

The LS-INAA measurement facility was originally designed for integral measurements of 0.1-3.0 MeV gamma-rays originating from the samples. This facility now had to be adjusted to enable the determination of the spatial distribution of the elements as well.

Determination of spatial distributions of radioactivity in large volumes, either of activated elements, or other radionuclides in e.g. waste barrels, requires a measurement system with a spatial resolution power, e.g. a gamma camera. The distribution is reconstructed on basis of projections of the emitted radiation at different positions and angles relative to the sample (*i.e.* Single Photon Emission Computed Tomography). Usually, tomography leads to a reconstruction of the distribution over cubic volume parts or voxels of the sample.

Another requirement is a number of collected counts large enough for a stable reconstruction of the spatial distribution. This requirement sets a lower limit to the product of detection efficiency, sample activity concentration and measurement time. REDNAILS samples have a relatively low activity, typically < 1 MBq, and measurement times are restricted by the decay times of the activated elements of interest, often < 1 d, *i.e.* the maximum measurement time of the total scan is limited to 1 d. As a consequence, the detection efficiency has to be higher than in comparable arrangements for reconstruction of distributions [1] of higher-

activity radioactive elements with longer half-lives, or of higher-activity distributions in nuclear power plant fuel pellets [2].

Furthermore, the energy resolution of gamma-cameras as used in tomography is not sufficient for spectrum interpretation based on resolved peaks as applied in NAA. Only Ge detectors allow for these analyses. Therefore, an optimum facility would comprise a large HPGe detector, with a large peak-to-Compton ratio and a large detection volume resulting in a full-energy detection efficiency as high as possible. For REDNAILS, the LS-INAA counting facility as described in Chapter 1, containing such a detector, was applied, though it had to be modified to meet other constraints as well.

In order to obtain a spatial resolution, the sample is scanned, *i.e.* translated and rotated in front of the detector, and spectra are collected for each position relative to the detector. To further improve the spatial resolution of the signal, the detector is collimated. However, the collimation decreases the detection efficiency, therefore the collimator must be optimised for REDNAILS.

For reconstruction of the spatial distribution in a Cartesian voxel (x,y,z) approach, as for the set-ups for long-lived radionuclides [1, 2], a pinhole-shaped collimator or combination of collimator and detector is required. The disadvantages would be (i) a decrease of detection efficiency and (ii) an increase of the number of measurements to get projections of the activity of the sample. The requirement of the measurements being performed in less than one day could not be met that way. Therefore, this approach has not been considered any further.

On the other hand, the LS-INAA irradiation and measurement facility was specifically designed for cylindrically shaped samples, and for most envisaged samples of this shape, being borehole logging samples, the distribution in the vertical direction is mainly of interest. Therefore a horizontal-slit shaped collimator has been built, somewhat like a Soller-Collimator [3]. However, the method should also detect extreme inhomogeneities within a layer that -if not detected- may disturb the analysis results [4]. To that end, the sample can be measured in different rotational positions to determine a rough horizontal distribution.

In this chapter, calculations and measurements are described that were performed to optimise the measurement set-up for REDNAILS. Scan steps and collimator shape determine the spatial resolution and the detection efficiency of

the voxel in the focus of the collimator opening. First, a short summary is given of the measurement procedure to clarify the collimator parameters to be optimised.

When the sample is divided in voxels and it is assumed that the elemental distribution and the gamma-ray attenuation coefficients are constant within each voxel, the measured peak areas in measurement j , after correction for background and natural activity, can be described with the activation formula corrected for large samples, Equation 4 in Chapter 3, summed over all voxels i and nuclides n that emit photons with energy E_γ [J]:

$$A_j(E_\gamma) = \sum_{n,i} \int_{\text{voxel } Vol_i} \Phi_{th}(\vec{r}_i) \sigma_{n,th} \frac{N_{Av} \theta_n w_{ni}}{M_n} (1 - e^{-\lambda_n t_{ir}}) e^{-\lambda_n t_{d,j}} \frac{1 - e^{-\lambda_n t_{m,j}}}{\lambda_n} \gamma_n(E_\gamma) \varepsilon_{ij}(E_\gamma, \vec{r}_i) d\vec{r}_i, \quad (1)$$

where Φ_{th} [$m^{-2}s^{-1}$] is the thermal neutron flux $\sigma_{n,th}$ [m^2] is the thermal neutron cross section for nuclide n , θ the isotope abundance, w_n [g] the mass of the element related to nuclide n in voxel i , N_{Av} Avogadro's number ($6.022 \times 10^{23} \text{ mol}^{-1}$) and M_n [g/mol] the atomic mass, λ_n [s^{-1}] the decay-constant, t_{ir} [s] the irradiation time, t_d [s] the decay time before measurement j and t_m [s] measurement time for measurement j , $\gamma(E_\gamma)$ the emission probability per decay-event for a gamma with energy E_γ and $\varepsilon_{ij}(E_\gamma, \vec{r}_i)$ the detection efficiency for a gamma with energy E_γ originating from position \vec{r}_i . Voxels and measurements are labelled in such a way that if $i = j$ than voxel i is right in front of the collimator opening.

The probability that a photon of energy E_γ will be detected depends on the attenuation in the sample, the collimator, the distance to the detector, and the detection efficiency of the detector:

$$\varepsilon_{ij,tot}(E_\gamma) = \int_{\text{voxel}} \varepsilon_{ij,sample}(E_\gamma) \varepsilon_{ij,col}(E_\gamma) \varepsilon_{ij,det}(E_\gamma) dV, \quad (2)$$

where $\varepsilon_{ij,tot}$ is the energy dependent detection efficiency for a source in voxel i in measurement j , the subscripts *tot*, *sample*, *col* and *det* indicate the total, sample, collimator and internal detector detection efficiency respectively. The geometry and the elemental composition of both collimator and detector are known, and their contributions to the detection efficiency can be calculated or determined via the method described in Chapter 4. The elemental composition, and hence the gamma-ray attenuation, of the sample is not known and may vary

from sample to sample, from layer to layer and even within a layer. Therefore the attenuation of each voxel has to be determined as well. This is described in Chapter 7.

The optimisation of the measurement set-up is based on Equation 2, but cannot be derived in a straightforward manner. The parameters that could be varied for optimisation are collimator composition, its position, its thickness, the slit opening, the slit shape and the number of rotation steps. The optimisation itself is towards a maximum for the detection efficiency ε_{ij} ($j = i$) of voxel i directly in front of the collimator in measurement j ($j = i$), with a minimum for the sum of the detection efficiencies for the other voxels in measurement j ($j \neq i$). Hence the gamma-energy dependent ratio $\varepsilon_{ij}(j = i)/\sum_{j \neq i} \varepsilon_{ij}$ is maximised for the gamma-energy spectrum of interest. This is done with constraints on the decrease of $\varepsilon_{ij}(j = i)$ (in the case that with decreasing $\varepsilon_{ij}(j = i)$, $\sum_{j \neq i} \varepsilon_{ij}$ decreases even more) in order to allow counts being collected from samples with a relatively low radioactivity concentration. Also the optimum number of rotation steps is studied.

Finally the use in practice will be discussed taking into account the strongly situation-dependent constraints for sample activity and requirements for detection limits.

5.2 Theory

5.2.1 position and thickness of the collimator

The best spatial resolution and detection efficiency for the voxel in front of the detector is found for collimator and detector positioned as close as possible to the sample. Then, it is expected that the maximum efficiency for the voxel in front of the detector is reached for a collimator opening of the same height as the voxel. Voxels in the other layers will 'see' a smaller part of the detector relative to other collimator positions.

The ratio $\varepsilon_{ij}(j = i)/\sum_{j \neq i} \varepsilon_{ij}$ is sensitive to the collimator thickness in that sense that both ε_{ij} and $\sum_{j \neq i} \varepsilon_{ij}$ will be reduced, but $\sum_{j \neq i} \varepsilon_{ij}$ more which makes that $\varepsilon_{ij}(j = i)/\sum_{j \neq i} \varepsilon_{ij}$ increases with increasing collimator thickness. But in order to limit the decrease of $\varepsilon_{ij}(j = i)$, the thickness has to be limited.

5.2.2 composition of the collimator

A collimator with the best shielding properties should absorb radiation rather than scatter. Therefore the collimator should be composed of a material with a high atomic number and a high density.

5.2.3 collimator slit and voxel size

In measurement j , the detection efficiency of voxel $i = j$ for the gamma-ray energy (range) of interest, $\varepsilon_{ij}(j = i)$ must be maximised for a good reconstruction of the activity in each voxel. Activity in other voxels is also measured but with a lower detection efficiency. An optimum must be found for the ratio $\varepsilon_{ij}(j = i)/\sum_{j \neq i} \varepsilon_{ij}$. This ratio is influenced by the voxel size. If the system is collimated, then the collimator will improve this ratio as well.

For best spatial resolution one wants to minimise the voxel size, but then the total number of voxels will increase and hence the fraction of the total activity that is in the voxel will decrease. If a collimator is used, then detection efficiencies will decrease with decreasing voxel size as well: $\sum_{j \neq i} \varepsilon_{ij}$ will be reduced as well as $\varepsilon_{ij}(j = i)$, so this may change the ratio to be optimised, $\varepsilon_{ij}(j = i)/\sum_{j \neq i} \varepsilon_{ij}$.

For a theoretical elaboration, a sample is considered with an homogeneous activity divided in layers of d cm, with a total height h and negligible diameter, at distance L from a detector with diameter $D \gg d$, and a collimator thickness c and slit size d (see Figure 1), in the simplified theoretical case that $\varepsilon_{ij,tot} = \varepsilon_{ij,col}$, i.e. assuming that there is no attenuation in the sample and all photons that reach the detector are completely detected: in Equation 2 $\varepsilon_{ij,sample} = \varepsilon_{ij,det} = 1$, the following approximation can be made:

$$\varepsilon_{ij,uncoil}(j = i) = \frac{\frac{1}{4}\pi D^2}{4\pi L^2} = \frac{D^2}{16L^2} \quad (3)$$

Assuming that $\varepsilon_{ij,col}(j = i)$ mainly depends on the area of the detector that is visible through the collimator opening: width \times height = $D \times dL/c$, $\varepsilon_{ij,col}(j = i)$ can be written as:

$$\varepsilon_{ij,col}(j = i) = \frac{DdL}{c} \frac{1}{4\pi L^2} = \frac{dD}{c4\pi L} \quad (4)$$

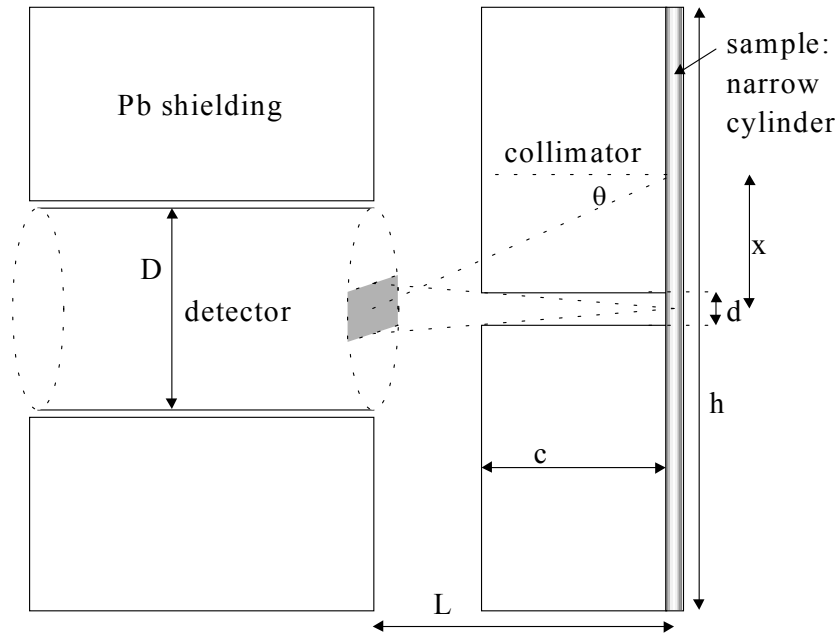


Figure 1 Schematic drawing of the measurement set-up for LS-INAA, where a slit collimator is added for scanning measurements

On the other hand, $\sum_{j \neq i} \varepsilon_{ij}$ can be written as an integral, when divided by d , assuming $d \ll h$:

$$\sum_{j \neq i} \varepsilon_{ij, uncol} \approx 2 \int_0^{\frac{1}{2}h} \frac{\pi D^2 \cos \theta}{4\pi d(L^2 + x^2)} dx = \frac{D^2 L}{2d} \int_0^{\frac{1}{2}h} \frac{dx}{(L^2 + x^2)^{3/2}} = \frac{D^2 h}{2Ld \sqrt{4L^2 + h^2}} \quad (5)$$

and:

$$\sum_{j \neq i} \varepsilon_{ij, col} \approx 2 \int_0^{\frac{1}{2}h} \frac{\pi D^2 \cos \theta e^{-\frac{\mu c}{\cos \theta}}}{4\pi d(L^2 + x^2)} dx \approx \frac{D^2 L e^{-\mu c'}}{2d} \int_0^{\frac{1}{2}h} \frac{dx}{(L^2 + x^2)^{3/2}} = \frac{D^2 h e^{-\mu c'}}{2Ld \sqrt{4L^2 + h^2}}, \quad (6)$$

where $c' = \mu c / \cos(\theta)$. Now two approximations can be written:

$$\frac{\sum_{j \neq i} \varepsilon_{ij, col}}{\sum_{j \neq i} \varepsilon_{ij, uncol}} \approx e^{-\mu c'} \quad (7)$$

and

$$\frac{\varepsilon_{ij,col}}{\varepsilon_{ij,uncol}}(j=i) \approx \frac{4dL\pi}{Dc}. \quad (8)$$

Defining the average efficiency ‘density’ for the collimated voxels: $\bar{\varepsilon} \equiv \frac{d}{h} \sum_{j \neq i} \varepsilon_{ij,uncol}$, where $\bar{\varepsilon}$ is independent of d , renders:

$$\frac{\varepsilon_{ij,col}(j=i)}{\sum_{j \neq i} \varepsilon_{ij,col}} \approx \frac{dD}{4\pi c L e^{-\mu c'} \sum_{j \neq i} \varepsilon_{ij,uncol}} = \frac{d^2 D}{4\pi c L e^{-\mu c'} h \bar{\varepsilon}}. \quad (9)$$

So, considering a homogeneous sample, the ratio of the contribution of the voxel in front of the detector to the peak area A_j over the contribution of the other voxels will be proportional to d^2 , d being the height of both the layer and the collimator slit opening.

Therefore, the collimator opening should be chosen as large as possible for maximisation of the ratio currently of interest. But for an opening

$$d > \frac{Dc}{L}, \quad (10)$$

the efficiency will no longer increase, because the voxel in front of the detector now ‘sees’ the total detector area.

5.2.4 rotation steps

Real samples usually have a diameter of about 7-12 cm and inhomogeneities within a layer may influence the measurement as well. Therefore the measurement of a layer has to be optimised as well.

Each layer can be measured under different horizontal angles in order to get information about the activity distribution within a layer. Now a layer is considered to consist of a number of wedge-of-cake shaped voxels. The number of rotation steps or voxels can be optimised for a minimum variation of the efficiency within the voxel and a maximum ratio of the voxel in front of the detector over its neighbouring voxels.

5.2.5 other collimator shape

A 100% radiation-absorbing slit-collimator close to the sample will not perfectly shield the radiation originating from the neighbouring layers, due to geometrical leakage. The collimator can be improved by adding one or more horizontal sheets of lead in the middle of the collimator opening (see Figure 2). Such a sheet will mainly attenuate gamma radiation that passes the collimator less horizontally than gamma radiation originating from the voxel in front of the detector. Therefore, as indicated in Figure 2, the sheet will mainly absorb radiation from the neighbouring layers.

5.3 Methods

The measurement set-up is optimised for the ratio $\varepsilon_{ij}(j=i)/\sum_{j \neq i} \varepsilon_{ij}$ by determining the optimum collimator composition, shape and opening as well as the number of rotation steps. The constraint of a gamma-energy range as opposed to a single (optimised) gamma energy, was satisfied by modelling the efficiency

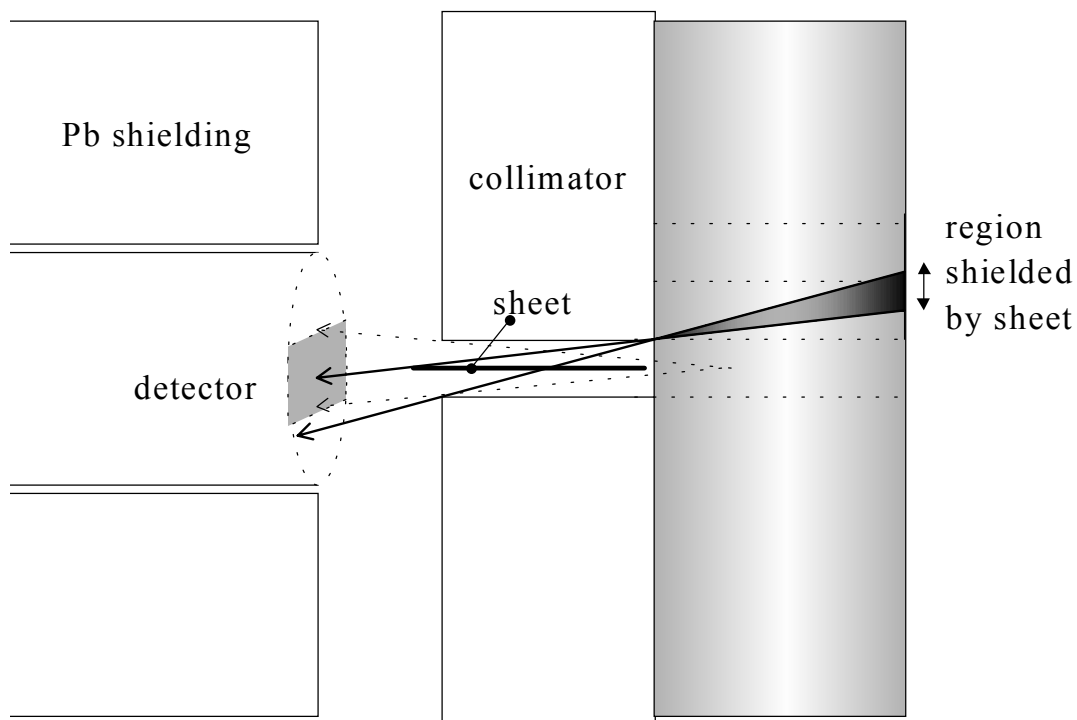


Figure 2 Schematic drawing of the measurement set-up for large sample scanning measurements, where a horizontal lead sheet is added in the centre of the collimator for improvement of the vertical resolution

using the method described in Chapter 4, for the desired energy range. The change of the collimator shape (*i.e.* the insertion of sheets) was tested by measurements

5.3.1 Position and thickness of the collimator

For preliminary experiments, a 10 cm thick collimator had been horizontally fixed to the system that contains the detector and its shielding at 7 cm (L-c) relative to the detector end cap, see Figure 2. The detector and collimator can be placed as close as possible to the sample. This was done without further optimisation studies on the position.

The collimator thickness c had been enlarged in a previous stadium from 5 to 10 cm. Steps of 5 cm were chosen based on the availability of Pb bricks of this size. Further increase of the collimator thickness was limited in order to limit the decrease of $\varepsilon_{ij,col}(j = i)$ being proportional to c^{-1} according to Equation 4, since L is fixed because the collimator is placed as close as possible to the sample, which is at a fixed distance to the detector.

5.3.2 composition of the collimator

The efficiency was modelled for a source at a horizontal distance of 25 cm from the detector end cap (*i.e.* equal to the centre of a sample of 8 cm diameter), a radius of 0 cm and a vertical height of 2 cm, equal to the collimator opening, scanned over neighbouring layers in steps of 2 cm. The modelling was done for gamma-ray energies of 120, 334, 662 and 1408 keV. Two types of collimator material were modelled for optimisation: lead and tungsten, both often used as collimator material, with densities of 11.34 g/cm³ and 19.3 g/cm³, and atomic numbers 82 and 74 respectively.

5.3.3 collimator slit and voxel size

To determine an optimum collimator opening and hence layer height, the efficiency was modelled for a source at a horizontal distance of 25 cm from the detector end cap, a radius of 0 cm and the same gamma ray energies. The vertical height was varied over 0.1-10 cm and the collimator opening was chosen equal to

that each time. The source was scanned over neighbouring layers in steps equal to the source height.

5.3.4 rotation steps

To determine the optimum number of rotation steps, the efficiency was modelled for the voxels in the layer in front of the detector for one through eight rotation steps. Also the variation of the efficiency within a voxel was modelled, by determining the efficiency of 25 subvoxels for each voxel. Now only one gamma-ray energy, 662 keV, was modelled and only one slit opening size, 2 cm.

5.3.5 other collimator shape

In a vertical scan of a ^{152}Eu point source, a horizontal Pb sheet ($l \times b \times h = 8.2\text{cm} \times 17\text{cm} \times 0.14\text{cm}$) was placed in the middle of the collimator opening, $d = 2$ cm, to improve the vertical resolution without too much loss of detection efficiency of the voxel in front of the detector (see Figure 2). Pilot experiments showed that adding more sheets would cost too much on detection efficiency compared to any gain on vertical resolution. The scanned measurements of 5 min per vertical step were performed with and without sheet.

5.4 Results

5.4.1 position and thickness of the collimator

The collimator position and thickness have not been optimised further.

5.4.2 composition of the collimator

In Figure 3, the modelled efficiency for a vertically translated source is presented for a lead versus a tungsten collimator of 10 cm thickness. No large difference is found for the two materials considering the layer in front of the detector and the first layer above and below (positions from -2 to 2 cm). Large relative differences can be seen in Figure 3b for other layers, tungsten performing better, but the absolute attenuation factor, μ , of lead is already over a factor 23 (at 1408 keV). Hence, the choice between lead and tungsten does not have a

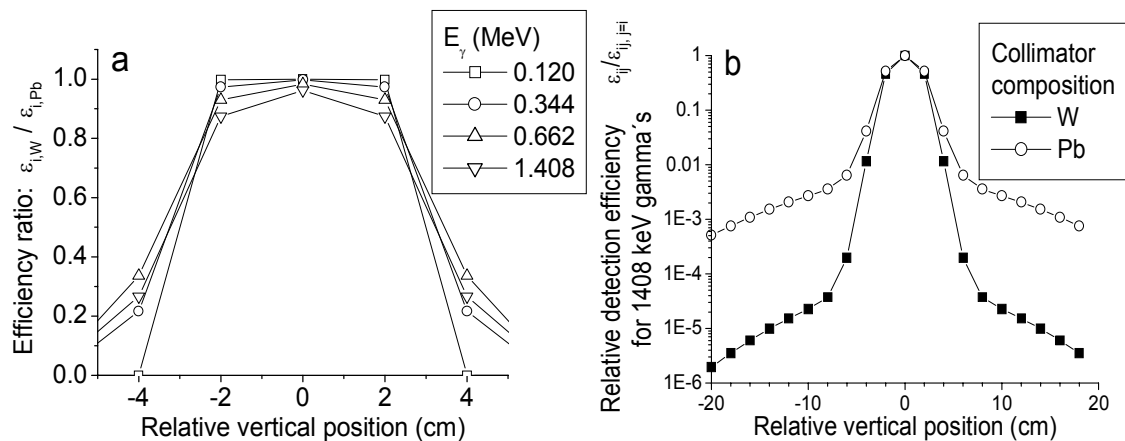


Figure 3 (a) Cross-talk ratios for scanned measurements with a collimator made of tungsten versus a collimator made of lead, calculated for four gamma-ray energies and a layer height and slit size of 2 cm and (b) same efficiencies for 1408 keV now relative to $\epsilon_{ij}(j=i)$.

significant impact on $\epsilon_{ij}(j=i) / \sum_{j \neq i} \epsilon_{ij}$ or the FWHM of the spatial resolution. Therefore, for practical (economical) reasons, lead was chosen.

5.4.3 collimator slit and voxel size

Figure 4 shows the calculated efficiency of the voxel in front of the detector as a function of slit opening size, for four gamma-ray energies. The results show the derived relation in Equation 4 for small collimator openings of $\epsilon/d = \text{constant}$. Because the efficiency was not modelled immediately behind the collimator but at 8 cm distance, ϵ_{max} is reached according to Equation 10 changed to the current situation:

$$d = \frac{D(c+8)}{L} = 7.4 \times (10+8) / 25 \approx 5 \text{ cm.} \quad (11)$$

Figure 5 shows the results for the modelled efficiency or cross-talk ratios $\epsilon_{ij}(j=i) / \sum_{j \neq i} \epsilon_{ij}$, where $i=120$ i.e. the central voxel in a sample of $N_{vox} = 240$ voxels, for a series of collimator openings $2 \text{ mm} < d < 100 \text{ mm}$. It can be seen that the larger the voxel and slit opening is, the larger, i.e. better, the cross-talk ratio. It reflects that at larger voxels, the detection efficiency of the voxel in front of the detector

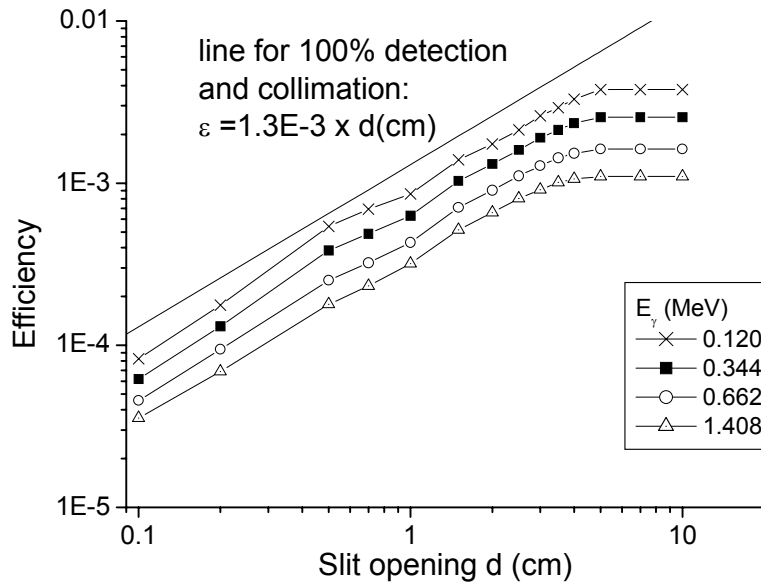


Figure 4 Efficiency ratios for measurements of a point source fixed at 25 cm (horizontally) from the detector end cap right in front of the collimator opening, calculated for slit sizes in the range of 2-100 mm for four gamma-ray energies. The straight line shows the detection efficiency for small collimator openings for a perfect collimator ($\mu=\infty$) and ideal detector ($\epsilon_{det}=1$).

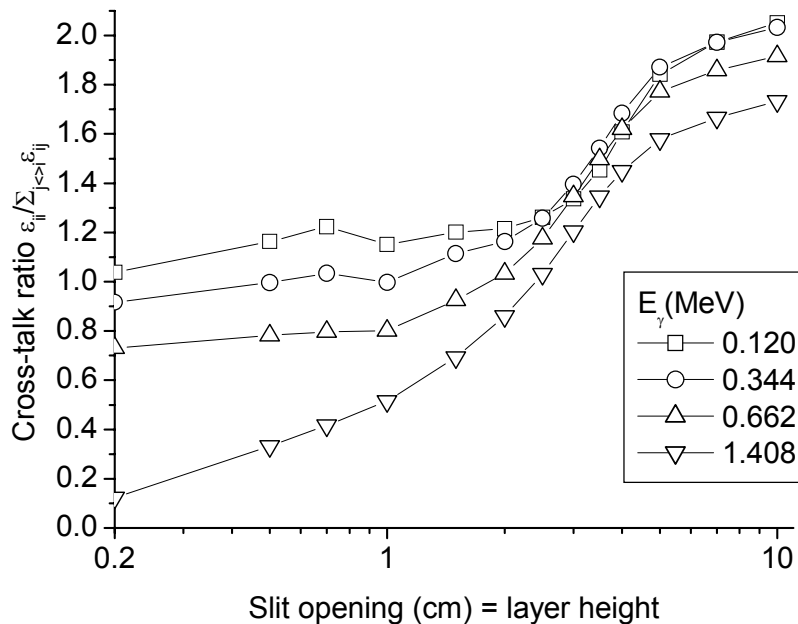


Figure 5 Cross-talk ratios for scanned measurements of a point source at 25 cm (horizontally) from the detector end cap, calculated for slit sizes in the range of 2-100 mm for four gamma-ray energies.

becomes larger and simultaneously the other voxels are further away to the detector due to the larger voxel size. The last effect means that the ratio increases even after the maximum efficiency of the voxel in front of the detector is reached (Figure 4).

In Figure 6, the results are plotted for the vertically scanned efficiency for 120 keV photons, where sample size is kept constant (5 mm layer height). Irregularities of smoothness of the maximums of the curves for collimator openings 2.0-3.5 cm are due to the roughness of the model: the summation of the efficiency over the detector end cap as explained in Chapter 3. This plot can be used to choose the optimum collimator opening for the required spatial resolution (FWHM) of the reconstructed activity distribution. The results show some artefacts at the central position that can be explained by the low (100) number of points and the symmetrical ordering thereof on the detector in the modelling.

5.4.4 rotation steps

Figure 7 shows the results for the modelled spatial variation of the efficiency within the voxel in front of the detector as a function of the number of rotation steps for a gamma-ray energy of 662 keV, central in the energy range of interest. It can be seen that the minimum variation is reached for 3 rotational

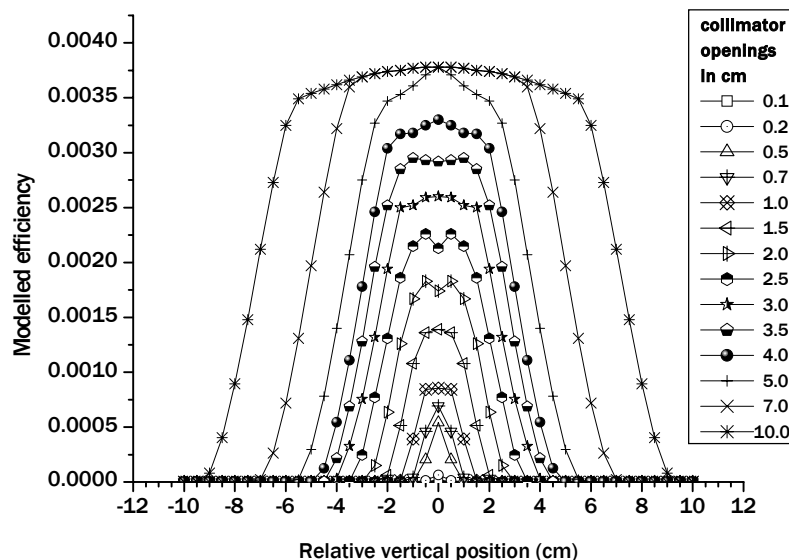


Figure 6 Modelled efficiencies for scanning measurements of a point source at 25 cm (horizontally) from the detector end cap, calculated for slit sizes in the range of 0.1-10 cm for 120 keV, scanning step sizes are 0.5 cm.

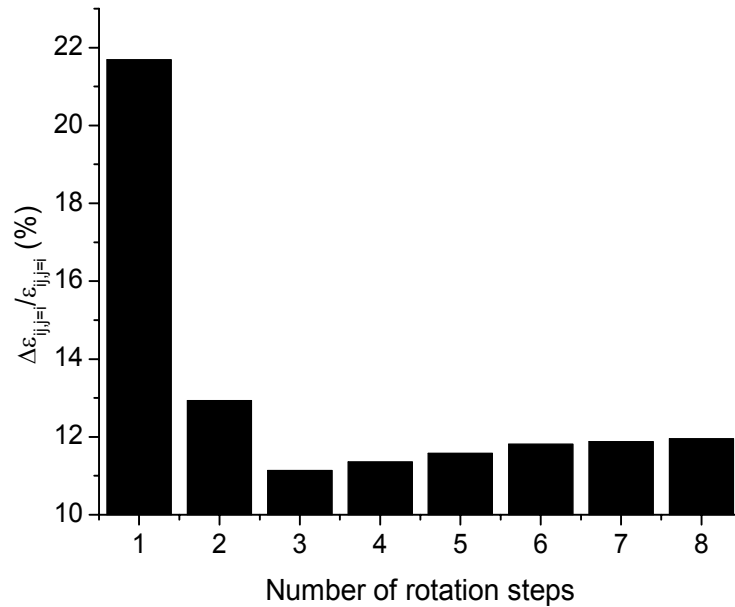


Figure 7 Calculated relative spatial standard deviation of efficiency ($\Delta\varepsilon/\varepsilon$) within the voxel in front of the detector for gammas of 662 keV and a 2 cm slit opening as a function of number of rotation steps and hence reciprocal voxel size.

steps.

Figure 8 shows the relative efficiency of the neighbouring voxel, compared to the efficiency of the voxel in front of the detector. The minimum contribution to the spectrum of neighbouring voxels is found at the lowest number of rotation steps, i.e. 2, but it can be seen that the difference between 2 and 3 steps is relatively small. Hence, considering Figure 7 and 8 together, the optimum number of rotation steps is 3.

5.4.5 other collimator shape

For three ^{152}Eu peaks, the peak area as function of the vertical position of the point source is compared for measurements with and without separation sheet in the collimator (Figure 9). Though the measured response is not necessarily Gaussian, fitting with a Gauss function,

$$y = y_0 + \frac{A}{w\sqrt{\pi}/2} e^{-\frac{(x-x_c)^2}{w^2}}, \quad (12)$$

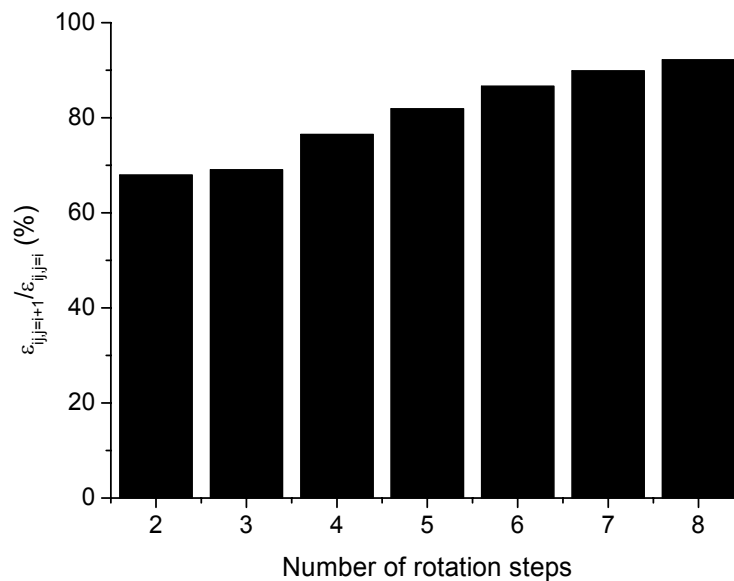


Figure 8 Calculated efficiency ratios for the voxel in front of the detector and its neighbour ($j=i+1$) as a function of the number of rotation steps, for gamma energy 662 keV and a 2 cm slit opening

illustrates the change in the response, where y_0 is the background (counts) or leakage radiation at $x = 0$, A the total area (counts), x_c the vertical position of the peak (cm) and hence the source, and w the peak width (cm). The width of the vertical response decreases when the sheet is applied, especially for lower energies. On the other hand, the peak height at $x=x_c$ decreases, and therefore the efficiency of the voxel in front of the detector.

The relative change of the peak width and the height at $x=x_c$, is presented as a function of gamma-energy in Figure 10. The change in peak height varies less with gamma-energy than the change in peak width. This results in the undesired effect that, for $E_\gamma \geq 1$ MeV, the decrease of the detection efficiency of the voxel in front of the detector is larger than the increase in spatial resolution, i.e. decrease of peak width. For instance for 1408 keV, applying the sheet renders a decrease in efficiency of 1.2 and a decrease in peak width of 1.0.

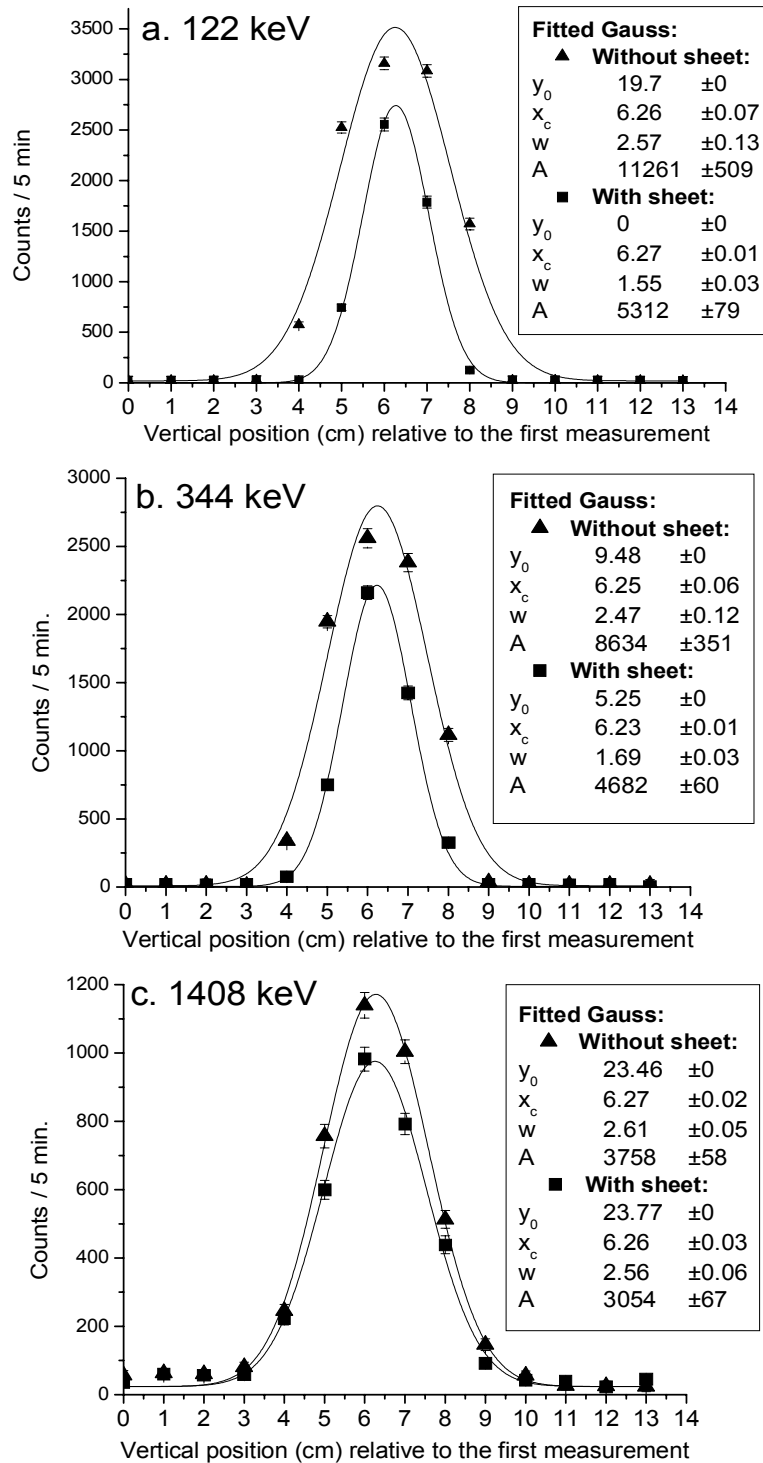


Figure 9 Measured efficiency of a ^{152}Eu point source in a vertical scan, with and without a horizontal lead sheet added in the centre of the collimator opening (see Figure 2), for (a) 122, (b) 344 and (c) 1408 keV.

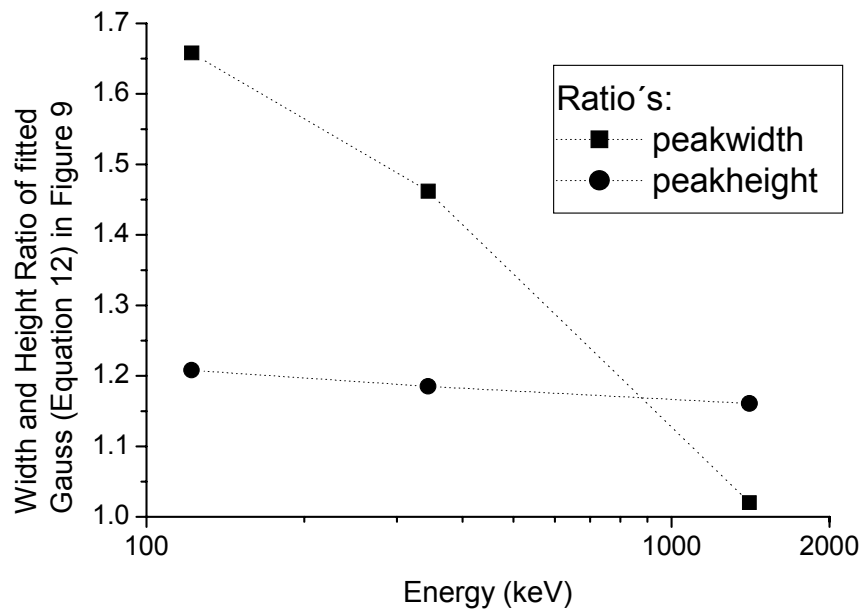


Figure 10 Ratios, without over with sheet, of the detection efficiency of the voxel in front of the detector (i.e. peak height h of the Gaussian in Figure 9 and Equation 12) and vertical resolution (i.e. peak width w), as a function of gamma-ray energy.

5.5 Discussion and conclusions

5.5.1 Choosing the optimum slit size in practice

The results in Figure 4 and 5 and Equation 11 show an optimum of efficiency ratios at a slit size of about 5 cm for the current experimental arrangement. This means that this slit size is the best for detecting activity differences between neighbouring voxels. However, in practice the slit size used will strongly depend on the sample type (radioactivity and energy range of the emitted gammas), and the required spatial resolution in the analysis. The optimum slit opening for such a resolution can be found by FWHM calculations as used for Figure 6.

In another approach, the efficiency ratios as plotted in Figure 5 can be applied to determine which variations in activity distributions can be reconstructed; i.e. how many counts must be gathered in a peak to get a proper signal (activity in the voxel in focus) to noise (sum of activities in the other voxels) ratio. For a ratio of 2.0, the relative contribution of the background for a

homogeneous sample is $\sum_{j \neq i} \varepsilon_{ij} / \sum_j \varepsilon_{ij} = 1/2 / (1/2 + 1) = 33\%$, and for a ratio of 0.1 it is $10 / (10 + 1) = 91\%$. Considering a sample that has a homogeneous activity distribution w_n of element n with an inhomogeneity in voxel i : Δw_{ni} , this causes a change in the collected counts of peak A_j in measurement $j=i$ of ΔA_j . This change can be detected with 99 % reliability if $\Delta A_j \geq 3\sigma = 3\sqrt{\tilde{A}_j}$, where σ is the standard deviation of \tilde{A}_j and \tilde{A}_j is the number of counts collected in measurement i for a homogeneous sample. Now a detection limit can be derived:

$$\frac{\Delta A_j}{A_{ij}} = 3 \frac{\sqrt{\tilde{A}_j}}{A_{ij}} = \frac{3}{\sqrt{A_{ij}}} \sqrt{\frac{\tilde{A}_j}{A_{ij}}},$$

where A_{ij} is the contribution to peak A_j due to gamma's originating from voxel i . Knowing that for $j = i$: $\Delta A_j / A_{ij} = \Delta w_{ni} / w_{ni}$ and for a homogeneously radioactive sample: $A_j / A_{ij} = \sum_j \varepsilon_{ij} / \varepsilon_{ij,j=i}$, this results in a detection limit on the relative size of an inhomogeneity:

$$\frac{\Delta w_{ni}}{w_{ni}} = \frac{3}{\sqrt{A_{ij,j=i}}} \sqrt{\frac{\sum_j \varepsilon_{ij}}{\varepsilon_{ij,j=i}}} = \frac{3}{\sqrt{\eta_{ni,j,j=i} w_{ni}}} \sqrt{\frac{\sum_j \varepsilon_{ij}}{\varepsilon_{ij,j=i}}}, \quad (13)$$

where η_{nij} is defined by $A_{ij} = \eta_{nij} w_{nj} \varepsilon_{ij}$. From Equation 1 it can be derived that

$$\eta_{nij} = \Phi_{th}(\bar{r}_i) \sigma_{n,th} \frac{N_{Av} \vartheta_n}{M_n} (1 - e^{-\lambda_n t_{ir}}) e^{-\lambda_n t_{di}} \frac{1 - e^{-\lambda_n t_{mj}}}{\lambda_n} \gamma_n \quad (14)$$

is independent of j for a homogeneously activated sample and independent of E_γ . Equation 13 depends only on E_γ via the detection efficiencies. Considering that w_{nj} only depends on d via $w_{nj} = d\pi R^2 \rho_n$, where R is the sample radius and ρ_n (g/cm^3) the concentration of element n in the voxel, the almost sample-independent term $\sqrt{(\sum_j \varepsilon_{ij}) / (\sqrt{d} \varepsilon_{ij,j=i})}$ is plotted in Figure 11 for 4 gamma-ray energies as a function of collimator slit sizes between 0.2 and 10 cm. Equation 13 and Figure 11 can be used, given the sample dependent term $\sqrt{(\eta_{nij} d\pi R^2 \rho_n)}$ and the required E_γ , either to determine the slit size given a desired relative detection limit, or to determine the relative detection limit if a certain slit opening or spatial resolution is desired. If the counting time is not at its maximum allowable value, it can be optimised for a desired spatial resolution and relative detection limit.

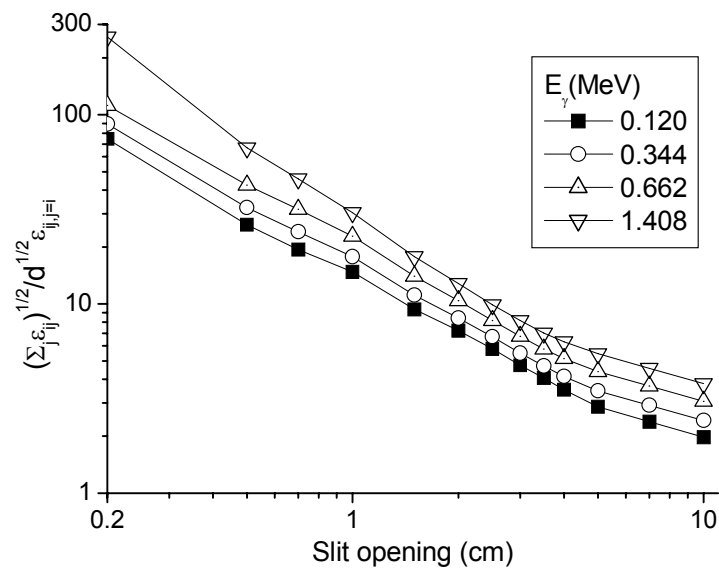


Figure 11 $\sqrt{(\sum_j \epsilon_{ij})} / (\sqrt{d} \epsilon_{ij=i})$ as function of collimator slit opening d for 4 gamma-ray energies. This curve can be used for determination of the relation between spatial resolution or slit opening, sample parameters and detection limits.

The effect of using another collimator opening than the voxel size can now be discussed. A larger opening would yield a higher detection efficiency of the voxel in front of the detector, but also a higher efficiency of the neighbouring voxels and hence a decrease of spatial resolution. From Figure 6 it can be derived that for this gamma-ray energy, the optimum ratio of $\epsilon_{ij}(j = i) / \epsilon_{ij}(j = i+1)$ is found for a collimator opening smaller than the voxel size. Calculations of the cross talk ratio $\epsilon_{ij}(j = i) / \sum_{j \neq i} \epsilon_{ij}$ for 1400 keV, where for some voxel sizes the collimator opening is varied, are presented in Figure 12. Even for this energy the optimum size of the collimator opening for this ratio is smaller than the voxel size. However, a collimator opening smaller than the voxel height will often be unpractical because of the decreased efficiency of the voxel in front of the detector and amplification of effects of inhomogeneities within the voxel on the count rate.

5.5.2 Horizontal resolution

The optimisation was mainly performed for vertical resolution. Resolution within the plane in front of the detector still is poor, even though the layer can be measured in rotational steps. Further optimisation is possible by scanning in the horizontal direction using a collimator in the horizontal direction as well. But this would imply a decrease of detection efficiency of the voxel in front of the detector.

In order to lose less efficiency when increasing the horizontal resolution, the horizontal slit could be filled with a coded aperture, as applied in e.g. astronomical scans for gamma-sources [5]. In that case the opening is filled with a pattern of absorber strips, patterned in such a way that a scan of a layer results in a unique set of spectra for each spatial distribution. A pinhole collimator satisfies this definition, but also some patterns that render a higher detection efficiency. The application of a coded aperture will be discussed in Chapter 10, together with other suggestions for further improvement of the methods.

5.5.3 Application of the sheet in practice

As can be seen from Figures 9 and 10, especially for lower energies (< 1 MeV), the sheet may improve the vertical resolution significantly compared to the loss of detection efficiency of the voxel in front of the detector.

The sheet has not been applied in experiments for REDNAILS yet, since the experimental facility was not suitable for precise positioning of such a sheet. Calculations indicate that with such a sheet the spatial resolution will improve, by

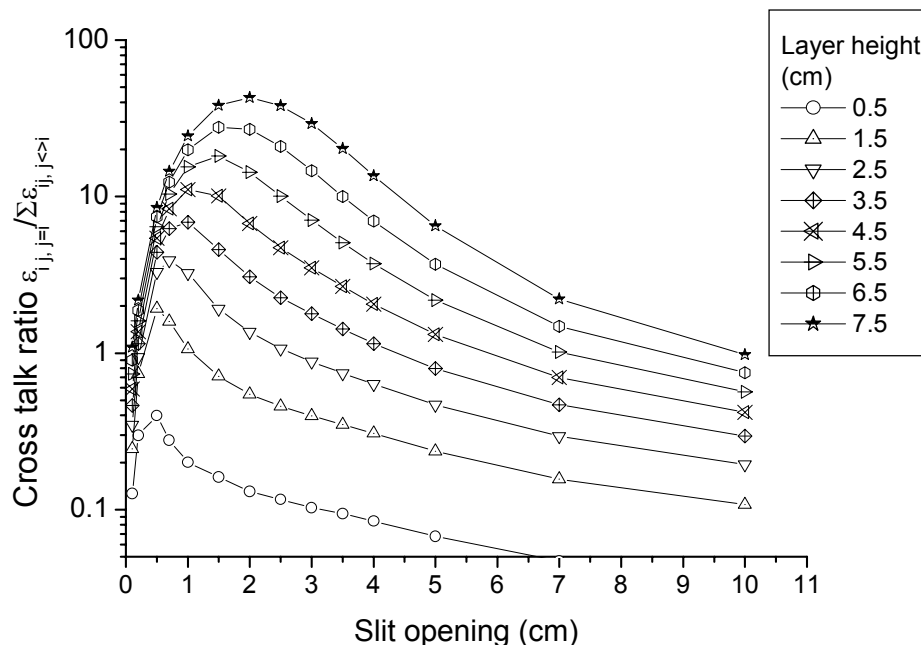


Figure 12 Efficiency ratios for scanned measurements of a source at 25 cm (horizontally) from the detector end cap, calculated for slit size, range 2-100 mm and voxel size, range 5-75 mm, for a gamma-ray energy of 1400 keV.

a factor of 1.2 - 1.7, for gamma-ray energies < 1 MeV.

5.6 References

1. R.H.J. Tanke, J.E. Jaspers, P.A.M. Gaalman, D. Killian, Applications of tomography in nuclear-research, *Kerntechnik*, 56 (1991) 283-289.
2. L. Borms, J. Oeyen, The design of a multipurpose tomography installation, *Nucl. Instr. And Meth. Phys. Res. A*. 422 (1999) 489-492.
3. W. Soller, A new precision X-ray spectrometer, *Phys. Rev.* 24 (1924) 158-167.
4. R.M.W. Overwater, P. Bode, Computer simulations of the effects of inhomogeneities on the accuracy of Large Sample INAA, *Appl. Radiat. Isot.* 49 (1998) 967-976.
5. E. Caroli, J.B. Stephen, G. Di Cocco, L. Natalucci, A. Spizzicino, Coded Aperture Imaging in X- and Gamma-ray Astronomy, *Space Sci. Rev.* 45 (1987) 349-403.

Chapter 6

Detection of Inhomogeneities via Collimated Scanning

6.1 Introduction

In the previous chapter approaches for optimal sample scanning have been described. The scanned spectra gathered this way can be analysed assuming either that the sample is inhomogeneous or that it is not. If the sample is not really inhomogeneous, or at least not for the elements of interest, integral analysis via the method of Overwater [1] is the method of choice. It will give more precise results than averaging after spatial reconstruction, because of intricate covariances between the results of spatial reconstruction. Only if inhomogeneities are detected, reconstruction of the spatial element distribution is mandatory.

Therefore, tools were developed to monitor sample inhomogeneity, to detect occurrence of substantial inhomogeneous element distributions using the already available scanned measurements, and to account for the presence of these inhomogeneities in the analytical results. Once such tools are available, the analytical problem of substantial inhomogeneities can be transformed into an analytical utility: the possibility to get insight in the spatial distribution of trace elements in a large sample.

Tools and methods to be developed are subject to several constraints, which are described in Chapter 3, 4 and 5. The gamma-ray spectroscopy of large, neutron-activated samples is 'routinely' carried out with a collimated detector in the scanning mode as described in the previous chapter, resulting in gamma-ray spectra for three wedge-of-cake shaped voxels per layer of 2 cm, with sizes of about 110 cm³.

6.2 Theory

The observed number of counts in a channel in a gamma-ray spectrum is a stochastic variable, distributed according to the binomial distribution. Usually, the probability of a radionuclide decaying during the measurement and contributing to the channel content is very small so that the Poisson distribution applies [2], often approximated by a normal distribution for expected numbers of counts exceeding 10 or some such number. The standard deviation σ_k of the Poisson-distributed number of counts C_k in channel k is equal to the expected value $E(C_k)$ and is estimated in practice by $s_k = \sqrt{C_k}$. If the measurement is repeated N times, a better estimate is

$$s_k = \sqrt{\bar{C}_k}, \quad (1)$$

with the average channel content over N measurements given by:

$$\bar{C}_k = \frac{\sum_{i=1}^N C_{ik}}{N}. \quad (2)$$

Now a 'z-score' is introduced, being the difference of a channel content from the average divided by its estimated standard deviation. For channel k in measurement i it is defined as:

$$z_{ik} = \frac{C_{ik} - \bar{C}_k}{\sqrt{\bar{C}_k}}. \quad (3)$$

A χ^2 -value can be calculated from the array of z-scores:

$$\chi_r^2 = \frac{\sum_{k=1}^M \sum_{i=1}^N z_{ik}^2}{M(N-1)}. \quad (4)$$

If the sample is homogeneous, the measurements of the different voxels can be considered to be repeated measurements of the same object, and the expected value of χ_r^2 is unity. If the value of χ_r^2 exceeds unity significantly [3], the sample apparently is inhomogeneous. However, because in LS-INAA inhomogeneities of elements rather than of radioactivity have to be monitored, a

correction for the longitudinal neutron flux gradient must be applied [4]. So the corrected values are:

$$C'_{ik} = \frac{\phi_0}{\phi_i} C_{ik}, s_k = \frac{\phi_0}{\phi_i} \sqrt{C_k} \text{ with} \quad (5)$$

$$\bar{C}'_k = \frac{\phi_0}{N} \sum_{i=1}^N \frac{C_{ik}}{\phi_i}, \quad (6)$$

in which ϕ_i is the local thermal neutron flux [$\text{m}^{-2} \text{s}^{-1}$], received by the position in the sample measured in measurement i , relative to ϕ_0 , the thermal neutron flux at an arbitrarily chosen reference point along the height of the sample.

The expected value $E(C_{ik})$ and the corresponding standard deviation σ_k are merely estimated by Equation 5 and 6. These estimates are the best possible, however, in the sense that all available information is used as efficiently as possible and that the estimates are unbiased.

The new z is given by:

$$z'_{ik} = \frac{C'_{ik} - \bar{C}'_k}{\sqrt{\bar{C}'_k}}, \quad (7)$$

Channels k' in which no counts are registered during the scan (*i.e.* $\forall i, C_{k'i} = 0$) are excluded from the z -score array, because their z -scores are not properly defined. This changes the equation for the χ_r^2 to:

$$\chi_r^2 = \frac{\sum_{k=1}^{M'} \sum_{i=1}^N z'^2_{ik}}{M'(N-1)}, \quad (8)$$

where M' is the number of non-zero channels.

The χ_r^2 -test uses χ_r^2 and $M' \times (N-1)$ as input for the standard probability function for a normal distribution which renders a probability that the sample has a (spatially) homogeneous composition, being the probability that for a normally distributed data set (z'_{ik}) with the same number of degrees of freedom ($M' \times (N-1)$) as the current data set, a χ_r^2 is found equal to or larger than the χ_r^2 found for the current data set. The χ_r^2 -test can only be used as an indication since the data are corrected for neutron flux and all channels are considered together.

6.3 Methods

6.3.1 Test criteria

The channel contents of gamma-ray spectra for a scanned sample are converted to the new z-score array (Equation 8), using the vertical flux correction function derived by Overwater [4]:

$$\varphi_i / \varphi_0 = \cos(0.021726 (z_i - z_0)),$$

with φ_i the thermal neutron flux at height z_i [cm] and φ_0 the thermal neutron flux at the reference height z_0 . Only if this z-score array reveals inhomogeneities, a further reconstruction of the spatial element distribution is necessary or meaningful.

The z-score array is judged in three ways: (i) by visual inspection using a coloured plot of the array, (ii) by comparison of the histogram of the z-scores with a histogram of a normal distribution or (iii) by the χ_r^2 -test. Each method has its own features.

The visual inspection allows one to analyse the array as a function of gamma-ray energy and spectrum number. The colour at position (i,k) indicates the value of z_{ik} as explained by the legend of the z-score plots. Small variations of z between -2 and 2 are not of interest, since 95 % of the normally distributed z-scores fall in this range, therefore these values for z have the same colour. It is expected that the clustering of high z-scores may give some information about the position, and the gamma energy of the elemental composition of the inhomogeneities. Also, a single extreme z-score may be observed readily.

The shape of the histogram will change if the sample has inhomogeneous spots, even if they are not extreme enough to be detected in the plot. In that case, the histogram has a positive tail due to high z-scores at positions of higher concentrations of the inhomogeneously distributed element, compensated with a relative large number of small negative z-scores, related to positions where the element concentration is according to the bulk average.

The advantage of the χ_r^2 -test is that only one scalar is obtained that gives information about the probability that the variation in the measurements is not only due to counting statistics, but that the sample contains statistically significant inhomogeneities. The disadvantages are that the χ_r^2 -test can only be used semi-

quantitatively (data are not purely random [3]), smaller, very local inhomogeneities may go unnoticed and no information is provided about position and energy of the radionuclide and its associated element.

6.3.2 spectrum filtering

Besides analysing the 'pure' channel contents of the spectra, it is useful to focus on those channels that contain peaks in the spectra and to disregard the majority of channels that contain only counts from scattered photons. Therefore the spectra are smoothed and filtered using a second order (mid-window) derivative Routti-Prussin filter, that is also applied in the detection of the peaks in gamma-ray spectrum analysis [5]. The width of the window is determined by the width of the peaks. The latter is energy dependent and is determined in a measurement with a calibration source.

This second order derivative will yield minimum, negative values at the position of peaks. These channel contents are only of interest here. Therefore, the (absolute) values of only the negative second order derivatives, $C''_{ik} = \text{Max}(-\frac{d^2}{dk^2} C_{ik}, 0)$, are used instead of C_{ik} in Equations 5-7 for a filtered version of the z-score equivalent array. Although these data points may not be normally distributed, the plot of the z-score equivalent array may give a clear indication of the position of the inhomogeneities and the gamma ray energy of the emitted photons. This smoothing over the peak-width reduces the contribution of the scattered photons to this z-score analysis. Hence inhomogeneities in the peak should be more easily detected this way.

6.3.3 Boundary effects

The spectra measured for the top and bottom layers of an homogeneous sample will contain less counts than the spectra measured in the middle of the sample, due to the fact that these boundary layers have cross-talk radiation from other layers in only one direction. This disturbance of the z-score array can be avoided by disregarding these spectra in the analysis, but in that case no information about inhomogeneities in these layers is gathered. Therefore the analysis can be performed with and without inclusion of the top and bottom layer to see this boundary effect.

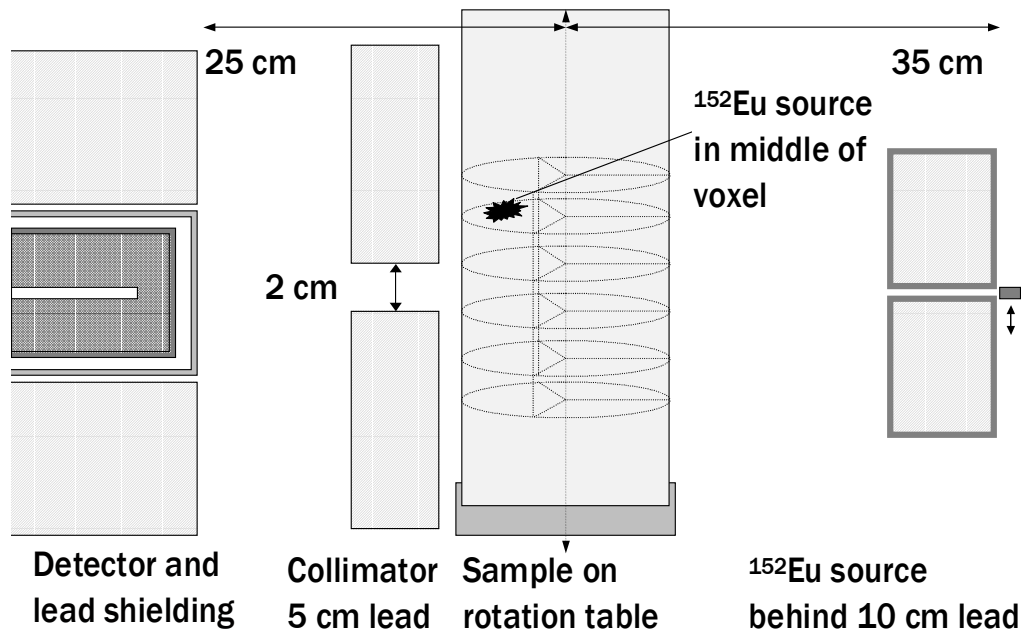


Figure 1 Measurement set-up for Sample 1. The ^{152}Eu source behind 10 cm lead is placed in front of the pinhole only during the scanned measurement of Sample 1 with the homogeneous background.

6.4 Experimental

The irradiation and measurement facilities used are described in Chapter 1 through Chapter 4. Three samples were investigated with the z-score test:

1) A tube of 11-cm inner diameter and 100 cm length, filled with sand, served as a first phantom for the verification experiments. A schematic drawing of the measurement set-up is presented in Figure 1. ^{152}Eu sources were used to simulate induced 'hot-spot' radioactivity at different levels of homogeneously distributed background radiation. The collimator size and hence the spatial resolution (or voxel size) were optimised as described in the previous chapter. A 2-cm opening of the slit collimator was used, which determined the layer height and subdivided each layer in 3 rotational fractions, attaining 150 wedge-of-cake shaped voxels of 63 cm^3 each.

A ^{152}Eu point source of approximately 30 kBq was inserted in the phantom, in the centre of one of the voxels. The gamma-ray spectra were measured in 45 s each while rotating the sample over the 120° 'solid angle' of the voxels to be able

to weigh all 'hot spots' within a voxel equally; yielding 150 measurements, one for each of the 150 voxels. Measurements were performed with and without another ^{152}Eu source in front of the pinhole, thus simulating a hot spot radioactivity at different levels of homogeneously distributed activity. The ratio of the net count rate due to the hot-spot radioactivity, R_{hs} , to the count rate due to the background radioactivity, R_{bg} varied from approximately $(R_{hs+bg} - R_{bg})/R_{bg} = 0.7$ [cps/cps] at 122 keV to 0.18 at 1408 keV.

2) A second sample, a 1 dm³ bottle containing sand and a piece of Zn (3.0 g) in the middle of one of the voxels, was irradiated in the BISNIS facility for 12 h and measured after 4 days in eight layers of 2 cm each, and each layer in three rotational steps, using the same collimator as in the first experiment and taking 3 minutes per measurement.

3) A sample of a 1 dm³ bottle filled with shredded plastic material used in the recycling industry, originally irradiated for 12 h and analysed after 3 days waiting time as a normal large sample. After the first integral activity measurement [6], it was also measured in scanning steps, similarly to Sample 2, and checked for inhomogeneities using the z-score test.

6.5 Results

6.5.1 Sample 1: ^{152}Eu trace hot spot

High-contrast, in otherwise homogeneous sample:

The plot of the z-score array in Figure 2 clearly shows some clustered spectra with extreme z-scores. The fact that this is a region at a certain height and not randomly distributed points, indicates distinct inhomogeneity in the radioactivity of the sample. The channels corresponding with the gamma energies of the photons emitted by the point source show the highest z-scores for the spectra around the layer containing the source; channels of these spectra in the lower energy region have high z-scores due to Compton scattering. The χ_r^2 -test renders: $\chi_r^2 = 1.76$ for $M'(N-1) = 151,384$ degrees of freedom (*i.e.* $M' = 1016$ nonzero channels $\times N-1 = 149$). The probability that $\chi_r^2 > 1.76$ for 151,384 degrees of freedom, $P(1.76 | n = 151,384) \ll 1E-300$, according to [3]. This means that the

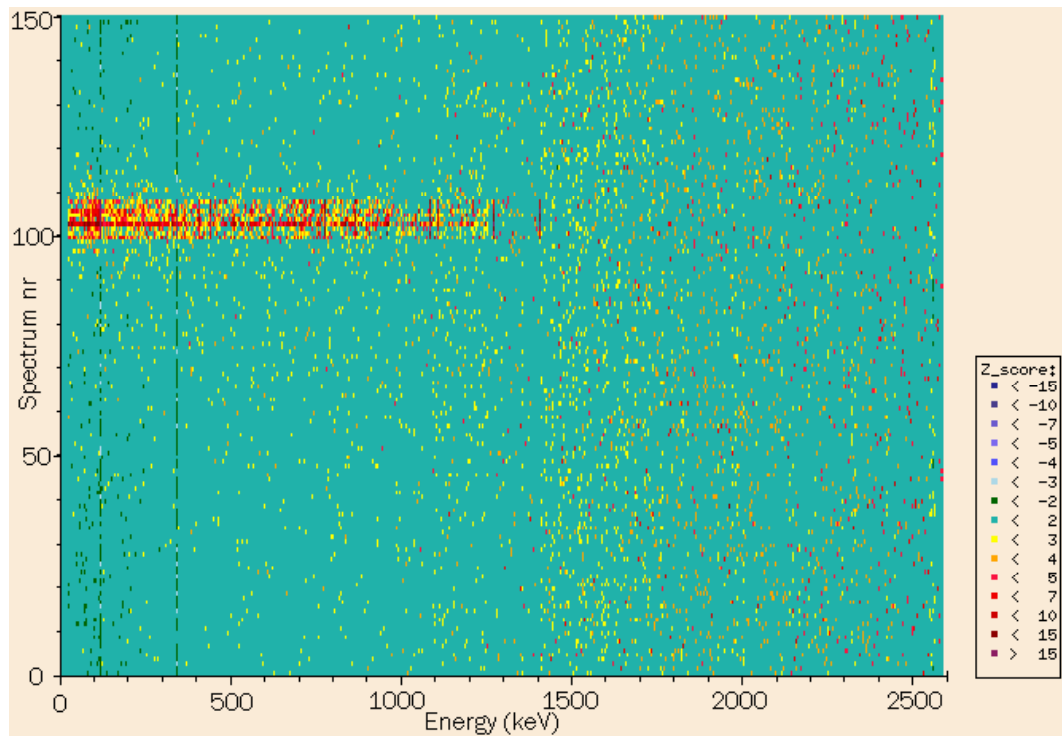


Figure 2 Plot of the z-score array of the raw channel contents for the spectra of Sample 1 with high contrast. Each row contains a single spectrum and each column corresponds to a gamma energy. The legend explains the range of equally coloured z-scores, e.g. all z-scores between 2 and 3 are yellow.

sample is definitely not homogeneous. From the plot of the z-score array (Figure 2) some important gamma-ray energies of ^{152}Eu (122, 344 and 1408 keV) can be identified and the central position of the source can be estimated to be in voxel 103. The layer number, 55, can be derived from the spectrum number, being the integer of that number divided by the number of spectra per layer, i.e. 3.

Low-contrast, in otherwise homogeneous sample

The z-score plot in Figure 3 still shows height and energy clustered extremities indicating inhomogeneities, though it is more difficult to see than in Figure 2.

The χ_r^2 -test gives now lower values: $\chi_r^2 = 1.12$ for 151,384 degrees of freedom. The probability that for a homogeneous sample a larger χ_r^2 is found is given by $P(1.12 \mid n = 151,384) = 6\text{E-}222$. This is still a clear indication that the sample is inhomogeneous.

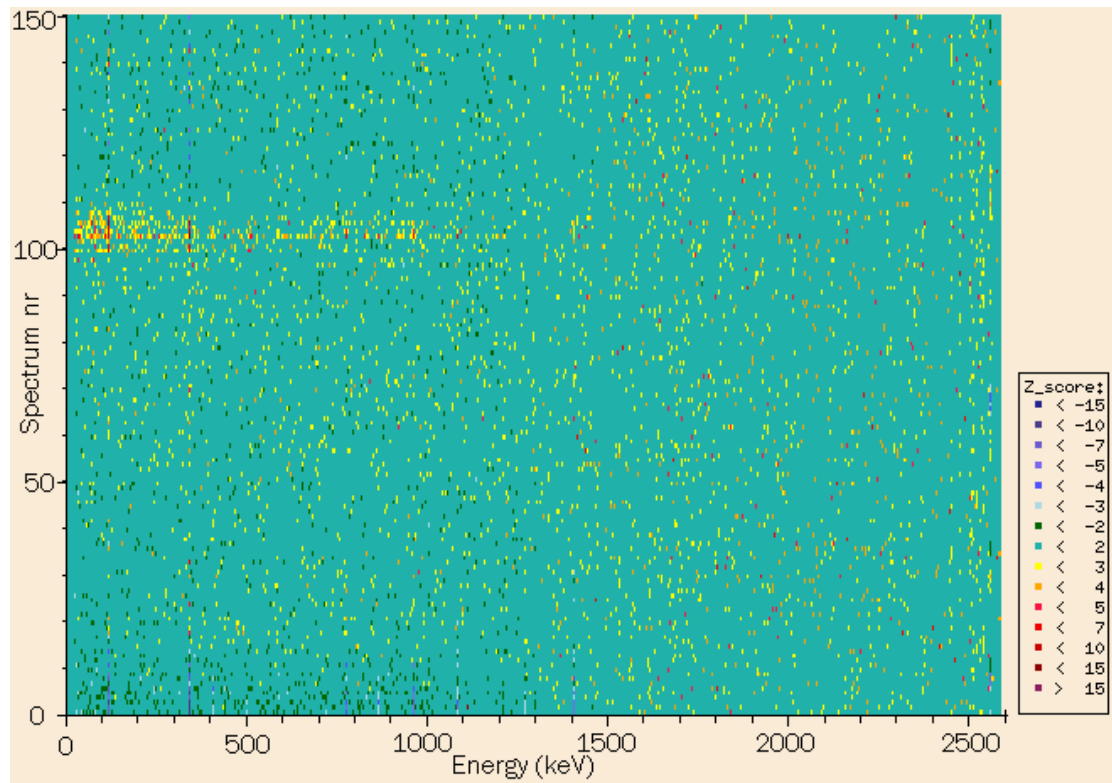


Figure 3 Plot of the z-score array of the raw channel contents for sample 1 with fixed background radiation, i.e. low contrast.

6.5.2 Sample 2: Zn in sand, activated phantom

The z-score plot in Figure 4 reveals the inhomogeneity for Zn at the $E_\gamma = 438$ keV and 1115 keV gamma-ray energy lines by high z-scores in the neighbourhood of spectrum 15. Other elements that are dominantly present in the spectrum of Figure 4, like Na (^{24}Na , $E_\gamma = 1368$ keV) give no deviating z-scores. This proves that the z-score test really stresses inhomogeneities above a certain threshold and suppresses changes in count rate due to statistical variation in counting.

The χ_r^2 -test renders $\chi_r^2 = 1.53$ for 23,368 degrees of freedom. Since $P(1.53 \mid n = 23,368) \ll 1\text{E-}300$, once again this test indicates that the sample is inhomogeneous.

Figure 5 shows the histogram of the z-score of the 'raw' channel contents, compared to a normal distribution. The change of shape of the histogram is in accordance with the expected change of shape for inhomogeneous samples:

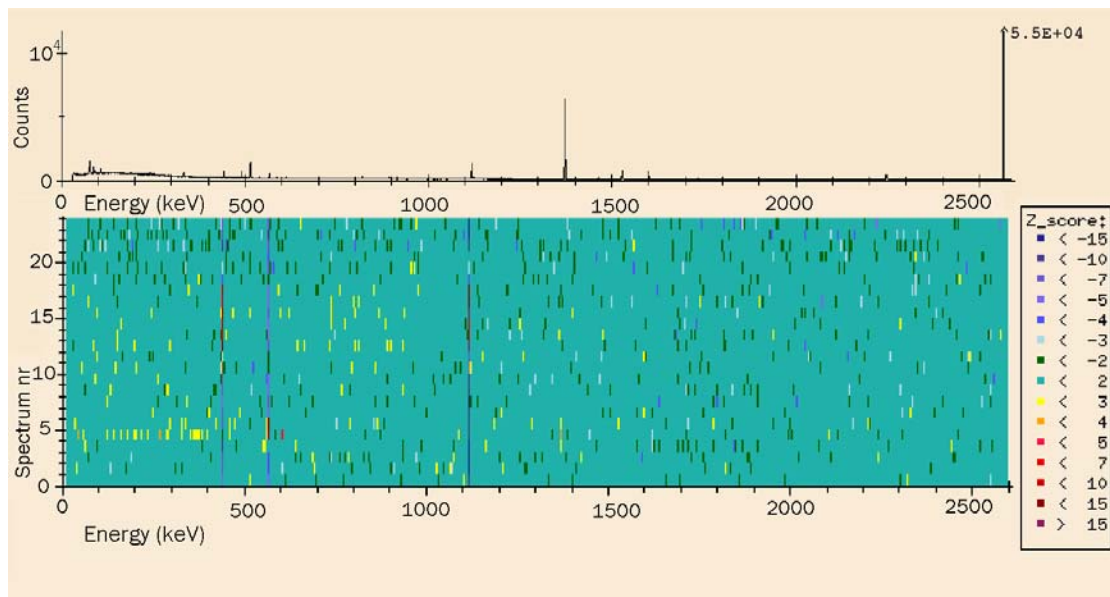


Figure 4 Parallel plot of the sum-spectrum of the scanning measurement and the z-score array of the raw channel contents of sample 2, with the same gamma-ray energy scale on both x-axes.

though the effect is only small, the histogram shows tailing in the positive z direction.

6.5.3 Sample 3: Plastic shredder sample

In this case the inhomogeneity of the sample was not a priori known. Therefore all three inhomogeneity tests were performed and for the plot of the z-scores array not only the raw channel contents were used but also the filtered data.

Figure 6 shows the z-score arrays of the raw and filtered data. The χ_r^2 -test for these arrays renders: $\chi_r^2 = 26.4$ for 24,528 degrees of freedom. In this case the plot, Figure 6, and the χ_r^2 -test both indicate that the sample is inhomogeneous. The high z-scores are found in the middle of the sample at the gamma-ray energy positions of ^{82}Br : 554, 776, 1044, 1317 and 1475 keV.

Figure 7 shows the z-score arrays of these data when the bottom and top layer are excluded from the analysis. The χ_r^2 -test for these arrays renders: $\chi_r^2 = 13.0$ for 17,374 degrees of freedom. So again, the conclusion can be drawn that this sample contains inhomogeneities.

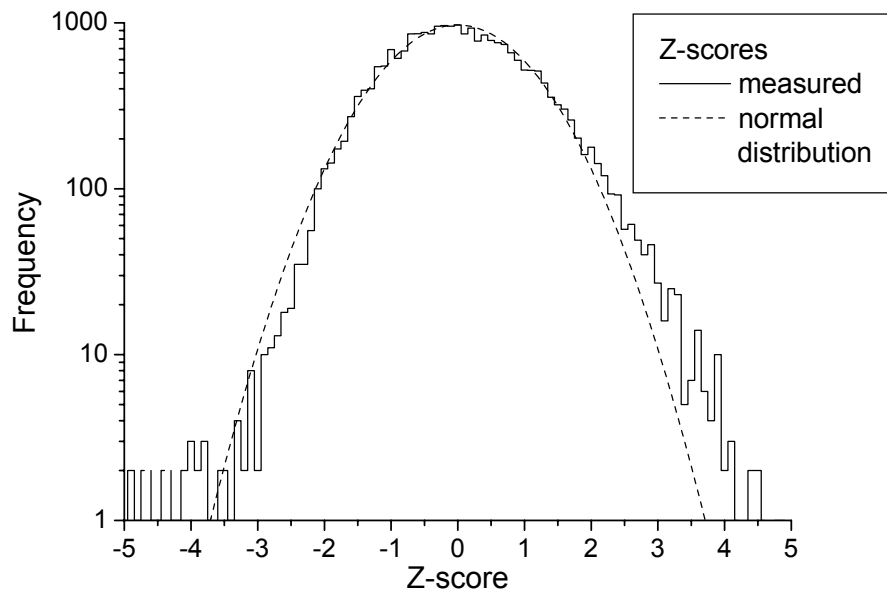


Figure 5 Histogram of z-scores for Sample 2, showing a small right tail

Finally, the histograms of the z-score arrays, presented in Figure 8a indicate likewise. The change in the shape of the histogram –the right tailing is more than the left tailing– is now more clearly as predicted in Paragraph 6.3.1. The effect of omission of the top and bottom layer is demonstrated in Figure 8b: the histogram is more comparable to a normal distribution now.

All tests show that this sample has an rather inhomogeneous distribution, at least for the element Br, that seems to be concentrated in the layers related to spectra 10-15, according to Figure 7.

6.6 Discussion and conclusions

The techniques presented in this chapter were designed for a quick 3-dimensional screening for substantial inhomogeneities. The robustness of the

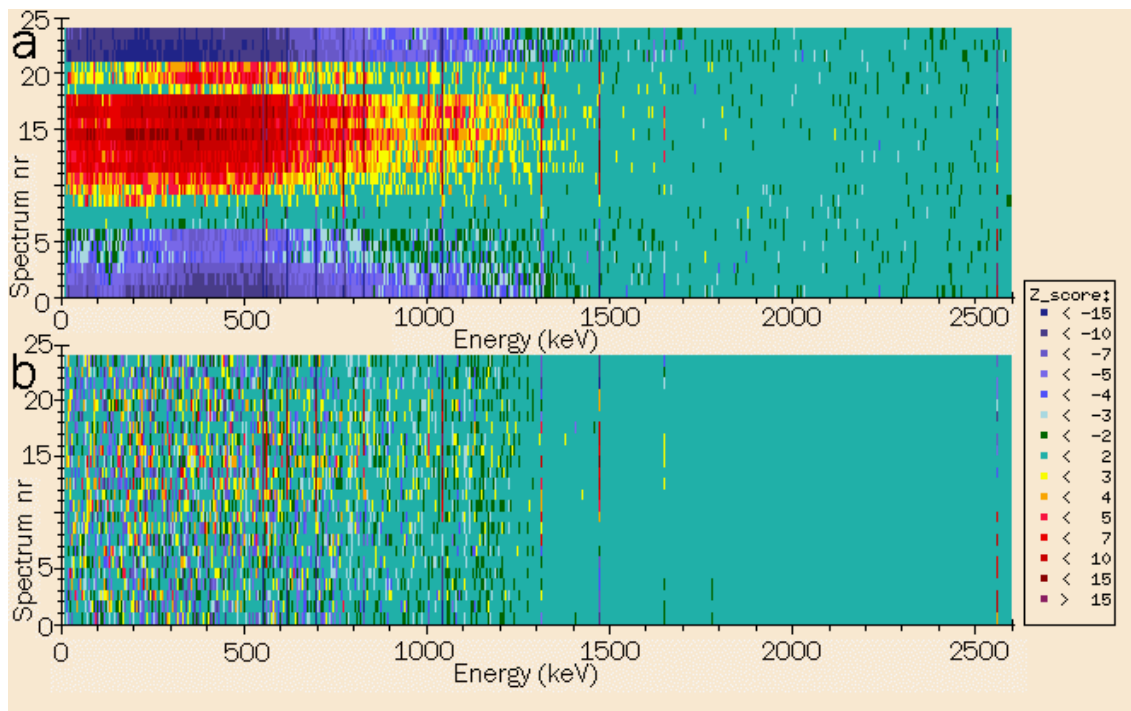


Figure 6 Plot of z-score array of (a) the ‘raw’ channel contents for Sample 3, and (b) of the (2nd order derivative) filtered channel contents for Sample 3.

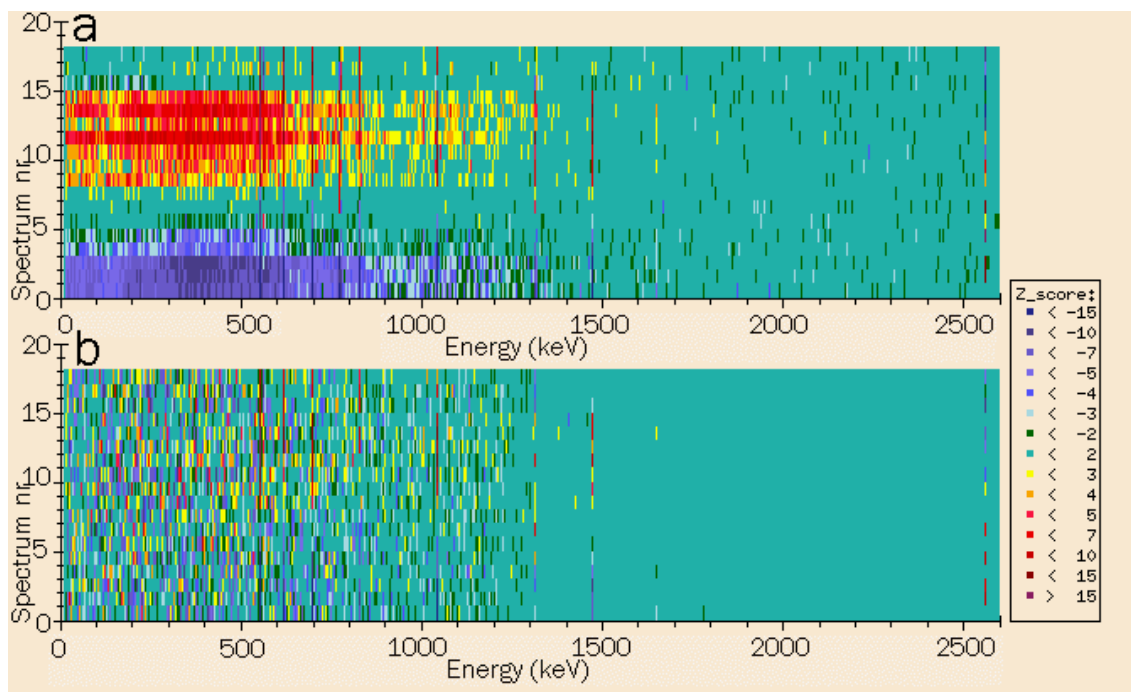


Figure 7 Plot of z-score array -skipping top and bottom layer- of (a) the ‘raw’ channel contents for Sample 3, and (b) of the (2nd order derivative) filtered channel contents for Sample 3

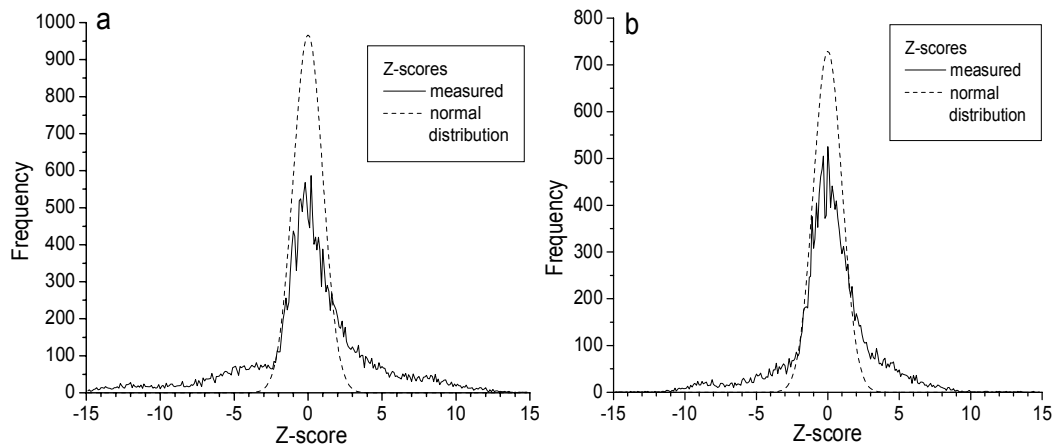


Figure 8 Histogram of z-scores for Sample 3 (a) of all spectra and (b) of the spectra minus those of top and bottom layer

techniques has been demonstrated with a couple of samples. Three ways of testing a set of spectra of a scanned sample on inhomogeneities were considered. Each approach has its own advantages and disadvantages:

The χ_r^2 -test may give a good indication in case of a sample with inhomogeneities close to the detection limit. The idea of one scalar as a basis for the classification of the sample on a (in)homogeneity scale is charming, but not practical considering the samples studied here: if the sample is inhomogeneous then the information from a single scalar is limited, since it does not provide any information about origin or energy of the emitted gammas. The χ_r^2 -test does not provide a better criterion than a visual check of the spectra for a go/no go decision towards analysis of the scanning data as spatially homogeneous data or not. Besides, the result is of limited value since not all criteria for the normal distribution are met [3].

For a scan with low channel contents in most spectra, the best indicator is the colour plot of the z-score array. For spectra containing a higher homogeneously distributed radioactivity, the z-score test still provides a monitor for extreme inhomogeneities, especially when the second order filter is used. The filtered data show clustered higher z-scores related to peaks rather than Compton scattered photons. The visual check of the plot also allows for estimation of position and element composition of the inhomogeneity. This test does not provide a quantitative measure of inhomogeneity, though.

The plot of the histogram of z-scores gives little more information than the χ_r^2 -test. It does not seem to give additional information either to the visual check of the z-score plot. But for more complex samples, where nothing can be seen clearly from the plot although the χ_r^2 -test points to an inhomogeneity, the histogram may give an explanation for the χ_r^2 found. Although the histogram provides more detailed statistical information than the z-score plot, one should keep in mind that information about position and energy is lost.

Figure 7 demonstrates that disregarding top and bottom layers may improve the analysis: systematically deviating data points are skipped. If one bears these systematic errors in mind then these layers may be included in the plot of the z-score array.

In general, the combination of the three tests gives the analyst useful tools to take the decision, whether the sample should be analysed as homogeneous or not.

If extreme inhomogeneities are observed, a more detailed picture can be reconstructed by scanning a small fraction of the sample around the inhomogeneity with a smaller collimator opening and using a longer counting time per measurement.

This homogeneity test is restricted to detection of inhomogeneities that have impact on the sample measurement statistics. *E.g.* radially symmetric inhomogeneities cannot be detected this way, even though they may affect the accuracy of the measurement result as mentioned already by Overwater[1].

6.7 References

1. R.M.W. Overwater, P. Bode, *Appl. Radiat. Isot.* **49** (1998) 967-976.
2. G.F. Knoll, *Radiation detection and measurement*, 2nd edition (1989), John Wiley & Sons Inc., New York.
3. J.S. Bendat, A.G. Piersol, *Random data: Analysis and measurement procedures*, (1971), John Wiley & Sons Inc., New York.
4. P. Bode, R.M.W. Overwater, J.J.M. De Goeij, *J. Rad. Nucl. Chem.* **216** (1997) 5-11.
5. M. Blaauw, *Nucl. Instr. Meth. A* **336** (1993) 273-277.
6. C. Renders, Graduation thesis, IRI/Fontys internal report (2000).

Chapter 7

Gamma-ray attenuation assessment

7.1 Introduction

As illustrated Equation 5 in Chapter 3, the main equation for REDNAILS, the peak areas for a given distribution of radionuclide associated with a particular element in the sample can only be predicted and interpreted if the gamma-ray detection efficiency is known. For proper gamma ray detection efficiency calculations, the attenuation of the gamma rays on their way out of the sample should be determined. Since the sample is assumed to be inhomogeneous for the element-concentrations, it may also be inhomogeneous for gamma-ray transmission as well.

Therefore, a method is developed to determine the gamma-ray transmission characteristics for all voxels separately. This method is an extension of the method developed by Overwater for determination of the average gamma-ray attenuation within the sample [1].

7.2 Theory

It is assumed that the attenuation of the gamma rays in each voxel separately may be described by a linear attenuation coefficient. The linear attenuation of the photons $\mu(E_\gamma)$ [m^{-1}] can be calculated for each E_γ from transmission measurements using the equation:

$$\mu(E_\gamma) = \frac{1}{d} \ln\left(\frac{I_0(E_\gamma)}{I(E_\gamma)}\right) \quad (1)$$

where d is the path length of the gamma rays through the sample [m], I_0 is the intensity of the beam for gammas with energy E_γ at the detector position in the absence of the sample [s^{-1}] and I the intensity at the same position in the presence of the sample [s^{-1}].

Overwater has applied Equation 1 in his method for determination of the spatial averaged gamma-ray attenuation in large samples, using a mixed-energy gamma-ray beam, originating from a $^{152}\text{Eu}/^{154}\text{Eu}$ source, and measuring the gamma-ray spectrum with and without rotating sample between source and detector. For determination of the gamma-ray attenuation for all gamma-ray energies in the range of interest, a cubic spline was fitted to the measured attenuations.

In the experiments for REDNAILS, the attenuation has to be measured for each voxel separately. As a consequence, to keep the total measurement time between reasonable limits for samples up to 150 voxels, the time per measurement has to be limited. This will result in spectra with relatively more statistical fluctuation. To stabilise the fitting outcome for the attenuation curves, it is assumed that for the gamma-ray energy range of interest, the attenuation coefficient can be described by the photo absorption effect above the K-edge and Compton scattering only. The attenuation as a function of gamma ray energy is fitted using the empirical model:

$$\mu(E_\gamma) = G_1 e^{-E_\gamma/E_1} + G_2 e^{-E_\gamma/E_2}, \quad (2)$$

where $E_1=0.15$ MeV and $E_2=2.3$ MeV are experimentally fitted coefficients. This model is based on the assumption that for most samples the largest atomic number of matrix elements will be less than 90 so that K-absorption edges do not appear above 100 keV, where all the photon energies of interest for INAA are observed. Variation of the ratio of photo-electric absorption to Compton scattering are described by G_1 and G_2 .

Figure 1 shows the attenuation coefficient of SiO_2 (as a model of sand) calculated with XCOM [2]. For the range 0.1 – 3 MeV, the attenuation can be approximated by Equation 2.

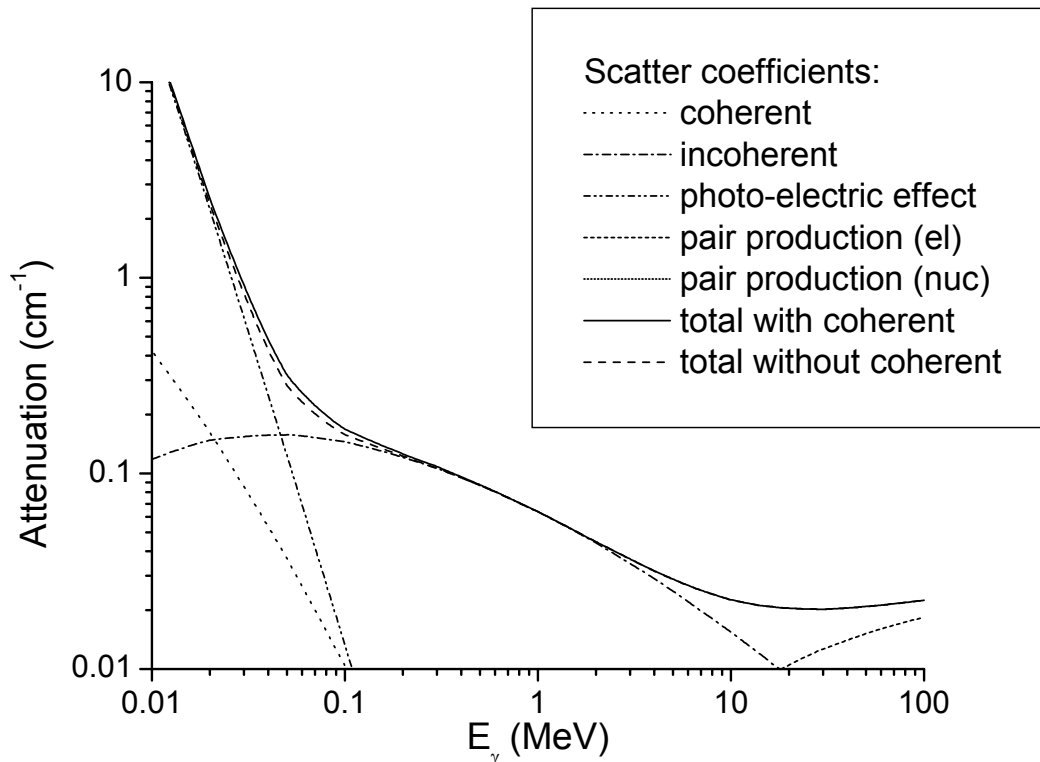


Figure 1 Energy dependent gamma ray attenuation coefficient for SiO_2 , calculated with XCOM[2].

7.3 Methods and experimental

As in Overwater's method, first the reference, the gamma-ray spectrum of the transmission source is measured without the sample. Next, the gamma ray spectrum is measured with the sample on the rotation table. But whereas in Overwater's method, the photon beam was directed at the centre of mass of the sample, now the sample is horizontally translated, creating an offset of half the radius from the transmission beam axis. The voxel to be scanned is vertically in front of the detector but horizontally 90° rotated, so that the transmission beam has its only path through the sample over on average $\sqrt{3} \times \text{Radius}$ in the voxel of interest, see Figure 2. The path through the sample has a range due to the transmission beam radius R_{in} at the entrance of the sample and R_{out} at the exit of the sample of $\sqrt{3} \times \text{Radius} \pm \frac{1}{2} \sqrt{3} (R_{in} + R_{out})$. But if Equation 1 is approached by only a first order Taylor expansion:

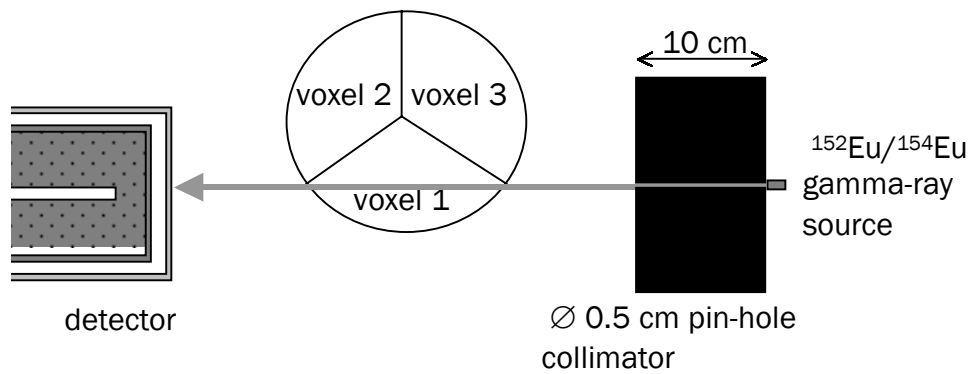


Figure 2 Schematic drawing, top view, of the measurement set up during the gamma ray attenuation measurement of a single voxel

$$\frac{I}{I_0} = e^{-\mu d} = 1 - \mu d, \quad (3)$$

which is valid for only small μd , then the average length of the path through the sample can be applied in solving Equation 1.

The reference might be measured only once and then applied to multiple scanned samples, since it is sample independent. This measurement may take 30 up to 60 minutes and the fitting result of its spectrum is checked visually.

On the other hand, the scanned measurements take typically 5 minutes per voxel and the fitting is fully automated, where peak positions are determined on basis of the peak positions in either the sum spectrum or the reference spectrum.

As can be seen from Figure 2, this method for measurement of the attenuation has an more ideal path through the voxel for three than for more radial voxels per layer.

The next step, the fitting of Equation 2, is performed for all voxels separately. To save time, the experimenter checks the quality of the fit only through χ^2 and variation in the parameters G_1 and G_2 .

The gamma-ray source used for the attenuation measurements is a $^{152}\text{Eu} + ^{154}\text{Eu}$ transmission source behind a 10 cm thick pinhole collimator. The spectra are fitted as described in Chapter 3. Now in the spectrum fitting special consideration is taken for the 122 keV doublet, since it is known on beforehand that both peaks are present in the spectrum of these radionuclides.

For validation of theory and methods the gamma ray attenuation was determined in three different samples: dried and homogenised harbour sediment, milk powder for three voxels per sample and ditch bottom sample for one voxel per sample.

7.4 Results and discussion

Figure 3 shows the measured and fitted attenuation of harbour sediment and milk powder. The Figure demonstrates that the approach of fitting G_1 and G_2 from Equation 2 for each voxel works well. The interpolation via this model is more realistic than interpolation via an unphysical cubic spline. Also extrapolation of the attenuation for $E_\gamma > 1408$ keV is more stable.

A large χ^2 is found in two cases, where linear attenuation for the 779 keV peak is lowest. In general, the linear attenuation measured at 778 keV seems systematically lower than the fitted value.

Figure 4 shows the measured and fitted attenuation for the ditch bottom sample. The line presents the calculated attenuation for low Z materials with density 1.33 g/cm^3 .

7.5 Conclusions

The results show that the presented method for determination of the gamma-ray attenuation works well. It renders more stable curves for interpolation and extrapolation of the attenuation for gamma-ray energies besides the energies present in the Eu source than the cubic-spline method developed by Overwater. The third sample shows that the attenuation coefficients agree well with known values, and even allow us to determine the specific mass of the voxel.

The method aims at a simple determination of the average linear gamma-ray attenuation coefficient per voxel in a large sample. It uses an maximum path through each voxel, to smoothen in-voxel inhomogeneities. However, extreme inhomogeneities outside this path may still corrupt the measurement.

The method has been designed for practicable multivoxel analysis, to minimise user interaction and checks. The user still has to look over the attenuation plots and the χ^2 to check whether the fit could be performed correctly.

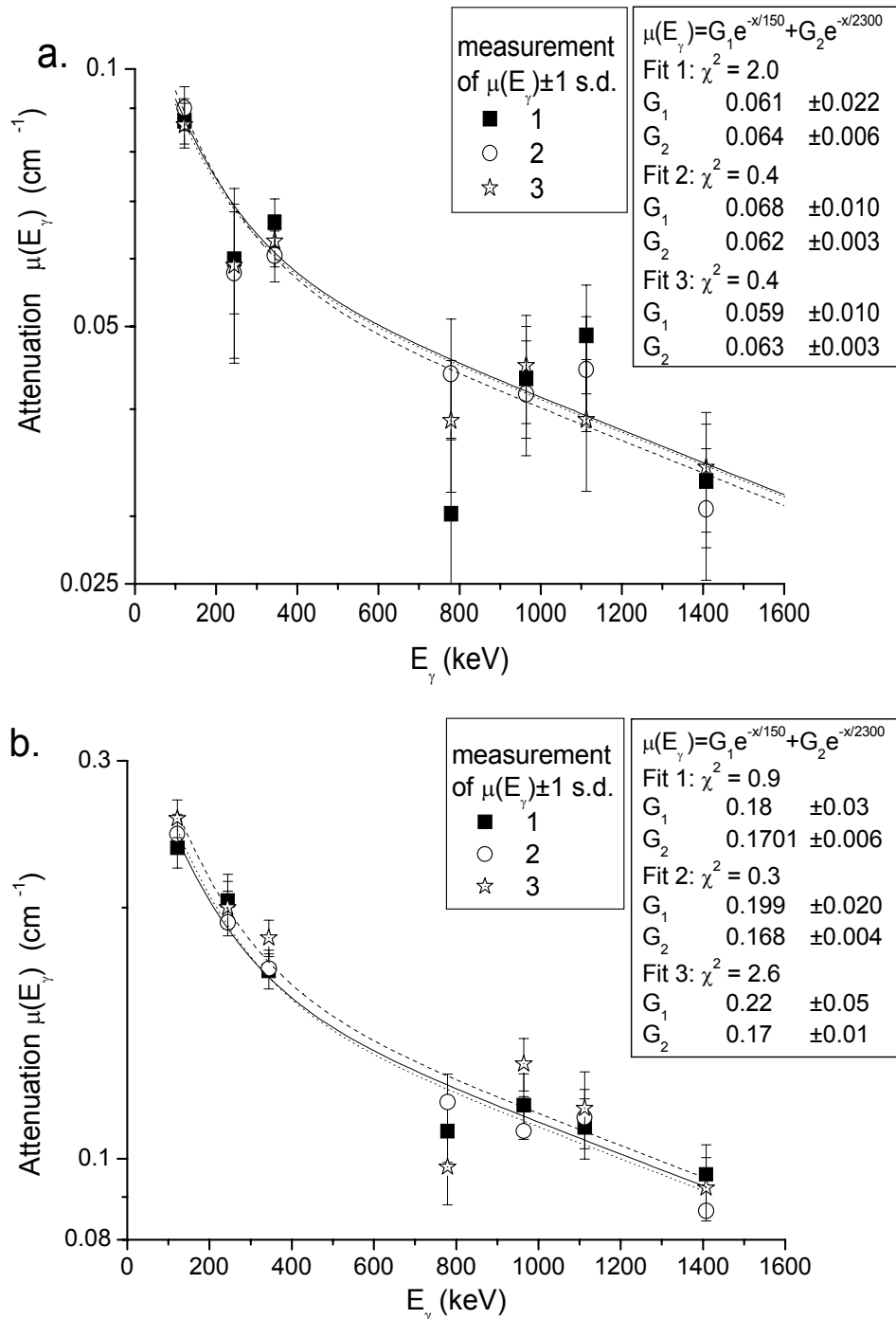


Figure 3 Linear attenuation coefficient of gamma rays, measured and fitted for (a) milk powder and (b) dried harbour sediment. The fitted data represented by the curves are quite stable (or reproducible) compared to the scatter in the measured attenuation coefficients.

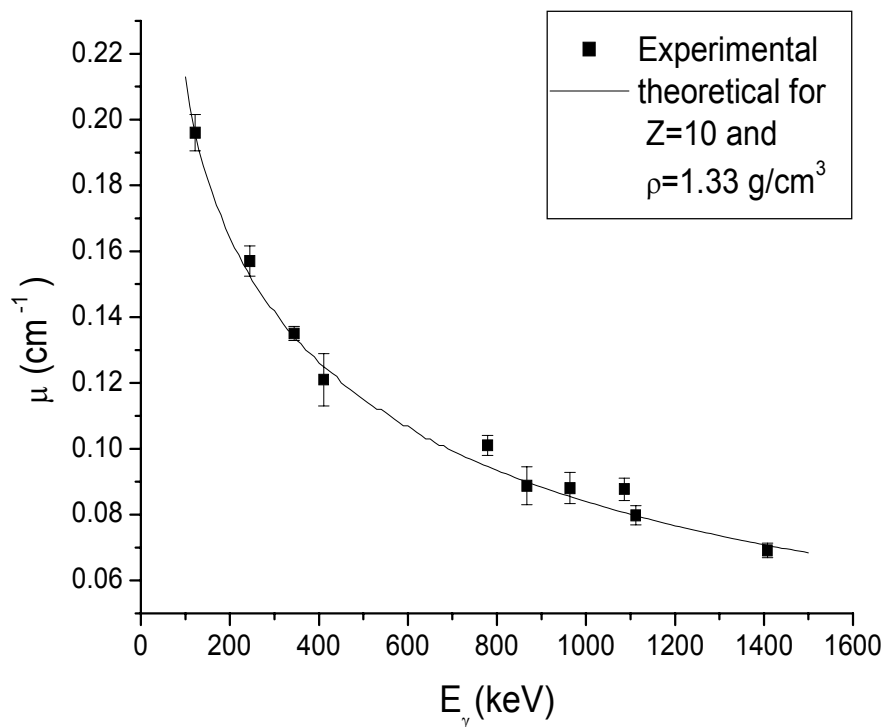


Figure 4 Results for the gamma ray attenuation of the ditch bottom sample. For comparison the linear attenuation coefficient for low Z samples with density $\rho=1.33 \text{ g/cm}^3$, calculated with XCOM[2], is plotted as well.

Outliers may be caused by errors in peak fitting of the gamma spectrum or samples of exotic composition.

7.6 References

1. R.M.W. Overwater, The physics of Big Sample Instrumental Neutron Activation Analysis, thesis, Delft 1994
2. M.J. Berger, J.H. Hubbell, H.D. Lemmel, XCOM: Photon cross-sections on a PC. Version 1.2 of 9 May 1987, International Atomic Energy Agency, Vienna (Austria). Nuclear Data Section.

Chapter 8

Reconstruction Algorithms for Analysis of Element Distributions in Neutron-Activated Inhomogeneous Large Samples

8.1 Introduction

A sample that has been treated according to the description in the previous chapters will have at this stage the following results: (i) As given in Chapter 3, its background radiation has been measured in scan mode, (ii) as described in Chapter 7, for each voxel a transmission measurement has been performed, as presented in Chapter 3, the sample has been irradiated in the BISNIS facility, surrounded by flux monitors, (iii) after irradiation the neutron-flux distribution in the sample has been determined on basis of the spectrometry of the flux monitors, (iv) next, after a certain decay time, the activated sample has been measured in scan mode, using the optimised measurement set up, as described in Chapter 5. These spectra have been used to detect inhomogeneities, as described in Chapter 6.

If the sample is inhomogeneous indeed, the matrix of equations, described by Equation 4 in Chapter 3 must be solved to determine the distribution of the elements in the sample. Figure 1 in Chapter 3 shows how all measurements are connected to build this matrix. In this chapter, the measurements are all fit into the matrix and algorithms to solve the matrix are described. Results of these reconstruction methods are presented and discussed for some modelled samples.

8.2 Theory and methods

8.2.1 Predicted spectra-array generation

The set of equations to be solved was already presented in Section 3.6.4:

$$\mathbf{A} = \mathbf{K}\mathbf{w}, \quad (1)$$

where A_{jl} is the observed peak area at energy l in spectrum j , K_{ijnl} is the expected peak area at energy l in spectrum j due to voxel i consisting of 1 g of element n [g^{-1}], and w_{in} is the amount of element n present in voxel i [g].

The value of the matrix elements K_{ijnl} is calculated with

$$K_{ijnl} = \int_{\text{voxel } \text{Vol}_i} \Phi_{th}(\vec{r}_i) \sigma_{th,n} \frac{N_{Av} \vartheta_n}{M_n} (1 - e^{-\lambda_n t_{ir}}) e^{-\lambda_n t_{d,j}} \frac{1 - e^{-\lambda_n t_{m,j}}}{\lambda_n} \gamma_{nl} \varepsilon_{jl}(\vec{r}_i) d\vec{r}_i, \quad (2)$$

The element and nuclide constants specific parameters $\sigma_{th,n}$, λ_n , γ_n , θ_n and M_n (see Section 3.2) are read from the INAA software library. The decay correction is determined using the times written in the sample database. The only terms that are spatially variant, $\Phi_{th}(r)$ and $\varepsilon(r)$, are merged together to determine a gamma-neutron correction factor for each gamma-ray energy and each voxel in each measurement. The relative position of the voxel in the given measurement is determined. The voxel is subdivided in a subset of 75 equal-sized subvoxels. The neutron flux relative to the BISNIS standard neutron flux in the sample is determined, using Overwater's neutron sample self-shielding correction factors for LS-INAA [1]. These correction factors are based on the measured fluxes at the positions of the flux monitors in the presence and absence of the sample. The front end of the detector crystal is subdivided in 125 equal-sized parts, as described in the detection efficiency calculations in Chapter 4. The path from the centre of the subvoxel to the centre of the part of the detector, see Figure 1, is analysed, to determine its total length and the respective lengths through attenuating materials. The path length through the voxels it crosses is determined, with their respective attenuation, as determined according to the methods described in Chapter 7. Also, the path length through the collimator and detector end cap is calculated, with their tabulated attenuations. Finally the path length

through the detector is calculated to determine the efficiency of detection according to the methods described in Chapter 4.

In order to minimise the calculation time, the following procedure is applied: First the net peak areas are predicted for the measurements of each voxel in front of the collimator opening ($i=j$), for each element, assuming that the voxel consists of 100% of that element. Next, assuming that the observed peak areas are due to this voxel only, upper limits for the elemental amounts in each voxel are calculated or else, when no peak was detected at the predicted energy, detection limits are calculated, taking the continuum in the measured spectrum into account. Then, predicted peaks that could not have contributed significantly to the observed peaks, in view of the elemental upper limits, are removed from the lists of predicted peak areas. These 'cleaned' peak lists for measurements of each voxel in front of the collimator opening are merged to obtain a list of all relevant predicted peaks. Finally, the peak areas for the lists of predicted peaks are (re)calculated for all i and j and removed afterwards if they are not present in the previously calculated merged list of relevant peaks. At this point, all predicted spectra contain the same peaks. The predicted spectra are stored in the matrix \mathbf{K} .

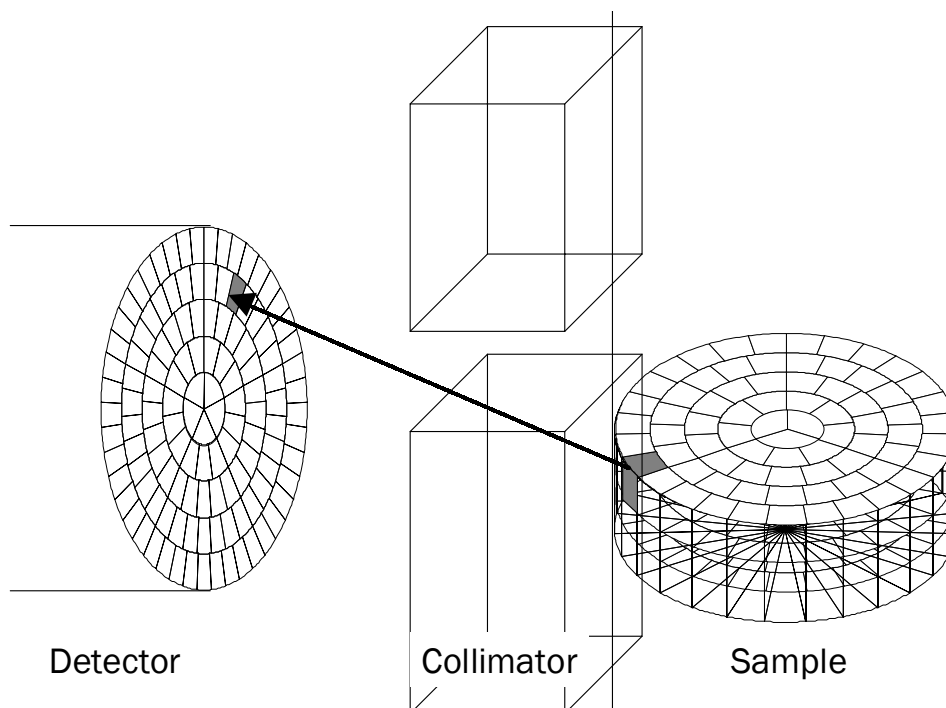


Figure 1 Schematic representation of path from subvoxel to segment of the detector.

Before starting the reconstruction, the matrix is reduced by dividing it in independent sets of elements, *i.e.* sets of elements that do not have any predicted or observed peak energy in common.

8.2.2 Reconstruction algorithms

The reconstruction procedure in holistic NAA, based on an array of predicted spectra, still can be applied, though extended in two dimensions: the number of measurements performed in one scan and the number of voxels.

In the holistic interpretation as implemented by Blaauw, the best fit is found by a linear least-squares solution [2]. For scanned measurements the solution of this algorithm becomes unstable, because the predicted spectra for the same element in neighbouring voxels - especially in the same layer - are strongly correlated. As an example a best fit may turn out to be an alternating pattern of positive and negative concentrations of the same element in neighbouring voxels (ringing effect). One way to circumvent this problem is adjusting the algorithm for non-negative results [3] or applying iterative algorithms as used in tomography. In this study, two algorithms are examined: The Maximum Likelihood method with Expectation Maximisation (MLEM) [4,5,6] and the Conjugate Gradient method with Non-Negativity constraint (CGNN) [6]. In the following paragraphs, the theoretical descriptions are mainly based on the descriptions of Chang *et al.* [6]. The k and l indices, denoting element and peak energy, are omitted in the following for clarity's sake.

8.2.3 MLEM

The maximum likelihood method itself is a basic method, used to determine statistical values in a data set, like expectation value or variation, given a distinct statistical distribution [7]. It selects the most likely solution to an unknown parameter, given measured parameters and a likelihood distribution that describes the relationship between measured and unknown parameters. Applying of the maximum likelihood technique to REDNAILS, the voxel concentrations w_i (for all voxels i) are determined that maximise the probability of having obtained the detector responses, peak areas, A_j (for all measurements j).

It is assumed that the number of counts in a peak area is Poisson-distributed

$$P(A_j) = \frac{\bar{A}_j^{A_j} e^{-\bar{A}_j}}{A_j!} \quad (3)$$

where \bar{A}_j is the expected number of counts in the peak, equal to the mean number observed in an infinite number of trials. The expected number of counts is given by

$$\bar{A}_j = \sum_i K_{ij} w_i \quad (4)$$

where K_{ij} is the number of counts expected in measurement j if the voxel i consists of 100% of the specific element and other voxels are empty.

The probability of having observed all A_j , assuming the voxel concentrations to be w_i , is given by

$$P(\mathbf{A} | \mathbf{w}) = \prod_j \frac{\bar{A}_j^{A_j} e^{-\bar{A}_j}}{A_j!} \quad (5)$$

When this probability is maximal, so is its natural logarithm given by

$$\ln(P(\mathbf{A} | \mathbf{w})) = \sum_j \{A_j \ln \bar{A}_j - \bar{A}_j - \ln(A_j!)\} \quad (6)$$

To determine the most likely w_i , the partial derivatives with respect to w_i are taken and the values for w_i are to be found where all the partial derivatives are zero (note that all A_j are experimentally observed numbers not depending on the assumed values for w_i , as opposed to the expected \bar{A}_j):

$$\frac{\partial \ln(P(\mathbf{A} | \mathbf{w}))}{\partial w_i} = \sum_j \left\{ \frac{A_j}{\bar{A}_j} \frac{\partial \bar{A}_j}{\partial w_i} - \frac{\partial \bar{A}_j}{\partial w_i} \right\} = 0 \quad (7)$$

and using Equation 4 to find

$$\frac{\partial \bar{A}_j}{\partial w_i} = K_{ij} \quad (8)$$

the result is

$$\sum_j \left\{ \frac{A_j}{\bar{A}_j} K_{ij} - K_{ij} \right\} = 0 \quad (9)$$

Now, an entity N_{ij} , to be computed from the w_i values from the previous iteration, is defined as

$$N_{ij} = \frac{K_{ij} w_i A_j}{\sum_l K_{lj} w_l} \quad (10)$$

and Equation 9 transforms to

$$\frac{\partial \ln(P(\mathbf{A} | \mathbf{w}))}{\partial w_i} = \sum_j \left\{ \frac{N_{ij}}{w_i} - K_{ij} \right\} = 0 \quad (11)$$

which yields the new w_i :

$$w_i = \frac{\sum_j N_{ij}}{\sum_j K_{ij}}. \quad (12)$$

Now, if all initial estimates for local element concentrations $w_{i(0)}$ are positive, then the iteration will render positive values as well. The iteration is stopped as soon as the iteration number $k = k_{\max}$, a user-defined maximum to the number of iterations, or $\sum_{i=1}^N (w_{i(k+1)} - w_{i(k)})^2 \leq \Delta_{\min}$, a user-defined minimum change per iteration.

8.2.4 CGNN

The conjugate gradient method is an iterative method to determine a least-squares solution for a set of linear equations. In each iteration step a search vector, from a conjugate set, that minimises the error e , is added to the estimated solution. The non-negativity is constrained in each iteration by adjustment of the size of the search vector if necessary.

A least-squares solution for vector \mathbf{w} from Equation 1 can be found by minimisation of the error:

$$e = \|\mathbf{A} - \mathbf{K}\tilde{\mathbf{w}}\|^2 = (\mathbf{A} - \mathbf{K}\tilde{\mathbf{w}})^t (\mathbf{A} - \mathbf{K}\tilde{\mathbf{w}}), \quad (13)$$

where $\tilde{\mathbf{w}}$ is the solution to be found for the element distribution vector \mathbf{w} , and $()^t$ indicates the transpose of the vector. In the conjugate gradient method, $\tilde{\mathbf{w}}$ can be found by the following iterative algorithm:

$$\tilde{\mathbf{w}}_{(k+1)} = \tilde{\mathbf{w}}_{(k)} + \alpha_{(k)} \mathbf{d}_{(k)}, \quad (14)$$

where k is the iteration index, $\mathbf{d}_{(k)}$ is a search vector and $\alpha_{(k)}$ is the value for a scalar search factor in iteration step k . The residual vector after the iteration step $k+1$, $\mathbf{r}_{(k+1)} = \mathbf{K}^t(\mathbf{A} - \mathbf{K}\tilde{\mathbf{w}}_{(k+1)})$, has to be orthogonal to $\mathbf{d}_{(k)}$: $(\mathbf{r}_{(k+1)})^t \mathbf{d}_{(k)} = 0$.

This leads to:

$$\mathbf{r}_{(k+1)} = \mathbf{r}_{(k)} - \alpha_{(k)} \mathbf{K}^t \mathbf{K} \mathbf{d}_{(k)}. \quad (15)$$

To find the minimum of the error e , the partial derivative of Equation 13 with respect to $\alpha_{(k)}$, is set to zero:

$$\frac{\partial}{\partial \alpha} (\|\mathbf{A} - \mathbf{K}\mathbf{w}\|^2) = \frac{\partial}{\partial \alpha} (\|\mathbf{A} - \mathbf{K}(\mathbf{w}_{(k)} + \alpha_{(k)} \mathbf{d}_{(k)})\|^2) = 0 \Rightarrow \alpha_{(k)} = \frac{(\mathbf{d}_{(k)})^t \mathbf{r}_{(k)}}{(\mathbf{d}_{(k)})^t \mathbf{K}^t \mathbf{K} \mathbf{d}_{(k)}}. \quad (16)$$

The vector $\mathbf{d}_{(k)}$ can be derived from its conjugate property, $(\mathbf{d}_{(k)})^t \mathbf{K}^t \mathbf{K} \mathbf{d}_{(k')} = 0$ for $k \neq k'$, and its recursive relation to the residual vector:

$$\mathbf{d}_{(k)} = \mathbf{r}_{(k)} - \beta_{(k-1)} \mathbf{d}_{(k-1)}, \quad (17)$$

where $\beta_{(k)}$ is the orthogonality factor, which value can be determined by taking the inner product of Equation 17 with $\mathbf{K}^t \mathbf{K} \mathbf{d}_{(k-1)}$ and applying the conjugate property:

$$\beta_{(k-1)} = \frac{(\mathbf{r}_{(k)})^t \mathbf{K}^t \mathbf{K} \mathbf{d}_{(k-1)}}{(\mathbf{d}_{(k-1)})^t \mathbf{K}^t \mathbf{K} \mathbf{d}_{(k-1)}}. \quad (18)$$

The iteration can be applied, by starting with an initial estimate for $\tilde{\mathbf{w}}_{(1)}$ and a calculation of $\mathbf{d}_{(1)} = \mathbf{r}_{(1)} = \mathbf{K}^t(\mathbf{A} - \mathbf{K}\tilde{\mathbf{w}}_{(1)})$. The loop starts now with $k=1$. The calculation of $\alpha_{(k)}$, $\mathbf{r}_{(k+1)}$, $\beta_{(k)}$ and $\mathbf{d}_{(k+1)}$ is performed based on applying successively equations 16, 15, 18 and 17. The iteration is stopped as soon as $k = k_{\max}$, a user-defined maximum to the iterations, or if the residual vector becomes smaller than a user-defined minimum.

According to Chang *et al.* [6], the non-negativity constraint was satisfied in each iteration by finding the minimum value for any $\tilde{w}_{i(k+1)}$. If this value was found to be negative, then $\alpha_{(k)}$ was adjusted:

$$\alpha_{(k)_{new}} = \alpha_{(k)} \tilde{w}_{i'(k)} / (\tilde{w}_{i'(k)} - \tilde{w}_{i'(k+1)}) = -\tilde{w}_{i'(k)} / d_{i'(k)},$$

where i' marked the minimum $\tilde{w}_{i(k+1)}$. Finally $\tilde{w}_{(k+1)}$ was recalculated.

But, considering Equation 14, it can be demonstrated that this will not uphold the non-negativity. If there exists an i'' such that

$$\tilde{w}_{i'(k+1)} < \tilde{w}_{i''(k+1)} = \tilde{w}_{i''(k)} + \alpha_{(k)} d_{i''(k)} < 0 \text{ and } -\tilde{w}_{i''(k)} / d_{i''(k)} < -\tilde{w}_{i'(k)} / d_{i'(k)},$$

the recalculated $\tilde{w}_{i''(k+1)}$ will be: $\tilde{w}_{i''(k+1)} = \tilde{w}_{i''(k)} - \tilde{w}_{i'(k)} d_{i''(k)} / d_{i'(k)} < 0$.

To solve this problem, the ratios of the iterated components to their change in the last iteration are considered: $\kappa_i = \tilde{w}_{i(k)} / (\tilde{w}_{i(k)} - \tilde{w}_{i(k+1)})$. This value indicates a violation of the non-negativity constraint if $0 < \kappa_i < 1$ for any i . This can be remedied by selecting the smallest κ that violates the non-negativity constraint: $\kappa_{min} = \text{Minimum}(0 < \kappa_i < 1)$, and redefine $\alpha_{(k)_{new}} = \kappa_{min} \alpha_{(k)}$. The components of \mathbf{w} that have been minimised this way should no longer be considered in the iteration to prevent that the algorithm will only try to reminimise these components (for which of course $\kappa_i = 0$ in subsequent iterations).

8.2.5 Reconstruction: Error propagation

Both reconstruction algorithms render a solution without any propagation of uncertainties in the measured or predicted peak areas. To find an indication of the impact of the uncertainties on the solution, the uncertainties are propagated to the algorithms by 15 times solving the reconstruction again after adding randomly, normally distributed errors with a standard deviation equal to the known uncertainties. This leads to 15 modified solutions. The standard deviation in this series of solutions is taken to represent the propagated uncertainty in the solution for the element distribution.

8.3 Modelling studies and phantom experiment

In this chapter only mathematically modelled samples and phantom measurements are considered. The aims are, to verify the applicability of the reconstruction algorithms for noisy spectra and of holistic analysis for scanned measurements.

The testing is done in three steps, firstly with two simulation studies to determine the robustness of the reconstruction algorithms without and with noise in the spectra. In these simulations, the efficiency matrices K are not derived from efficiency calculations as described in Chapter 4, but are more simple models. The spectra contain only one channel of which the contents are calculated using these simple efficiency matrices.

Then, as step 3, a sample with a known, simple inhomogeneous distribution was manufactured, irradiated and measured to test the total procedure of spectrum fitting, prediction and the reconstruction algorithms.

Step 1. Noise-free reconstruction: Measurement and reconstruction matrix are simulated: An artificial detection efficiency matrix is modeled: $K_{ij} = 2^{-|i-j|}$, the artificial element distribution is $w_i = i+1$ (a.u.) and the artificial single channel contents peak areas are calculated with $n_j = \sum_{i=1}^{100} w_i K_{ij}$, i.e. noise-free

Step 2. Reconstruction with counting statistics: Measurement and reconstruction matrix again are simulated: the same efficiency matrix $K_{ij} = 2^{-|i-j|}$, and $w_i = i+10,000$ with a ‘hot spot’ peak at $i=0$: $w_0 = 20,000$. These numbers of counts are to be much larger than in the first simulation experiment to justify the use of Gaussian noise instead of Poisson noise. The artificial, noisy single-channel contents or peak areas are now calculated with:

$n_j = \sum_{i=1}^{100} w_i K_{ij} + R(\sqrt{\sum_{i=1}^{100} w_i K_{ij}})$, where $R(x)$ is an algorithm that generates a random value for a Gaussian distribution with peak width x .

Step 3. Reconstruction with all sources of error in the analysis: Scanned measurements of a manufactured sample were used. A 3 g Zn sheet was inserted into a bottle containing sand (radius 47mm, height 16 cm and mass 1.4 kg) to serve, after irradiation, as a “hot spot” inhomogeneity. This sample is previously described as the second sample in Section 6.4. The sample was considered to consist of three wedge of cake shaped voxels per layer of 2 cm

each, *i.e.* altogether 24 voxels. Originally, the Zn sheet was positioned in the centre of a voxel. The gamma-ray attenuation was determined for each voxel according to the method described in Chapter 7.

In all three experiments, the reconstructed distribution is compared with the known distribution via the mean square error MSE [g^2]: [8]

$$\text{MSE}(\mathbf{w}, \tilde{\mathbf{w}}) = \|\mathbf{w} - \tilde{\mathbf{w}}\|^2 \quad (19)$$

and the I-divergence, I-div (g): [9]

$$I - \text{div}(\mathbf{w}, \tilde{\mathbf{w}}) = \sum_i w_i \ln \left(\frac{w_i}{\tilde{w}_i} \right) - (w_i - \tilde{w}_i). \quad (20)$$

Minimising the I-div is equal to maximising the mean of the log-likelihood from Equation 6 [9], whereas the MSE is the best measure of divergence for a Gaussian distribution.

8.4 Results

The results for the MSE and I-div are presented for the three test samples and the two reconstruction algorithms in Figure 2 through 3.

Step 1. Figure 2 presents the results for the mathematical model without noise.

It can be seen that for both algorithms, MLEM and CGNN, the divergence, both MSE and I-div, is still decreasing, even after 100 iterations. Hence both algorithms do not render the mathematically correct, optimum solution though they are really iterating towards that asymptotic solution.

Step 2. Figure 3 shows the divergence as a function of iteration number for the noisy data set. It can be seen that the CGNN algorithm needs less iterations than MLEM to reach its minimum, but MLEM finds a lower minimum. It can also be seen that both algorithms reach a minimum divergence and then the divergence increases again after each iteration. This effect is due to noise amplification [8], and makes it difficult to find a best stopping criterion for the iterations if the solution is unknown.

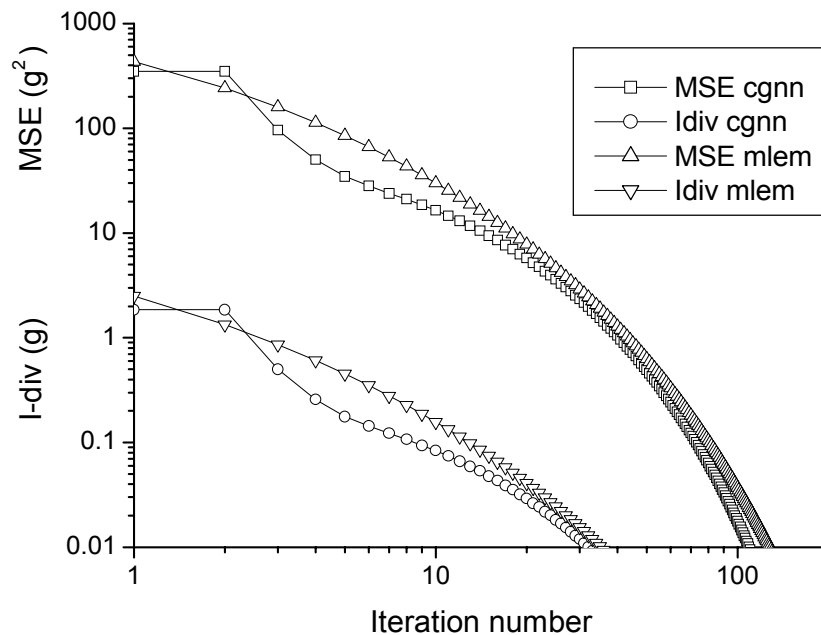


Figure 2 Divergence between true and reconstructed noise free data-set as a function of iteration number for two reconstruction algorithms and two definitions of divergence.

Step 3. The divergence as a function of iteration number for the irradiated test sample, as presented in Figure 4 shows that the MSE reaches a minimum after 30-50 iterations for both reconstruction algorithms, and then increases again. On the other hand, for CGNN the I-divergence, is still decreasing after more than 1000 iterations, apart from some fluctuations.

The reconstructed results for this sample are presented in Figure 4, together with a bar-graph of the real Zn distribution. The reconstruction via MLEM does not show significant amounts of Zn in the empty voxels, whereas CGNN finds small amounts of Zn in two empty voxels, which are in fact the neighbours of the Zn-containing voxel. The MLEM- reconstructed amount in the filled voxel is closer to the real amount than the amount obtained through CGNN but still deviates by about 20 %.

8.5 Discussion and conclusions

In this chapter the theory and methods for REDNAILS have been presented and tested.

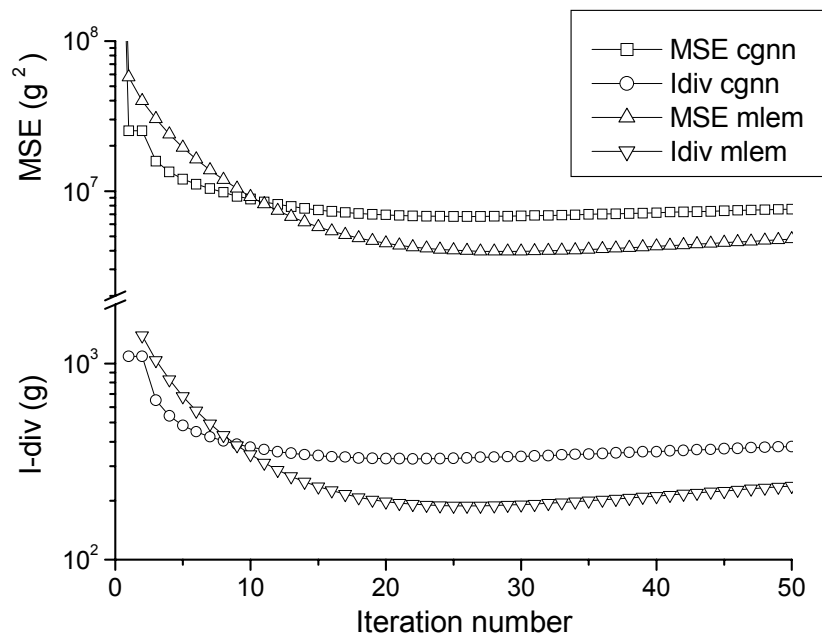


Figure 3 Divergence between true and reconstructed noisy data-set as a function of iteration number for two reconstruction algorithms and two definitions of convergence.

The results show that inhomogeneities can be detected and located. The reported size of the point source in the phantom sample is still overestimated by 20-40 %. Therefore, several steps in the reconstruction method that may explain the overestimation need further investigation with practice samples. This will be presented in Chapter 9. Though the steps that have been tested in this chapter have to be discussed here.

8.5.1 Neutron-flux distribution

The theory and methods for determining the neutron-flux distribution within the sample were directly imported from Overwater's work [10], via Equation 2, into the peak area prediction. A comment on the validity of doing so:

A practical point is that the neutron flux distribution is not cylindrically symmetrical, unless the container is rotated during irradiation. For the usual analysis of homogeneous samples, no problem arises as long as the sample is rotated during measurements only, since correction factors are integrated over the sample. But for reconstruction of the element distribution in rotational voxels, the

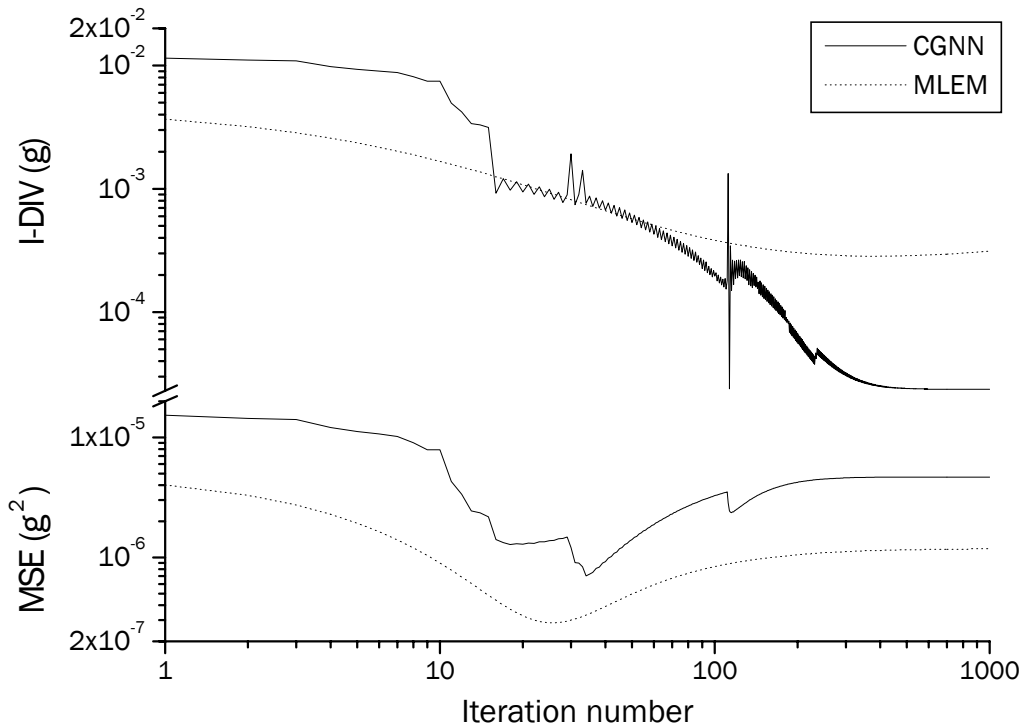


Figure 4 Divergence of results from real Zn amounts for reconstructed test sample as a function of iteration number for two reconstruction algorithms and two definitions of divergence, showing that the divergence has now some irregularities especially for CGNN and that after a decrease the divergence increases again.

sample must be rotated during irradiation or its position must be well defined during irradiation and at the start of the measurements in order to get the correct local neutron flux and gamma efficiency correction factors. This has been improved for the experiments in Chapter 9.

8.5.2 Signal-to-noise ratio

A large problem for tomography on neutron-activated samples is the low induced activity and thereby the small signal-to-noise ratio and the large relative uncertainties of peak areas. These errors are amplified in the reconstruction,

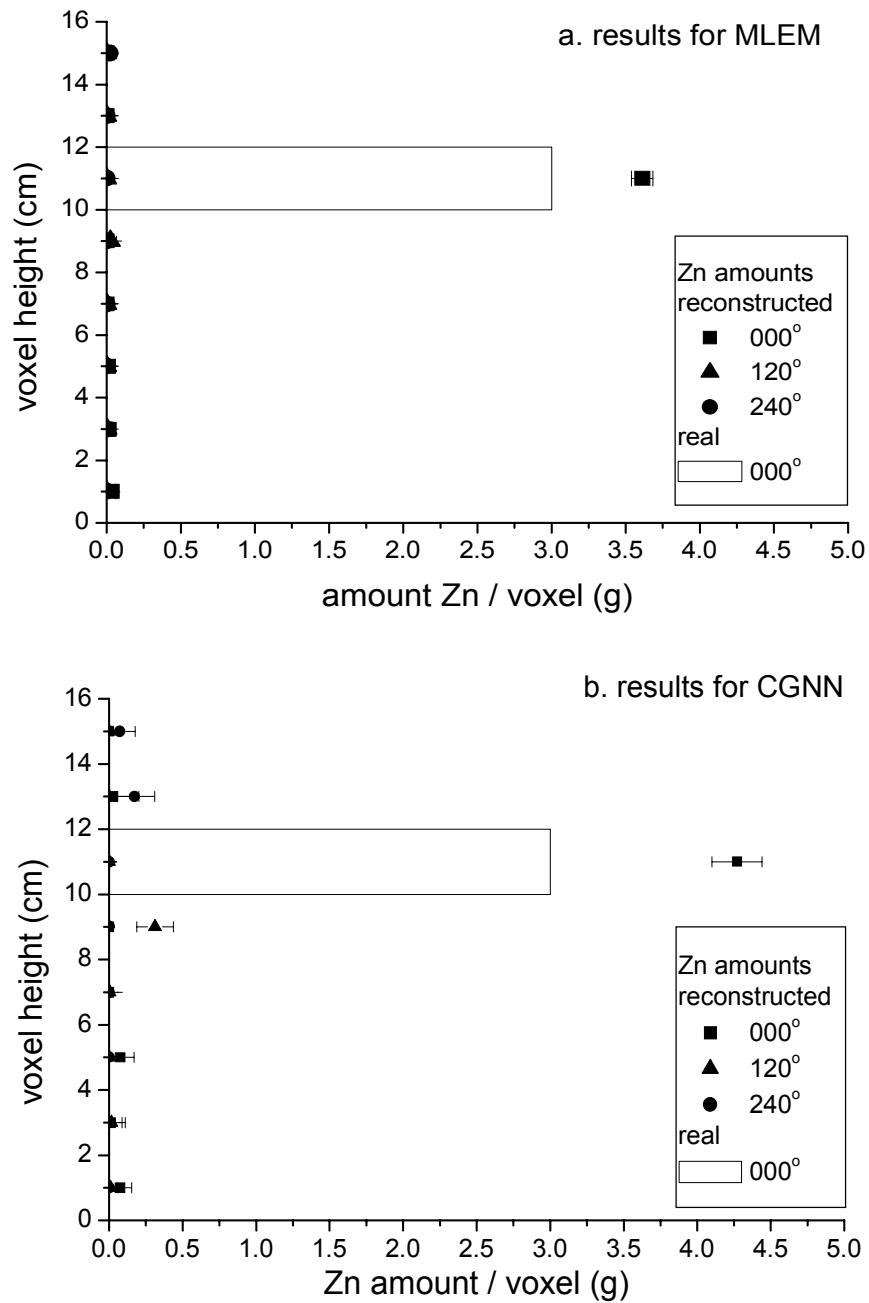


Figure 5 Comparison of reconstruction results and real values for test sample containing a sheet of Zn (3.0 g), using (a) the MLEM and (b) the CGNN algorithm, after 1000 iterations.

especially in reconstruction of spatial distributions in which the predicted spectra of one element from different voxels are highly correlated. This renders an ill-conditioned matrix of predicted spectra: it may be still invertible using one of the reconstruction algorithms, but the reconstruction is unstable.

8.5.3 Comparison of the reconstruction algorithms

For the reconstruction two algorithms have been applied. The second modelling study gives a simple impression of the performance of the two algorithms. From Figure 3 it can be concluded that CGNN is faster, *i.e.* it takes less iteration steps to reach the best solution. On the other hand, both Figure 2 and Figure 5 show that MLEM reaches a better solution. For the current experiments, the latter criterion is more important than the speed of the reconstruction.

The second modelling study and the phantom measurement do not show whether one of the algorithms is better. The phantom spectra are too noisy to allow for the reconstruction of a detailed spatial distribution.

8.6 References

1. R.M.W. Overwater, P. Bode, J.J.M. De Goeij, J.E. Hoogenboom, Feasibility of elemental analysis of kilogram-size samples by instrumental neutron activation analysis, *Anal. Chem.* 68 (1996) 341-348.
2. M. Blaauw, The holistic analysis of gamma-ray spectra in instrumental neutron activation analysis, *Nucl. Instr. Meth. A* 353 (1994) 269-271
3. C.L. Lawson, R.J. Hanson, *Solving least squares problems*, Prentice-Hall, New York, 1974.
4. L.A. Shepp, Y Vardi, Maximum Likelihood Reconstruction for Emission Tomography, *IEEE Trans. Med. Imag.* MI-1 (1982) 113-122
5. K Lange, R Carson, EM Reconstruction Algorithms for Emission and Transmission Tomography, *J. Comp. Assist Tomography* 8 (1984) 306-316
6. C.J. Chang, S Anghaie, Iterative Reconstruction and Statistical Optimization for the Nondestructive Assay of Distributed Gamma Source in a Large Nuclear Waste Container, *IEEE Trans. Nucl. Sci.* 45 (2) (1998) 146-153
7. W.R. Leo, *Techniques for Nuclear and Particle Physics Experiments, A How-to Approach*, 2nd Ed. Springer Verlag, Berlin 1994

8. G.M.P. van Kempen, L.J. van Vliet, P.J. Verveer, Application of image restoration methods for confocal fluorescence microscopy, Proc. SPIE 2984 (1997) 114-124.
9. D.L. Snyder, T.J. Schultz J.A. O'Sullivan, deblurring subject to nonnegative constraints, IEEE Trans. Signal Processing 40 (1992) 1143-1150.
10. R.M.W. Overwater, J.E. Hoogenboom, Accounting for the thermal neutron flux depression in voluminous samples for instrumental neutron activation analysis ,Nucl. Sci. Eng. 117 (1994) 141-157

Chapter 9

REDNAILS: Application with prior knowledge to samples of practical interest

9.1 Introduction

In the previous chapters the theory and principles of REDNAILS have been introduced and merged in Chapter 8 to test the reconstruction algorithms with simulated sample models and one artificial sample. It was concluded that the method was able to localise inhomogeneities but was unable to give accurate amounts for the spatial element distribution of the artificial sample. Hence adjustments have to be made to increase the accuracy. These adjustments focus on the stability of the reconstruction. Adjustments aiming at better approximation of elemental amounts in 'hot spots' are discussed in Chapter 10.

In this chapter, the applicability of REDNAILS to samples of practical interest is investigated in order to study the following aspects. Not only the spatial resolution and detection limits are studied, but also is under consideration to what extent REDNAILS can be adjusted to realistic samples, using prior knowledge about the spatial distribution of elements.

First one sample has been analysed exactly according to the method described in the previous chapter. Secondly, the method is adjusted to allow for larger numbers of voxels as well as the introduction of assumptions on the inhomogeneity distribution in order to stabilise the results of the reconstruction and to obtain more accurate results. The adjusted method(s) were then applied to two additional samples.

In the next section some adjustments to the method described in the previous chapter are introduced

9.2 Theory

9.2.1 “Geosampling”

In Chapter 2 some issues about sampling have been discussed. It was mentioned that for better insight into sample representativeness in large-sample analysis, the structure within the sample should be known. As described before, LS-INAA has been introduced to allow for the analysis of large inhomogeneous samples without destruction of the sample structure. It is known that inhomogeneities, mainly of gamma-ray emitting radionuclides, might introduce errors in this analysis. If such inhomogeneities are present in the sample, then they can be detected by the method described in Chapter 5 and finally made quantitative according to the method given in Chapter 6. But, as demonstrated and discussed in the previous chapter, this method is sensitive to background and statistical noise. This will be further demonstrated in the straightforward analysis applied to the first sample. To make REDNAILS applicable to more noisy circumstances, possible assumptions about sample composition are considered here.

LS-INAA is mainly applied to geological samples. These samples sometimes are the result of vertical bore-hole logging through material that has been deposited over a wider area in successive periods of time. This means that these cylindrical samples have a typical layered structure.

9.2.2 *Optimisation of speed and spatial resolution in the reconstruction*

As discussed in the previous chapter, the MLEM algorithm renders the best results in the reconstruction, but takes more time than the other. The latter becomes a more serious problem for the analysis of a sample as the number of voxels increases. To allow for a solution of a large system of equations in a reasonable amount of time, the method needs reduction.

Secondly, the spectra are rather noisy and, especially for the high-energy gamma's, rather similar due to collimator leakage. 'Inversion' of such data may lead to unstable element-distribution results. As discussed in the previous chapter, this stabilisation can be achieved by making assumptions about the element distributions and incorporating these in the reconstruction.

For example, homogeneity can be assumed for some of the layers just outside the focus of collimator, and zero detection efficiency can be assumed for layers even further away. The element distribution vector \mathbf{w} is determined by considering the amounts $w_{i\alpha}$ of the elements in voxel α in layer i in three different ways:

1. **0 neighbours:** considering the single layer i in front of the detector, a 3x3 square [voxels x measurements] is cut of from the matrix \mathbf{K} , with central element $K_{i\alpha i\alpha}$, with second and fourth subscript for the rotational position of the voxel and the measurement respectively. Now the $w_{i\alpha}$ values are solved within this window, assuming that $w_{(i-2)\alpha} = w_{(i-1)\alpha} = w_{i\alpha} = w_{(i+1)\alpha} = w_{(i+2)\alpha}$. In other words, the voxels in the layers above and below the current layer are assumed to have the same composition as the voxels in the current layer and there may be only difference between the compositions of voxels of different rotational position.
2. **1 neighbour:** is based on the previous method, but now the relative layers -1 and +1 are taken into account as well: considering the three layers $i-1$, i and $i+1$ in front of the detector, a 9x9 square is cut of from the matrix \mathbf{K} , with central element $K_{i\alpha i\alpha}$. Now the $w_{i\alpha}$ values are solved within this window, assuming that $w_{(i-3)\alpha} = w_{(i-2)\alpha} = w_{(i-1)\alpha}$ and $w_{(i+1)\alpha} = w_{(i+2)\alpha} = w_{(i+3)\alpha}$, but only the results $w_{i\alpha}$ for the central layer i are kept for the final solution. In other words, the voxels in the layers above and below the central three layers are assumed to have the same composition as the voxels in upper and lower of the central three layers, respectively.
3. **2 neighbours:** is an extension of the 1 neighbour method, but now the relative layers -2 and +2 are taken into account as well: considering the five layers $i-2$, $i-1$, i , $i+1$ and $i+2$ in front of the detector, a 15x15 square is cut of from the matrix \mathbf{K} , with central element $K_{i\alpha i\alpha}$. Now the $w_{i\alpha}$ values are solved within this window, assuming that $w_{(i-4)\alpha} = w_{(i-3)\alpha} = w_{(i-2)\alpha}$ and $w_{(i+2)\alpha} = w_{(i+3)\alpha} = w_{(i+4)\alpha}$, but only the results $w_{i\alpha}$ for the central layer i are kept for the final solution. In other words, the voxels in the layers above and below the central

five layers are assumed to have the same composition as the voxels in the upper and lower of the central five layers, respectively.

The same methods can also be applied considering only layers instead of voxels, by assuming each layer to be homogeneous in itself. In that case the subscript α is omitted.

9.3 Methods and results

9.3.1 Analysis without use of a priori knowledge

Methods

A 1.4 dm³ sample was analysed using the methods described in Chapter 6. It consisted of three different layers of 6 cm each: dried harbour sediment, sand and milk powder, containing three different ‘hot-spots’: La, Ta and Zn, as shown in Figure 1. The sample was irradiated (without rotating it) for 9 hours with flux monitors in the BISNIS standard average neutron flux of 3×10^{12} m⁻²s⁻¹, and measured twice:

- a) 4 days after irradiation 120 s/single spectrum, 5 cm thick collimator)
- b) 8 months after irradiation 240 s/single spectrum, 10 cm thick collimator).

Results

The results of the measurements 4 days after irradiation are presented in Figure 2 and Figure 3. Only reconstruction results for the elements present in the point sources (Zn, La, Ta) and some major elements in the bulk of the sample (Br, Fe, Sc) are reported.

Figure 2, presenting the results for the reconstruction of the point source elements, shows that the positions of the La and Ta source are well reconstructed for both MLEM and CGNN, but the source strength is significantly different from the real value, as shown in Table 1. This can be explained by the uncertainty of the position of the point source, and by the fact that the voxel is larger than the point source; in this respect the real neutron flux and detection efficiency differ from the modelled one. The reconstruction of the Zn point source is even worse: the reconstructed Zn profile is distributed over the whole layer and it can be seen that

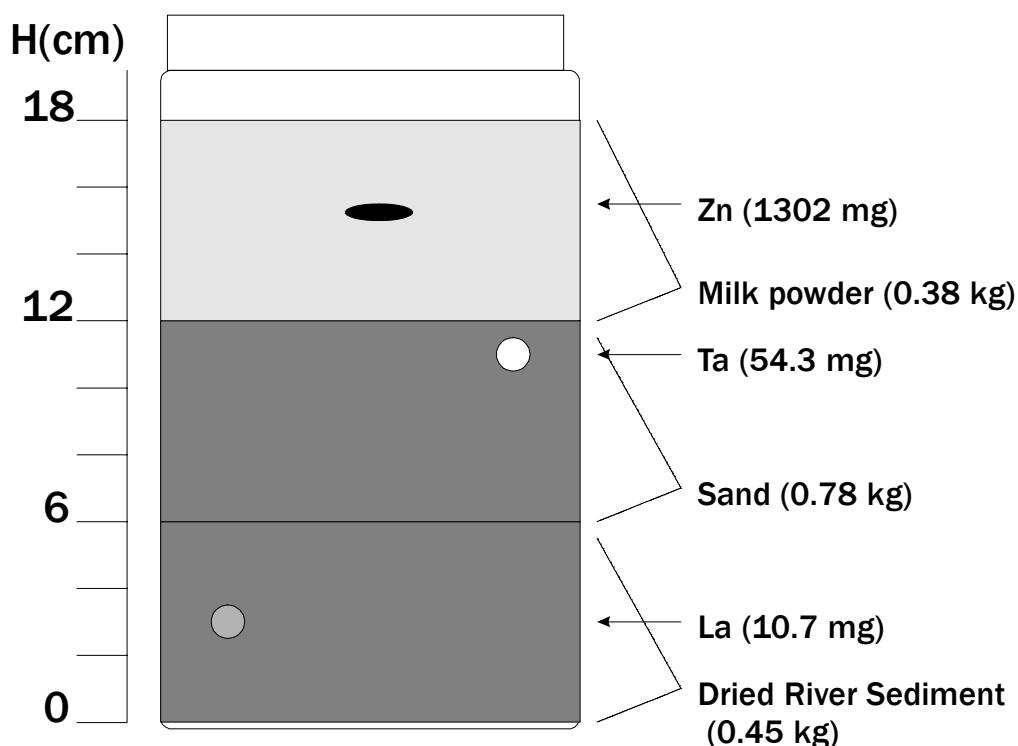


Figure 1 Schematic drawing of artificial sample 1, the rotational position of the hot spots is given in Figure 2.

the collimator did not shield the top of the sample during the measurement of the bottom layer. This makes the reconstruction unstable.

The real concentration of the three major elements is derived from INAA of a small sample of the dried sediment, of which the 6 cm bottom layer is made. The elements may also be present in the sand and the milk powder, but in a negligible concentration as compared to the concentration in the dried sediment. The results for Br, Sc and Fe are presented in Figure 3, together with the concentrations reported by small sample INAA, performed on the dried sediment; concentrations of relevant elements in the other layers were assumed to be negligible. The error bars for Sc and Br show that these elements were detected well above their detection limits. The reconstruction results show a large fluctuation that is not caused by the Poisson distribution in counting statistics. It can be seen from the layer averages, that the instability is mainly within the reconstruction of each separate layer. For Fe, the uncertainty of the reconstruction is larger; the detection limit is in the order of 1 g/voxel.

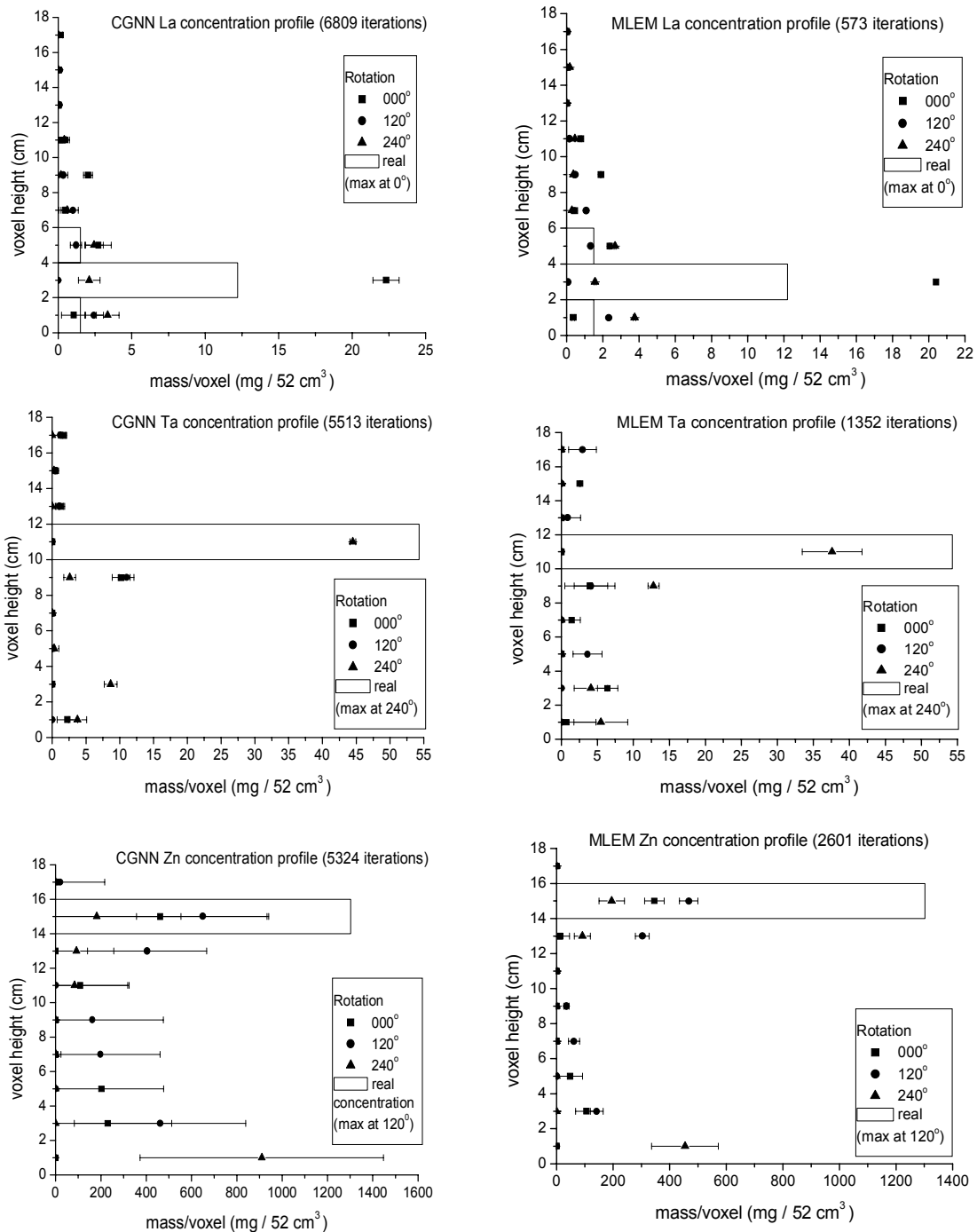


Figure 2 Results for the reconstruction of point concentrated elements: La, Ta and Zn, in the first sample in the first scan, 4 days after irradiation.

Table 1: Comparison between real and calculated point sources [mg] for sample 1a. Only amounts calculated for the corresponding voxel are considered

	MLEM	(+/- %)	CGNN	(+/- %)	REAL	(+/- %)
Zn	467	7	649	45	1.30 x10 ³	1
Ta	37.6	11	44.5	1	54.3	1
La	20.4	1	22.3	4	12.2	1

For this sample, the results of the measurements 8 months after irradiation are presented in Figure 4. In the first session the collimator was only 5 cm thick. Therefore the sample was measured again, now using the 10 cm thick collimator. This was done only after 8 months, so there were no detectable amounts of ¹⁴⁰La or ⁸²Br left. Figure 4 shows the results for Zn, Ta and Sc. It can be concluded that the Zn and Ta point sources have sunk about half a layer deeper into the sample. The reconstruction of Zn has become better with the new collimator thickness.

9.3.2 adjusted method

Methods

A beaker-sampler was used to take two samples close to each other from a ditch bottom. These samples, coded YA02 and YD03, both cylinders of 94 cm length and 13 cm in diameter, were analysed in 47 layers of 3 voxels of 88 cm³ each. To create these voxels physically for future verification of the results by ordinary INAA, one sample (YA02), in frozen condition, was sliced in layers of 2 cm each and each layer put in a plastic petri dish with 120° partitions. The petri dishes were stacked on top of each other to reconstruct the sample.

The sample labelled YA02 first was measured for natural activity in 30 min/voxel. Next the sample was irradiated (without being rotated) for 1.972 days with a standard neutron flux in the BISNIS facility. The activated sample was measured once, 19 days after irradiation for 30 min/voxel.

The interpretation was performed per voxel, using MLEM and the 0 neighbour methods. The interpretation was also performed per layer with the 0, 1 and 2 neighbour method.

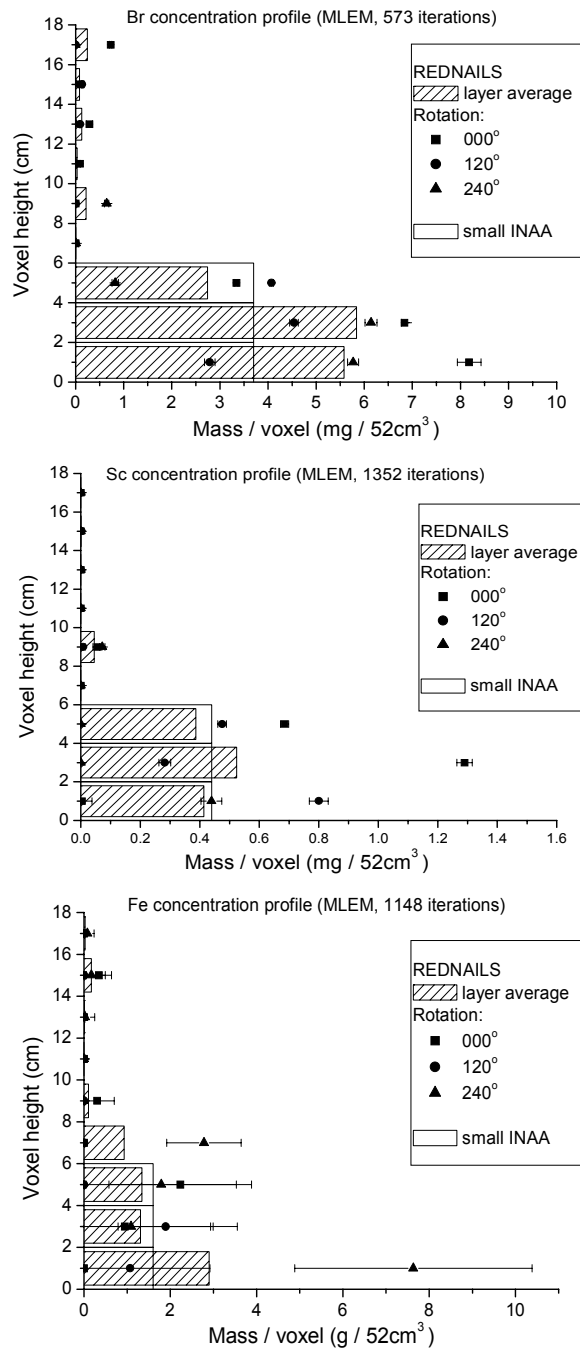


Figure 3 Results for the reconstruction of the concentration profile of the elements: Br, Sc and Fe, in the first sample in the first scan, 4 days after irradiation.

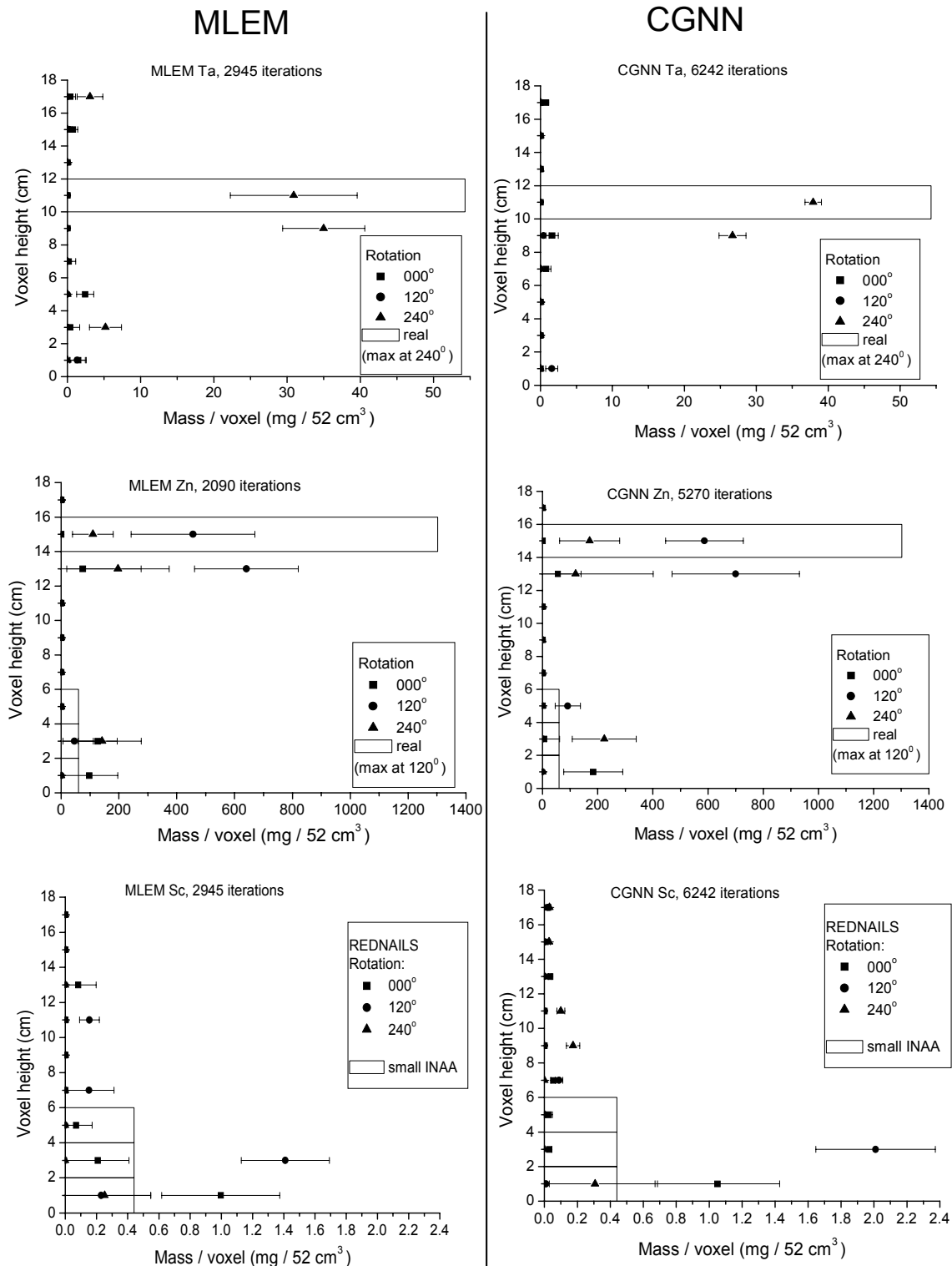


Figure 4 Results for the reconstruction of the concentration profile of the elements Zn, Ta and Sc, in the first sample in the second scan, 8 months after irradiation

For verification of the analysis method, 14 voxels were selected from 12 layers for analysis with small sample INAA. The last three voxels were from a single layer to investigate variation within a layer. The material in each voxel was dried, then weighed, and homogenised before a subsample was taken for analysis by ordinary INAA. The samples were irradiated in a neutron flux of $4.7 \times 10^{16} \text{ m}^{-2}\text{s}^{-1}$ and measured during 1 hour in a well-type HPGe detector after 6 days waiting time.

The second sample, labelled YD03, was irradiated (without being rotated) for 2.17 days with a standard neutron flux in the BISNIS facility after a scanned natural activity measurement of 30 min/voxel. The activated sample was measured for the first time after 5 days waiting time for 6 min/voxel, for a second time after 16 days for 30 min/voxel and for the third time after 74 days for 60 min/voxel.

Interpretation of the spectra was performed using the 0-neighbour method, per layer, dealing with 3 spectra per layer, where each spectrum was the sum of the three spectra gathered from the three voxels of that layer at one point in time.

Results

Figure 5 shows the results of sample YA02 for Fe and Sc using REDNAILS with the 0-neighbours analysis per voxel. The results still show systematic deviations for the voxels at 120° and 240° . When the individual voxel results for Sc are divided by the per-layer result and averaged over the three stacks of 120° -voxels that constitute the sample, the weighted averages are 1.02 ± 0.01 , 0.81 ± 0.02 and 1.34 ± 0.02 . Since there is no reason for these differences from unity to occur apart from measurement errors, orientation-dependent bias is the most likely explanation. Such a bias could be due to imprecise positioning of the sample during irradiation or measurement, or due to inaccurate modelling of the neutron flux distribution during irradiation.

The results per layer for Fe, Sc and Cr using INAA and REDNAILS with the 0, 1 and 2-neighbour method are presented in Figure 6. The graphs show that the three interpretation methods introduced in Section 9.2.2 do not lead to significantly different results. The 0-neighbour method gives the smoothest result. The 1-neighbour and even some more the 2-neighbours method demonstrate small fluctuations probably due to the so-called "ringing" effects known to occur in image restoration techniques near discontinuities. Ways to circumvent this problem will be discussed in the next chapter.

Figure 6 demonstrates also that all three methods agree well on most points with the INAA results. Only from 0.5 to 8.0 cm height relative to the centre of mass the REDNAILS results seem to underestimate the element amounts.

The interpretation of the measurements of the flux monitors used for the

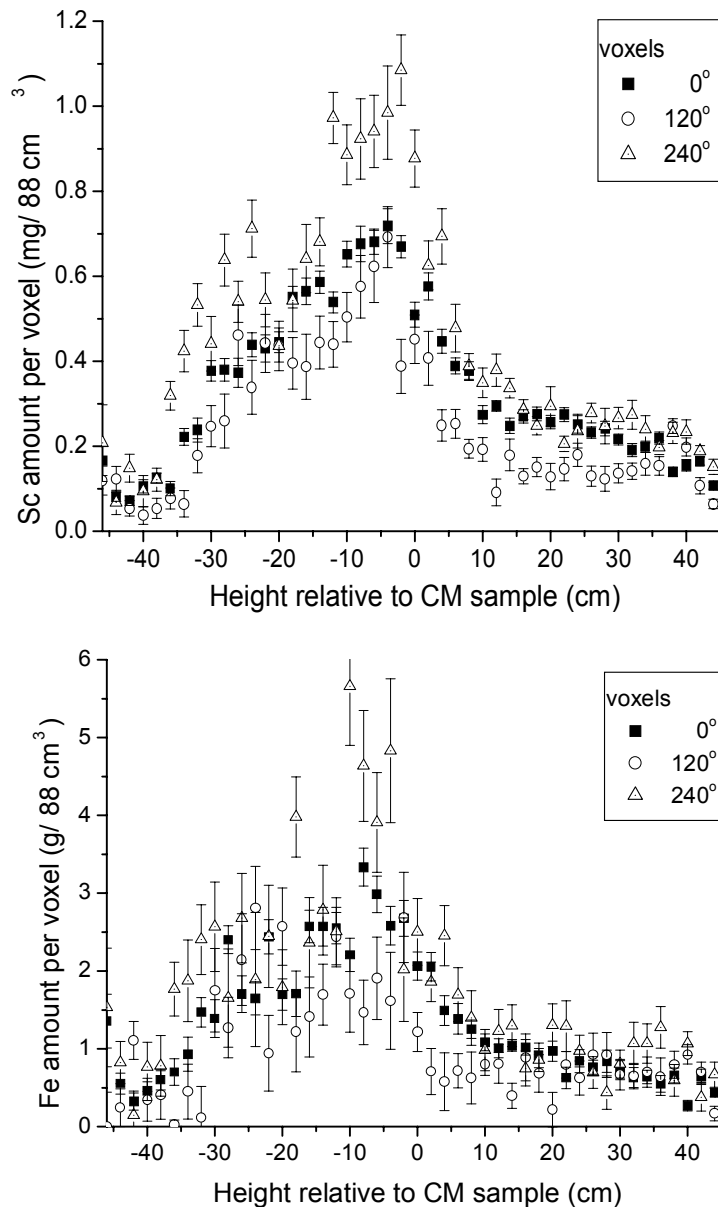


Figure 5. Results for concentration profiles of Sc and Fe in YA02 using the 0-neighbours method and analysis per voxel, reported in amount per voxel. For both elements, concentrations in the voxel at 120° are below and at 240° above layer average

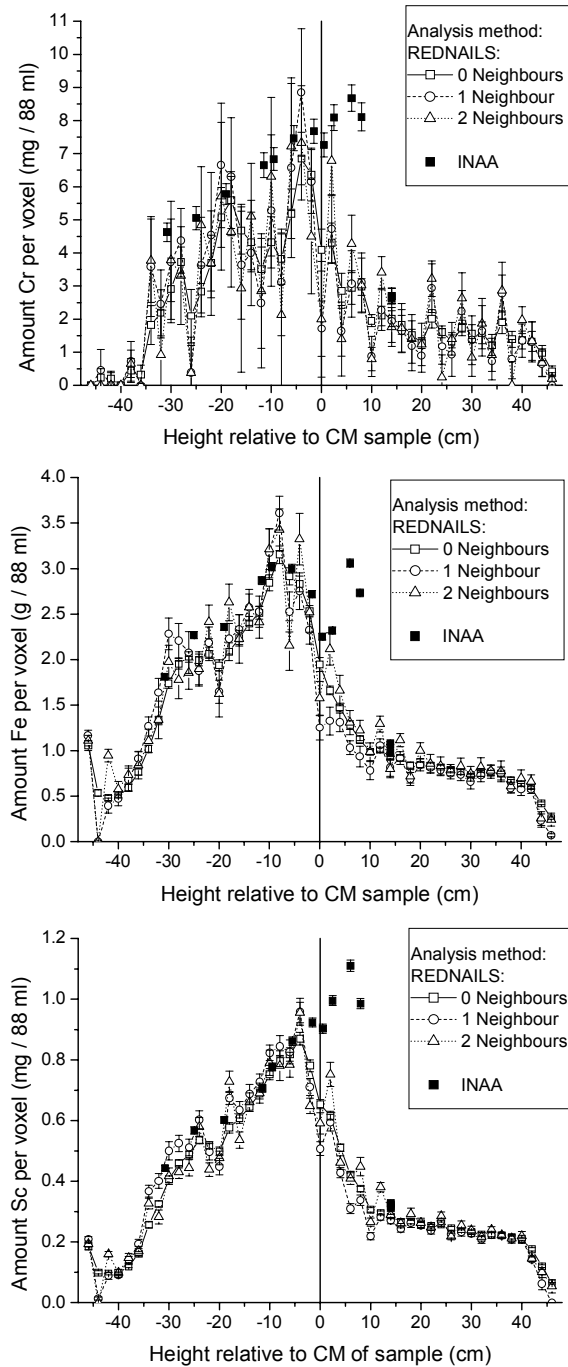


Figure 6. Results for concentration profiles per calculated per layer of Cr, Fe and Sc in sample YA02. Reported in amount of that element per voxel. Comparison between REDNAILS and INAA. Lines between symbols are added for REDNAILS to show profile.

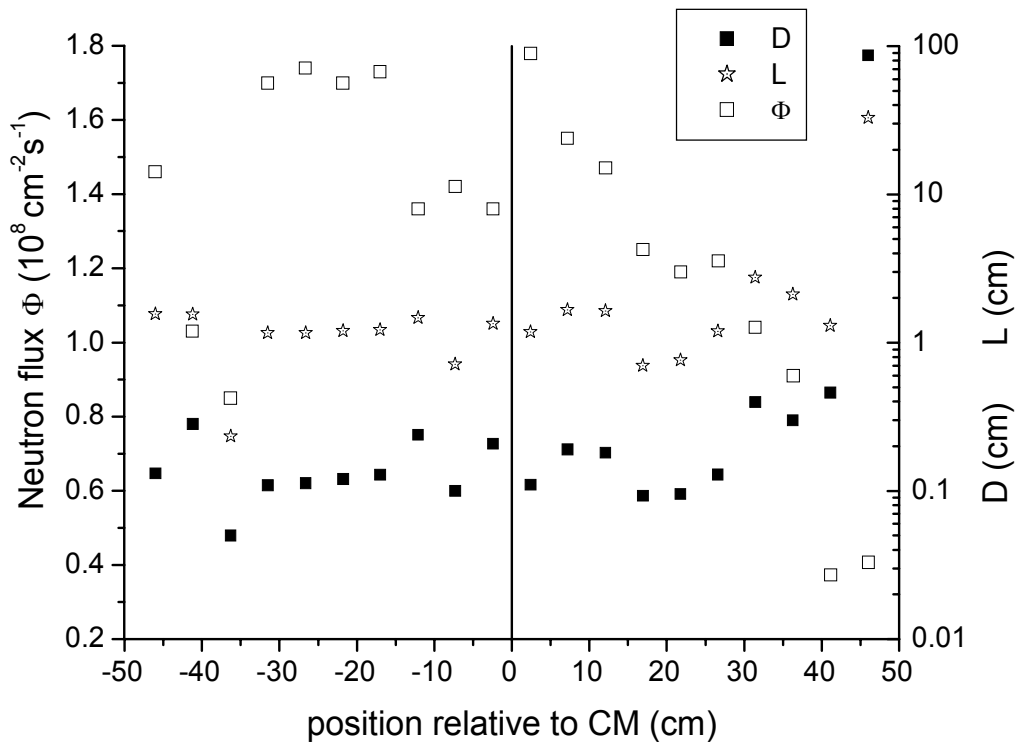


Figure 7 Parameters fitted on neutron flux monitors, describing the neutron flux Φ outside the sample YA02, the diffusion length L and the diffusion coefficient D , applied in Overwaters description for neutron transport within a sample, see Section 3.4.1. [1].

irradiation of this sample, are presented in Figure 7. It can be seen that diffusion length L and diffusion coefficient D are quite stable in the middle of the sample, but the neutron flux outside the sample shows a strange peak between 0 and 5 cm relative to the vertical sample centre (CM). This may be, at least partially, the cause of REDNAILS underestimating the element concentrations.

The results for the last three INAA subsamples, sampled from the same layer, demonstrate that for this sample variation within that layer is negligible.

The results of the analysis of sample YD03, using the 0-neighbour method and reconstruction per layer, are presented in Figure 8 for the elements Na, K, Ca, Fe, Sc, Co, La, Cr and Br. The elements that were also reported for sample YA02 now have smaller uncertainties. Na, K, Ca, La and Br have not been reported for YA02. Other samples reported for sample YD03 but not presented in the graph are Zn, Cs, Eu, Er, Hf, Ta, Ir and Th. More elements were detected in YD03 than in YA02 due to the fact that this sample is measured three times, which allows for

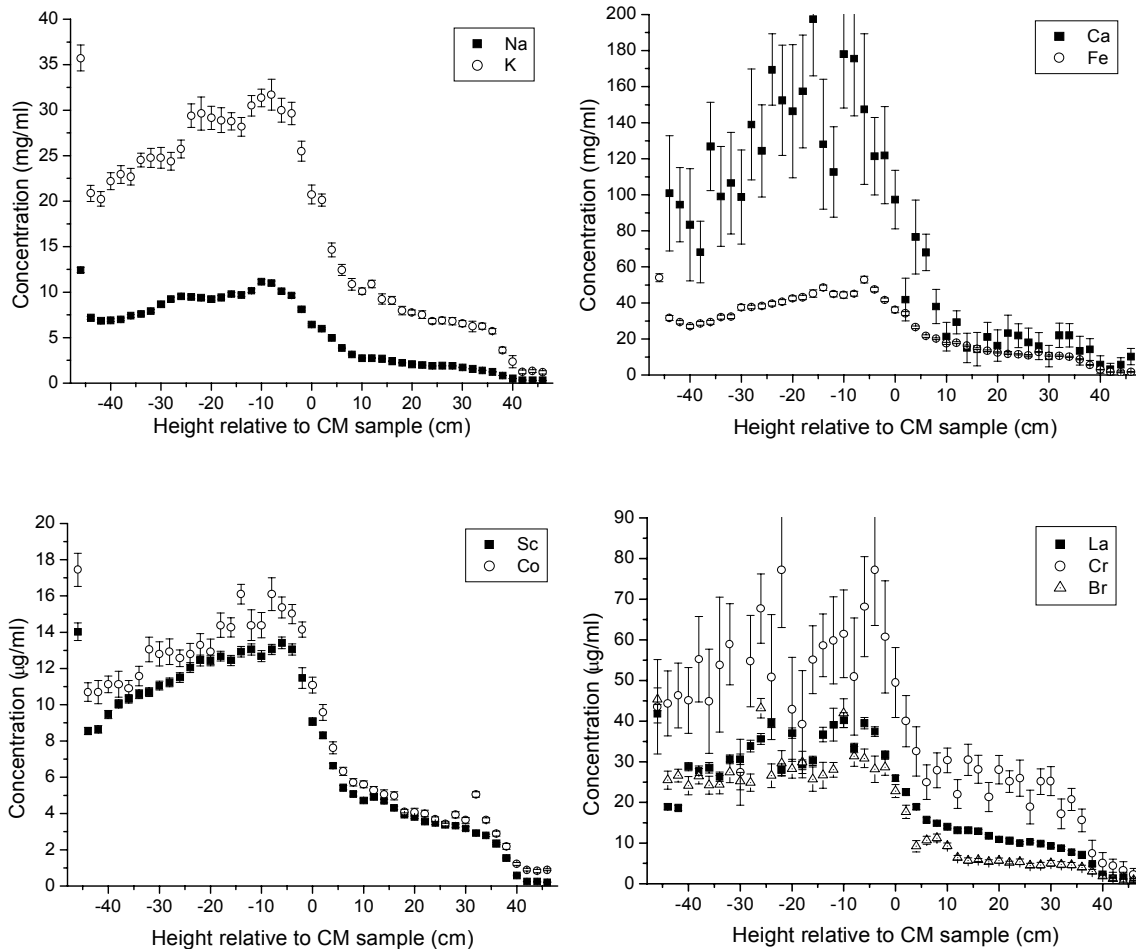


Figure 8 Results for concentration profiles of Na, K, Ca, Fe, Sc, Co, La, Cr and Br for sample YD03 using the 0-neighbour method per layer. Reported in amount of that element per ml of the wet sample.

detection of shorter-lived radionuclides in a first quick measurement and improved detection of longer-lived radionuclides in a later measurement that takes more time per measurement.

From Figure 8 it is clear that all elements show roughly the same concentration profile. This is due to vertical variations of sample dry mass density. Hence, if the dry mass of each voxel would have been determined and the concentrations would have been calculated in mg/g dry mass, the concentration profiles would look much more flat.

9.4 Discussion and conclusions

In this chapter REDNAILS is applied to real samples. Problems that arise in practice have been discussed together with possibilities for stabilisation of the reconstruction algorithm for samples as large as the method will handle.

The results for the first sample, analysed with the method described in Chapter 6, show that, though inhomogeneities can be localised, their exact amounts could not be determined. Therefore improvements have been suggested and applied to the last two samples.

The results for sample YA02 analysed per layer show that this adjustment leads to more accurate results than analysis per voxel. The comparison of the 0-, 1- and 2-neighbour method show that these methods give comparable results, though the results for the 0-neighbour method appear smoother.

REDNAILS has been verified by INAA of selected voxels of YA02. Comparison of the sample results show good agreement on most points. Deviations may be explained by the fact that small errors in the neutron flux determination outside the sample leads to large errors in the estimated neutron flux inside the sample. Such small errors can easily be made because the neutron flux gradient in the water layer surrounding the sample is very steep, and the positioning of the flux monitors is not all that precise. A way to circumvent this problem may be to use a graphite tube that fills the empty space in the container, instead of water.

The results show that multiple measurements (after different decay times) render better results. This allows for determination of elements that have relatively short lived radionuclides, like Na ($T_{1/2}=15$ h).

Finally, these results show that REDNAILS can be applied for analysis of geological material, especially where long vertical cylinders are sampled. The results for these two samples show vertical gradients, with a higher concentration [mg/ml] of all elements in the lower part of the samples.

9.5 References

1. R.M.W. Overwater, J.E. Hoogenboom, Accounting for the thermal neutron flux depression in voluminous samples for instrumental neutron activation analysis, Nucl. Sci. Eng. 116-7 (1994) 141-157.

Chapter 10

General Discussion

10.1 Introduction

This thesis work has been started in order to develop methods to detect and correct for inhomogeneities in LS-INAA. As mentioned in Chapter 1, referring to the work of Overwater [1,2,3], large errors may occur in reported element concentrations if their spatial distribution is inhomogeneous. Therefore, these inhomogeneities were to be detected and secondly the element distribution was to be determined correctly. To what extent these aims have been achieved is discussed in this chapter.

This discussion is structured as follows. First the general results achieved with the methods are discussed related to the aims of this thesis. This will lead to a discussion of the aims themselves. Next the open issues on details of the method are discussed and questions for further research are formulated.

10.2 Detection of inhomogeneities

The method for detection of inhomogeneities is described in Chapter 6. The results on the validation experiments demonstrate that this method is able to detect inhomogeneities, whether they are 'hot spots', 'hot spots' in a background of radioactivity or more smoothly varying concentrations.

Since this detection method is a straightforward statistical analysis, it has also easily derivable detection limits: the inhomogeneities are detected if they deviate from the normal distribution of the counting statistics, demonstrated by extremely deviating z-scores in the z-score plot, e.g. $|z_{ik}| > 4$.

10.3 Reconstruction of element distributions

The newly developed parts of the reconstruction method described in Chapter 4 (spatial energy-dependent gamma-ray detection efficiency), Chapter 7 (determination of the spatial energy-dependent gamma-ray attenuation) and Chapter 8 (reconstruction algorithms) were found to function properly in partial validation experiments.

As shown in Chapters 8 and 9, a method for reconstruction of the spatial element distributions has been developed, using an holistic approach and a Maximum likelihood reconstruction method with expectation maximisation (MLEM). Validation experiments showed that this method works in principle for smoothly varying fluctuations in the element concentration. Even better accuracy can be expected once the water layer in the irradiation container is replaced by a graphite shell to reduce the flux gradient at the flux-monitor positions.

Errors in the order of a factor of two were still found in the detected element amounts for sharply varying fluctuations in the element concentration in neutron-activated samples and especially for 'hot spots'. These errors are explained by uncertainties about the spatial distribution of the neutron flux in the sample for these cases and especially by the for 'hot spots' invalid 'homogeneous voxel approximation'. Nevertheless, an order of magnitude of the inhomogeneity is indicated.

In general, the accuracy and moreover the quality of the results have been increased with the replacement of LS-INAA with REDNAILS in three aspects. (i) Although REDNAILS still contains errors in the element concentrations, for inhomogeneous samples it renders more accurate average element concentrations than LS-INAA. (ii) The fact that inhomogeneities and spatial distributions of the elements are reported with REDNAILS is an improvement of accuracy in itself. (iii) Warnings that the method is at its limits can be derived from the REDNAILS results itself once sharply varying fluctuations of element concentrations are reported.

10.4 Definition of the design problem

The previous two sections describe to what extent the aims of the thesis have been fulfilled. Both sections still use rather general terms. This is related to

the problem of the formulation of the aims of the project. It is clear that the project has been started to solve the problem of the neutron activation analysis of inhomogeneous large samples. However, the project was without sufficient specifications of the underlying purposes. As soon as more was known about the sample, as shown in Chapter 9, this extra knowledge was incorporated in the optimisation of the method for that typical sample.

This lack of purpose in general therefore also limited the possibilities of optimisation of the set-up as described in Chapter 5. Still some assumptions on the sample structure and the analysis requirements had to be made and were accordingly made.

For example, variations of element concentrations only on a cm scale normally will not affect the accuracy of LS-INAA, and therefore they are not the topic of this research. The spatial resolution of the analysis should be adjusted to the size and distribution of the inhomogeneities of interest, for instance by a larger collimator opening or regularisation in the reconstruction matrix, if this stabilises the reconstruction algorithm.

Hence, further optimisation of the method should only be pursued if a clear definition is formulated for detection limits of the inhomogeneities (size and distribution). A subdivision of sample types with matching analysis strategies is mandatory, based on foreknowledge of the sample a quick screening with the detection method of Chapter 6 and aim of the analysis.

10.5 Open issues

10.5.1 Neutron Activation

The assumption of homogeneity of the samples for neutron-transport calculations [1] is questionable in some special cases. Overwater discussed in his thesis the effects of inhomogeneities on errors in neutron-flux calculations only partially and semi-quantitatively [2,3]. He did not discuss or demonstrate that his methods for neutron-transport calculations could be extended to these inhomogeneous cases. The theory for the neutron-flux distribution has been developed and verified for rotationally homogeneous samples (with respect to neutron diffusion) only. Substantial inhomogeneities of elements with large cross

sections for neutron interaction may disturb the model and create an underestimation or overestimation of the neutron flux at some points in the sample.

Further study of the neutron flux distribution in inhomogeneous samples is mandatory. Experiments with inhomogeneous samples with incorporated and external neutron flux monitors have to be designed to get a more realistic view on the impact of inhomogeneities on the neutron flux.

10.5.2 *'Hot spots' and sharp edges*

In the theory developed it is assumed that the sample may be considered as consisting of a wedge-of-cake shaped volume elements (voxels) that are individually homogeneous. Experiments with samples containing 'hot spots', in Chapter 6, 8 and 9, have shown that detection of these 'hot spots' is not a problem, but errors occur in the results for estimating the element amounts in the voxels that contain these 'hot spots'. The positioning of the source and the small source size may cause an underestimation of K_{ij} . This reflects an underestimation of both local neutron flux and local detection efficiency, and would result in an overestimated amount.

This demonstrates that once these 'hot spots' are detected and acknowledged as being a possible 'hot spot', the voxels around these 'hot spots' must be measured and analysed in a special way. This requires better collimation to zoom in on the 'hot spot' both in vertical and horizontal direction.

The same strategy applies to sharp edges in, apart from that place, smoothly varying element concentrations.

10.5.3 *Collimator leakage*

In Chapter 3, the detection-efficiency calculation and its limitations and uncertainties have already been discussed. These calculations become more critical if an inhomogeneity exists emitting high-energy gamma rays (e.g. above 1 MeV). The amount of the element is overestimated in the current voxel if the leakage of these gamma rays through the collimator is underestimated for measurements in which the inhomogeneity is not in front of the collimator opening.

10.5.4 *Alternative collimation*

As described in Chapter 3 and 5, the set-up is optimised with use of a single-slit collimator. It is optimal for spatial resolution but not for detection efficiency which is a problem since the activity of the sample is relatively low. As mentioned in Chapter 5, worthwhile alternative may be Coded Aperture Imaging (CAI) [4]. CAI is a method used in e.g. astrophysics for celestial imaging of gamma-ray sources where two problems -also met in this research- have to be dealt with: (i) high-energy gamma-ray sources are difficult to focus on and (ii) fluxes are very low. Hence normal collimation would require too long counting times.

Methods and instruments based on so called multiplexing techniques have been developed, consisting of three components: (i) the modulation of the incident gamma rays by a matrix comprising a suitable combination of absorbing and transparent elements (the coded aperture), (ii) position-dependent detection behind the collimator and (iii) reconstruction algorithms comprising the more complex spatial detection efficiency for such a more complex collimator.

The coded aperture can be a one or two dimensional array of elements in front of a position sensitive detector or if the detector is not position sensitive, a series of measurements can be made using different collimator settings (time multiplexing).

10.5.5 *Alternative detectors*

The set-up has been optimised given the current large HPGe detector with high detection efficiency, high energy resolution and high peak-to-Compton ratio, but low spatial resolution (if any). This is optimal of course as long as inhomogeneous samples and detection of inhomogeneity is considered as an extreme case of LS-INAA.

But if inhomogeneous large samples and reconstruction of element distributions in neutron-activated inhomogeneous large samples is to become a more advanced discipline, then another set-up with other detectors may be considered. Below a few options are discussed, ordered with increasing spatial resolution and decreasing energy resolution.

The first option would be a set of collimated HPGe detectors, that would still allow for a high energy-resolution, but a little smaller detection efficiency and peak-to-Compton ratio. These detectors may be smaller (and cheaper) than the

one used now. The gain of this set up is (i) the sum of their detection efficiencies being larger than the detection efficiency of the current detector and (ii) a small gain in spatial resolution caused by using smaller detectors.

Secondly a grid of small germanium detectors may be considered. This grid still has a high energy-resolution, as is typical for germanium detectors, but the peak-to-Compton ratio and the detection efficiency will be dramatically reduced. The advantage is the position sensitivity of such a grid, which allows for a combination with a coded aperture as described in the previous section.

Finally, position-sensitive detectors of more efficient but less energy resolving materials have to be mentioned here. The likeliest candidate materials would be Bismuth Germanate (BGO) and NaI. They can be combined with a coded aperture as well, but application for NAA is only allowed if the gamma spectrum of the activated sample consists of only a few clearly separated peaks [5].

10.5.6 *Influence of peak fitting*

The reconstruction results are highly sensitive to the way the peak positions and areas are determined. As mentioned in Section 8.2.1, the set of fitted peaks and the set of predicted peaks must have the same dimensions or the same list of peaks. An instability occurs if in some spectra: (i) a peak is not fitted on exactly the same position and may therefore be assigned to different elements or (ii) a small peak is found close to another, larger, peak.

Until now, the first problem is acknowledged and accounted for by fixation of peak positions over all spectra, based on the peak position in the sum spectrum. Therefore, the sum spectrum is fitted first. But this solution for the first problem may enlarge the second problem if the fixed position is not correct for all spectra, due to counting statistics, and hence another peak is fitted on the shifted peak. This is not very likely to happen, though, given the stable temperature in the counting room and the regular tests of the stability of the detector and associated electronics.

10.5.7 *Composition of (radio)nuclides or elements list*

Before the reconstruction is started, time can be saved and precision can be gained if a list is used that contains the relevant elements for which a reconstruction has to be performed. It will save time by not necessitating

reconstruction of detection limits and noise, and it may decrease the size of the independent sets of elements if the skipped elements have the same gamma-ray energies as elements that are on the list. The latter will also improve the precision of the reconstruction results because peaks are assigned to fewer elements.

10.5.8 *Improvements of MLEM.*

Notwithstanding the conclusion in Section 8.5.3, still some improvements may be reached in using the MLEM algorithm. Knowing that MLEM gives a better solution but uses more iteration steps, it is worthwhile to apply methods to accelerate the algorithm [6]. The methods may be applied in REDNAILS if it can be changed in such a way that the reconstruction matrix has the shape of a point spread function.

For noisy data sets best results can be found when the algorithm is regularised [6]. Though this will smoothen the result, it prevents noise amplification as reported for the noisy test cases in this chapter. Hence the regularised solution is more realistic.

Another improvement of the MLEM iteration is found by Byrne [7] for sets of solutions that can be limited between a certain bandwidth before the iteration. REDNAILS would also allow for such a bandwidth, defined between zero and the maximum amount that the iteration now uses as starting point (*i.e.* the amount obtained if all counts of a main peak are assigned to the voxel in front of the collimator).

10.5.9 *Reconstruction methods and data presentation*

If spatially more complex measurement set-ups are used, like the detector arrays and coded aperture collimation described in the previous section, then the reconstruction of the spatial element distribution becomes more detailed and more complex as well.

One way to estimate the spatial distribution of the elements to some more detail after the reconstruction is interpolation or 'kriging'.

The reconstruction results can be interpolated to get a more detailed element distribution profile. This can be done in two dimensions: in vertical and in rotational direction. For a profile in radial direction, more measurements should be applied, where distance to the centre is varied.

For interpolation the reconstruction results itself must be stable enough. If the concentration does not vary significantly between two points, the concentration may be assumed to be constant. Considering the results in Chapter 9, this means that for some elements (e.g. the matrix elements in Sample 1 in Chapter 9) it is not possible to interpolate in rotational direction. More stable results are reached then with considering the layer homogeneous (before reconstruction) or averaging (afterwards).

10.5.10 *Further interpretation of transmission measurements*

As concluded in Chapter 7, the method for determination of the linear attenuation of gamma rays results, renders attenuation coefficients that agree well with known values. Figure 4 in Chapter 7 shows even that from the transmission measurements we are able to derive the specific mass of the voxel.

This value can either be used for further interpretation of the calculated element amounts per voxel towards element concentrations (in mg/kg), if the value for the density shows not too large variations between the voxels or as a caveat for large variations in density of the voxel. The latter may indicate large sample matrix inhomogeneities.

10.6 References

1. R.M.W. Overwater, J.E. Hoogenboom, Accounting for the thermal neutron flux depression in voluminous samples for instrumental neutron activation analysis, *Nucl. Sci. Eng.* 116-7 (1994) 141-157.
2. R.M.W. Overwater, P. Bode, Computer simulations of the effects of inhomogeneities on the accuracy of large sample INAA, *Appl. Radiat. Isot.* 49 (1998) 967-976.
3. R.M.W. Overwater, The physics of Big Sample Instrumental Neutron Activation Analysis, thesis, Delft 1994
4. E. Caroli, J.B. Stephen, G. Di Cocco, L. Natalucci, A. Spizzicino, Coded Aperture Imaging in X- and Gamma-ray Astronomy, *Space Sci. Rev.* 45 (1987) 349-403.
5. N.M. Spyrou, J.M. Sharaf, S. Sarkar, Elemental analysis of biological matrices using tomographic techniques, *J. Rad. Nucl. Chem.* 167 (1993) 453-465.

6. G.M.P. van Kempen, L.J. van Vliet, P.J. Verveer, Application of image restoration methods for confocal fluorescence microscopy, Proc. SPIE 2984 (1997) 114-124.
7. C. Byrne, Iterative algorithms for deblurring and deconvolution with constraints, Inverse problems, 14 (1998) 1455-1467.

Summary

REDNAILS

Neutron Activation Analysis of Inhomogeneous Large Samples - An Explorative Study

Neutron activation analysis is a powerful technique for the determination of trace-element concentrations. Since both neutrons that are used for activation and gamma rays that are detected have a high penetrating power, the technique can be applied for relatively large samples (up to 13 L), as demonstrated by Overwater. This technique resulted only in average results for the element concentration, which led to the following problems. Firstly, the result for a (simple) single sample doesn't give information about the representativity of the sample related to the population it was sampled from. Secondly, evaluation by Overwater of the impact of element distributions on the correctness of results indicated large errors, up to 100%, without being noticed by the analyst if no extra measures were taken.

A method that provides information as to the spatial element distribution may overcome these problems in a reverse order. Firstly, if the element distribution is known, then the total amount of the element in the sample can be determined more accurately. Secondly, the element distribution gives information about the inhomogeneity of the sample; if the sample is a composition of subsamples the results also provide information about the representativity of the sample and the inhomogeneity of the population. A third advantage is that such a method would provide information about the structure of the sample. This may be of interest for e.g. geological samples.

Therefore the study underlying this thesis was started. It explores methods for determination of element distributions in large samples using the principles of Neutron Activation Analysis (NAA).

Chapter 1 provides a view on the development of NAA from the beginning until the recent steps that are described in this thesis. In Chapter 2, the problems of representative sampling in the analysis of inhomogeneous bulk materials are briefly discussed. As mentioned above, this is one of the major problems that asked for a solution as explored by this thesis work.

Methods and results are presented in Chapter 3 through 9. Chapter 3 gives the framework of and constraints for this study (the design of a method for neutron activation analysis of inhomogeneous large samples) and describes the steps in the design of the method that are not part of this study. It points to Chapters 4 through 9 for those parts that constitute the thesis work. The method is an extension of the so-called “holistic approach”: for each element in each voxel a response matrix is calculated for each measurement. From this set a weighted subset is chosen by fitting towards the most likely solution using expectation maximisation (MLEM) or using the conjugate gradient method with a nonnegative constraint (CGNN), see Chapter 8.

As discussed by Overwater, the largest errors in LS-INAA can be expected for inhomogeneity of trace elements due to a wrong correction of the gamma-ray detection efficiency. Therefore it was decided to use his methods for calculation of the neutron flux distribution in the sample without any caveat or correction for local fluctuations in the parameters for neutron interactions due to inhomogeneities.

The method for calculation of the detection efficiency for gamma rays is described in Chapter 4. Firstly, a series of Monte Carlo simulations has been performed to determine the detector efficiency as a function of gamma-ray energy and the dimensions of the path of the gamma ray through the detector. These results have been used for a method that enables to determine the gamma-ray efficiency for any point in the sample. Correction for attenuation in the sample and collimator are included. Methods for calculation of the local attenuation coefficients in the sample are presented in Chapter 7.

For the measurements, the set-up as developed by Overwater was used as a starting point. In Chapter 5, the optimisation of the set-up for the new measurements is discussed. Assuming a method of collimated scanning in vertical and rotational direction, the sample is considered to consist of wedge-of-cake shaped volume elements (voxels), and optimal collimator opening and voxel size

are discussed. It is mentioned that also the constraints for a particular sample have to be taken into consideration

In Chapter 6, a quick scanning method is presented, that provides statistical information about the sample in order to decide whether the sample is homogeneous enough to analyse it via the method of Overwater. Otherwise, it should be analysed using REDNAILS.

Chapter 8 discusses the above-mentioned reconstruction algorithms. They are tested against a few mathematical samples. In Chapter 9, REDNAILS is tested with practical samples after some adjustments based on knowledge of the general sample contents. It is shown that the method gives in most cases sufficiently accurate results, but in some cases local fluctuations in the parameters for neutron interactions due to inhomogeneities cannot be neglected.

The thesis work and the resulting methods as a whole are discussed in Chapter 10. A list of parts that need further investigation is provided. Further development of the method requires in particular an answer to the question what REDNAILS is practically to be applied for, since that will set proper criteria for an optimal design.

Samenvatting

REDNAILS

Neutronen activeringsanalyse van inhomogene grote monsters – een verkennende studie

(Neutron Activation Analysis of Inhomogeneous Large Samples - An Explorative Study)

Neutronen activeringsanalyse is een succesvolle analysemethode voor de bepaling van de concentratie van sporenelementen in monsters. Omdat zowel neutronen als gamma's een hoog doordringend vermogen hebben, is deze methode bij uitstek ook geschikt voor de analyse van grote monsters (tot 13 liter) zoals aangetoond door Overwater. Zijn methode leverde alleen gemiddelde waarden voor de element concentraties. Dit leidde tot de volgende problemen. Ten eerste geeft het resultaat van één monster geen informatie over de representativiteit van het monster voor het grotere geheel waaruit het getrokken was. Ten tweede, evaluatie door Overwater van de juistheid van resultaten toonde grote fouten, tot 100%, ten gevolge van, kan een inhomogene ruimtelijke verdeling van elementen in het grote monster, zonder dat de onderzoeker dit zou merken als geen aanvullende maatregelen zouden worden getroffen.

Een methode die informatie geeft over de ruimtelijke verdeling van de elementen zou bovenstaande problemen aanpakken, te beginnen bij het laatste. Ten eerste, als de ruimtelijke element verdeling bekend is, dan kan de totale hoeveelheid van het element in het monster nauwkeuriger bepaald worden. Ten tweede geeft de element verdeling informatie over de inhomogeniteit van het monster. Als het grote monster een compositie is van random verzamelde kleinere monsters, dan zal het resultaat ook informatie geven over de representativiteit van het grote monster en de inhomogeniteit van de totale partij. Een derde voordeel is

dat een dergelijke methode informatie kan geven over de structuur van het monster, wat interessant kan zijn voor bijvoorbeeld geologische monsters.

Gezien bovenstaande overwegingen is het onderzoek gestart dat ten grondslag ligt aan dit proefschrift. Het verkent de methodes benodigd voor de bepaling van element verdelingen in grote monsters gebaseerd op de principes van neutronen activeringsanalyse (NAA).

Hoofdstuk 1 voorziet in een overzicht op de ontwikkeling van NAA, van het begin tot de recente stappen die worden beschreven in dit proefschrift. In hoofdstuk 2 worden de problemen van representatief bemonsteren voor de analyse van inhomogene partijen kort bediscussieerd. Zoals hierboven genoemd, is dit een van de grote problemen die een oplossing, zoals verkend in dit proefschrift, benodigden.

De methoden en behaalde resultaten worden beschreven in hoofdstuk 3 tot 9. Hoofdstuk 3 geeft het raamwerk van de methode (het ontwerp van een methode voor neutronen activeringsanalyse van inhomogene grote monsters) en de randvoorwaarden. Het beschrijft ook de stappen van het ontwerp van de methode die niet speciaal in deze studie zijn uitgewerkt. Er wordt verwezen naar hoofdstuk 4 tot 9 voor de onderdelen die wel het werk voor het proefschrift betreffen. De methode is een uitbreiding van de zogenaamde “holistische benadering”: voor elk element in elk blokje van het monster (voxel) wordt het verwachte gamma-stralingsspectrum berekend voor elke meting. Van deze verzameling wordt een gewogen deelverzameling gekozen door die het best past bij de echte metingen. Dit kiezen kan via twee strategieën: de meest waarschijnlijke oplossing wordt gezocht door maximalisatie van de verwachtingswaarde (MLEM), of het verschil tussen voorspelde en gemeten metingen wordt geminimaliseerd door gebruik te maken van de geconjugeerde gradiënt methode met als randvoorwaarde dat concentraties niet negatief mogen zijn (CGNN). Dit is beschreven in hoofdstuk 8.

Zoals besproken door Overwater, kunnen de grootste fouten in grote monster NAA verwacht worden met inhomogene sporenelementen ten gevolge van een verkeerde correctie voor de detectie efficiëntie van gammastraling. Daarom is gekozen zijn methode voor de berekening van de neutronen flux te gebruiken, zonder correcties voor fluctuaties in de neutronenparameters ten gevolge van inhomogeniteiten, op kleinere schaal dan nu al gebeurt in zijn methode.

De methode voor berekening van de detectie efficiëntie voor gammastraling is beschreven in hoofdstuk 4. Allereerst is een aantal Monte-Carlo berekeningen uitgevoerd om de detectie efficiëntie te bepalen als een functie van de energie van de gammastraling en de dimensies van de weg van de gammastraal door het detectorkristal. Met deze resultaten is een methode ontwikkeld die de detectie efficiëntie kan bepalen voor elk punt in het monster, inclusief correctie voor verzwakking in het monster en de collimator. De methode voor de bepaling van de lokale verzwakkingscoëfficiënten wordt weergegeven in hoofdstuk 7.

Voor de metingen is uitgegaan van de opstelling van Overwater. In hoofdstuk 5 wordt de optimalisatie van deze opstelling voor de nieuwe metingen besproken. Uitgaande van een methode van gecollimeerd scannen en verticale en rotatoire richting, wordt het monster beschouwd als te zijn opgebouwd uit taartpuntvormige voxels. De optimale collimator opening en voxel grootte wordt bediscussieerd. Daarbij moet genoemd worden dat daarbij ook de randvoorwaarden van een bepaald monster in acht moeten worden genomen.

In hoofdstuk 6 wordt een snelle scan methode gepresenteerd die statistische informatie oplevert over het monster, om te kunnen bepalen of het monster homogeen genoeg is voor analyse volgens de methode van Overwater. Zo niet, dan moet geanalyseerd worden met behulp van reconstructie van de element verdeling van met neutronen geactiveerde inhomogene grote monsters (REDNAILS).

Hoofdstuk 8 bespreekt de hierboven genoemde reconstructie algoritmes, waarbij ze worden getest met behulp van mathematische modellen. In hoofdstuk 9 wordt REDNAILS getest met monsters uit de praktijk, na een aantal aanpassingen gebaseerd op kennis over algemene eigenschappen van monsters. Aangetoond wordt dat de methode in de meeste gevallen accurate resultaten levert, maar dat in enkele gevallen lokale schommelingen in de parameters voor neutronen interacties ten gevolge van inhomogeniteiten niet genegeerd kan worden.

Dankwoord

Eindelijk, eindelijk is het af! Dit is vast een verzuchting die bijna elke promovendus al dan niet hardop zal slaken als het dan zover is. Dat het eindelijk zover kon komen heb ik mede te danken aan veel mensen.

Allereerst Menno. Jij bent vanaf het begin intensief bij het project betrokken geweest. Ik heb altijd gebruik kunnen maken van je kennis van vrijwel alle aspecten van de neutronenactiveringsanalyse en van je adviezen bij allerlei technische details. Jij hebt in een laat stadium nog een extra experiment uitgevoerd om de methode in de praktijk te testen.

Peter, als werkgroepleider was jij ook onmisbaar. Je had een iets grotere afstand tot het project en daardoor had jij juist oog voor de grotere lijnen en toekomstige toepassingen.

Jeroen, je kritische opstelling en menige vraag naar het wat, hoe en waarom hebben ertoe geleid dat dit proefschrift flink in helderheid en kwaliteit is gestegen. Ondanks de druk van de vele promovendi wilde je toch steeds de tijd nemen om de tekst grondig door te spitten.

Ad, jou ben ik erkentelijk dat jij als medepromotor bij mijn proefschrift wilde optreden.

Beste Heleen, Sjoerd, Bas en Frank. Als kamergenoten wil ik jullie graag bedanken. Het was een goede tijd, waarin we eerste ontdekkingen of bugs in de software, proefballonnetjes en persoonlijk wel en wee goed konden delen. Ook de andere promovendi in de afdeling Radiochemie wil ik bedanken voor de goede samenwerking en contacten. Het was door de jaren heen een hechte club.

Ook de ondersteuning vanuit de werkgroep wil ik niet onvermeld laten. De basiskennis van instrumentele neutronenactiveringsanalyse en de praktische vaardigheden zeker voor bestraling en meting van grote monsters heb ik in eerste instantie geleerd van Rob. En ook Anneke, Thea, Mehmet en Karin hebben me de kneepjes van deze techniek bijgebracht. Voor technische ondersteuning of een

kopje thee kon ik altijd bij Theo terecht en Folkert was en is een ideale vraagbaak voor software en hardwareproblemen.

Lieve Anneclair, dank je voor je steun, zeker in de laatste jaren toen we ook wel eens verzuchten of het nog wel ooit af zou komen. Dorine en Nora, het is eindelijk zover: nog één dagje examen doen en daarna is het feest! Jullie hebben ook meegeholpen om ook dit boekje in het juiste perspectief te blijven zien.

Curriculum vitae

Hendrik Willem (Erwin) Baas was born on 9 April 1972 in Staphorst, The Netherlands. He obtained his VWO diploma at the “Gereformeerde Scholengemeenschap” at Amersfoort in 1990 and started directly afterwards his studies in physics at the “Rijksuniversiteit” at Leiden. He obtained his masters degree in 1996 for his work on “Monte Carlo simulations of radiotherapy treatments to relate dose distributions to secondary tumours after irradiation for Hodgkin’s disease”, under supervision of Prof. Dr. J.J. Broerse and Dr. Ir. J. Dave-laar at the Oncology Department of the Leiden University Medical Centre.

From 1996 until 2000, Erwin worked as a PhD student in the Physical and Mathematical Radioanalysis group of the Department Radiochemistry of the Interfaculty Reactor Institute. This work that is described in this thesis, was conducted under supervision of Dr. M. Blaauw and Prof. Dr. Ir. J.J.M. de Goeij.

In 2000, Erwin accepted a position as trainee in clinical physics - audiology at the “Samenwerkende Audiologische Centra” at Eindhoven. The first two years he was in a postgraduate designer program of the Eindhoven University of Technology under supervision of Prof. Dr. H.C.W. Beijerinck. He was awarded in 2003 with the title “Master of Technological Design” (MTD). He is working as clinical physicist - audiologist at “Instituut Sint Marie” at Eindhoven and the University Medical Centre Utrecht.

He is married to Anneclair Griffioen. They have two children, Dorine (2001) and Nora (2003).

List of Publications

Papers

1. H.W. Baas, M. Blaauw, Determining the depth distribution of planar gamma-ray sources using the shape of the Compton continuum: Experimental test, Nucl. Instr. Meth. Phys. Res. A 413 (1998) 440-446
2. H.W. Baas, M. Blaauw, P. Bode, et al. Collimated scanning towards 3D-INAA of inhomogeneous large samples, Fresen. J. Anal. Chem 363 (1999): 753-759
3. H.W. Baas, P. Bode, M. Blaauw, Ge detector efficiency calculations for determination of three-dimensional radioactivity distributions, Rad. Phys. Chem. 61 (2001) 637-638
4. M. Blaauw, H.W. Baas, M. Donze, Height-resolved large-sample INAA of a 1 m long, 13 cm diameter ditch-bottom sample, Nucl. Instr. Meth. Phys. Res. A 505 (2003) 512-516

Oral and poster presentations

1. H.W. Baas, M. Blaauw, Neutron Activation Analysis of Inhomogeneous Large Samples, Intelligent Analytical Solutions 1, Jülich, 1998
2. Erwin Baas, Menno Blaauw, Peter Bode, Jeroen De Goeij, 3D-Neutron Activation Analysis - Going to the extremes, Modern Trends in Activation Analysis 10, Washington, 1999
3. J.J.M. de Goeij, H.W. Baas, M. Blaauw, Non-Destructive Analysis of very Large Objects: Three-Dimensional Spectrometry for Inhomogeneity Studies, 6th International Conference on Applications of Nuclear Techniques, Crete, 1999
4. P. Bode, H.W. Baas, M. Blaauw, Finding Elements By Spatially Resolved INAA, 4th International Conference on the Analysis of Geological and Environmental Materials, Pont à Mousson, 2000
5. E. Baas, P. Bode, M. Blaauw, 3D Gamma-ray Ge detector efficiency modelling, International Symposium on Radiation Physics 8, Prague 2000